

# 1        The novel anti-CRISPR AcrIIA22 relieves DNA torsion in target 2        plasmids and impairs SpyCas9 activity

3        Kevin J. Forsberg<sup>a,b,\*†</sup>, Danica T. Schmidtke<sup>a</sup>, Rachel Werther<sup>a</sup>, Ruben V. Uribe<sup>c</sup>, Deanna  
4        Hausman<sup>a</sup>, Morten O.A. Sommer<sup>c</sup>, Barry L. Stoddard<sup>a</sup>, Brett K. Kaiser<sup>a,d</sup>, Harmit S. Malik<sup>a,b</sup>

<sup>a</sup>Division of Basic Sciences & <sup>b</sup>Howard Hughes Medical Institute, Fred Hutchinson Cancer Research Center, Seattle, WA, 98109 USA; <sup>c</sup>Novo Nordisk Foundation Center for Biosustainability, Technical University of Denmark, Lyngby 2800, Denmark; <sup>d</sup>Department of Biology, Seattle University, 901 12th Avenue, Seattle, WA 98122, USA

5        <sup>†</sup>Current address: Department of Microbiology, University of Texas Southwestern Medical Center,  
6        Dallas TX 75390, USA; email: [kevin.forsberg@utsouthwestern.edu](mailto:kevin.forsberg@utsouthwestern.edu)

7        Running title: AcrIIA22 alters DNA torsion and protects plasmids from Cas9

8        \*Address correspondence to: Kevin J. Forsberg, Department of Microbiology, University of Texas  
9        Southwestern Medical Center, 5323 Harry Hines Blvd, Dallas TX 75390, USA; email:  
10        [kevin.forsberg@utsouthwestern.edu](mailto:kevin.forsberg@utsouthwestern.edu)

11 **Abstract**

12 **To overcome CRISPR-Cas defense systems, many phages and mobile genetic elements**  
13 **encode CRISPR-Cas inhibitors called anti-CRISPRs (Acrs). Nearly all characterized Acrs**  
14 **directly bind Cas proteins to inactivate CRISPR immunity. Here, using functional**  
15 **metagenomic selection, we describe AcrIIA22, an unconventional Acr found in**  
16 **hypervariable genomic regions of clostridial bacteria and their prophages from human gut**  
17 **microbiomes. AcrIIA22 does not bind strongly to SpyCas9 but nonetheless potently**  
18 **inhibits its activity against plasmids. To gain insight into its mechanism, we obtained an**  
19 **X-ray crystal structure of AcrIIA22, which revealed homology to PC4-like nucleic-acid**  
20 **binding proteins. Based on mutational analyses and functional assays, we deduced that**  
21 **acrIIA22 encodes a DNA nickase that relieves torsional stress in supercoiled plasmids.**  
22 **This may render them less susceptible to SpyCas9, which uses free energy from negative**  
23 **supercoils to form stable R-loops. Modifying DNA topology may provide an additional**  
24 **route to CRISPR-Cas resistance in phages and mobile genetic elements. (150)**

25 **Introduction**

26 CRISPR-Cas systems in bacteria and archaea confer sequence-specific immunity against  
27 invading phages and other mobile genetic elements (MGEs)<sup>1,2</sup>. In response, MGEs can  
28 circumvent CRISPR-Cas systems by evading CRISPR immunity. In its simplest form, evasion  
29 requires only a single mutation within a CRISPR target site, which allows a phage or MGE to  
30 escape immune recognition<sup>3</sup>. However, CRISPR-Cas systems routinely acquire new spacer  
31 sequences corresponding to new sites within phage and MGE genomes<sup>1</sup>. This means that any  
32 single-site evasion strategy is likely to be short-lived. Thus, phages also employ forms of CRISPR-  
33 Cas evasion that are less easily subverted. For instance, some jumbophages assemble a  
34 proteinaceous, nucleus-like compartment around their genomes upon infection, allowing them to  
35 overcome diverse bacterial defenses, including CRISPR-Cas and restriction-modification (RM)  
36 systems<sup>4,5</sup>. Similarly, other phages decorate their DNA genomes with diverse chemical  
37 modifications such as the glucosylated cytosines used by phage T4 of *Escherichia coli*<sup>6</sup>, which  
38 can prevent Cas nucleases from binding their target sequence.

39 MGEs may also overcome CRISPR-Cas systems by inactivating, rather than evading,  
40 CRISPR immunity. MGEs encode diverse CRISPR-Cas inhibitors called anti-CRISPRs (Acrs),  
41 which allow them to overcome CRISPR-Cas systems and infect otherwise immune hosts<sup>7</sup>. Most  
42 known Acrs bind Cas proteins and inhibit Cas activity by restricting access to target DNA,  
43 preventing necessary conformational changes, or inactivating critical CRISPR-Cas  
44 components<sup>8,9</sup>. The direct inactivation of Cas proteins by Acrs has proven an effective and  
45 widespread strategy for overcoming CRISPR immunity<sup>10</sup>.

46 Recent genetic, bioinformatic, and metagenomic strategies have identified many Acrs that  
47 independently target the same CRISPR-Cas system<sup>7-10</sup>. Yet, most CRISPR-Cas systems are not  
48 inhibited by known Acrs<sup>10</sup>. Thus, many undiscovered strategies to inhibit or evade CRISPR-Cas  
49 systems likely exist in nature. Indeed, over half of the genes in an average phage genome have  
50 no known function<sup>11</sup>. To uncover new counter-immune strategies, we recently devised a high-  
51 throughput functional metagenomic selection to find genes that protect a target plasmid from  
52 *Streptococcus pyogenes* Cas9 (SpyCas9), the variant used most frequently for genome editing<sup>12</sup>.  
53 Our selection strategy was designed to reveal any gene capable of overcoming SpyCas9 activity  
54 in this system, regardless of mechanism. With this approach, we previously described a new

55 phage inhibitor of SpyCas9, called AcrIIA11, which exhibits broad-spectrum anti-Cas9 activity and  
56 is prevalent across human gut microbiomes<sup>12</sup>.

57 Here, we describe *acrIIA22*, which was the second most common Acr candidate recovered  
58 from our original functional selection. *AcrIIA22* encodes a 54 amino acid protein that impairs  
59 SpyCas9 activity. We observe that homologs of *acrIIA22* are found in hypervariable loci in phage  
60 and bacterial genomes. Unlike most other Acrs, AcrIIA22 does not bind strongly to SpyCas9 *in*  
61 *vitro*. Instead, guided by an X-ray crystal structure of AcrIIA22, coupled with mutational and  
62 biochemical analyses, we show that AcrIIA22 encodes a DNA nickase. By nicking a supercoiled  
63 plasmid substrate and relieving its torsional stress, AcrIIA22 renders the target less susceptible  
64 to SpyCas9 activity. AcrIIA22 thus represents a novel mechanism of SpyCas9 evasion, which  
65 capitalizes on SpyCas9's preference for negative supercoils to efficiently form R-loops and cleave  
66 DNA<sup>13-16</sup>. Such a resistance mechanism could be accessible to diverse MGEs, providing a route  
67 to CRISPR-Cas tolerance in many genetic contexts.

68 **Results**

69 **Functional selection reveals a novel anti-CRISPR protein, AcrIIA22**

70 We recently carried out a functional selection for SpyCas9 antagonism, recovering clones  
71 from metagenomic libraries that could potently inhibit SpyCas9<sup>12</sup>. In this two-plasmid setup, we  
72 used an arabinose-inducible SpyCas9 on an expression plasmid to cleave the *kanamycin*  
73 *resistance (Kan<sup>R</sup>)* gene of a second 'target' plasmid. We then grew cultures in SpyCas9-inducing  
74 conditions and measured the proportion of colony forming units (cfus) that remained kanamycin  
75 resistant (Figure 1A). This proportion is a measure of how many clones retained their target  
76 plasmid and, thus, how effectively that plasmid withstood SpyCas9 attack. In our previously  
77 published work, we describe AcrIIA11, a novel anti-CRISPR from a metagenomic clone named  
78 F01A\_2 (Genbank ID MK637582.1), which was the most abundant clone after functional selection  
79 of a human fecal microbiome<sup>12</sup>. This functional selection also revealed another protective clone,  
80 F01A\_4 (Genbank ID MK637587.1), which was the second most abundant contig following  
81 selection. Together, these two contigs (F01A\_2 and F01A\_4) accounted for >96% of the  
82 normalized read coverage.

83 The F01A\_4 contig is 685 bp long, encodes three potential open reading frames (ORFs),  
84 and confers complete protection against SpyCas9, with plasmid retention equaling that of an  
85 uninduced SpyCas9 control (Figure 1B). To determine the genetic basis for SpyCas9 antagonism  
86 in this contig, we introduced an early stop codon into each of the three potential ORFs and  
87 analyzed how these mutations affected the contig's ability to protect a target plasmid from  
88 SpyCas9. We found that an early stop codon in *orf\_1* reduced the proportion of *Kan<sup>R</sup>* cfus by a  
89 factor of 10<sup>5</sup>, matching the value observed for an empty vector control (Figure 1B). Furthermore,  
90 expression of *orf\_1* alone was sufficient for SpyCas9 antagonism (Figure 1C), protecting a target  
91 plasmid from SpyCas9 cleavage as effectively as the potent SpyCas9 inhibitor, AcrIIA4. In this  
92 assay, *orf\_1* was slightly toxic when singly expressed in *E. coli*, reducing growth rate by 7%  
93 (Supplemental Figure 1). Combined, our results indicate that *orf\_1* completely accounts for the  
94 SpyCas9 protection phenotype of contig F01A\_4.

95 One mechanism through which *orf\_1* could apparently antagonize SpyCas9 in our functional  
96 assay would be by lowering its expression. To address this possibility, we carried out two  
97 experiments. First, we swapped the *spycas9* gene for *gfp* in our expression vector and asked  
98 whether *orf\_1* induction impacted fluorescence output. We saw no change in fluorescence upon

99 *orf\_1* induction, indicating that *orf\_1* neither suppressed transcription from our expression vector  
100 nor altered its copy number (Supplemental Figure 2). Second, we used Western blots to test  
101 whether *orf\_1* expression impacted SpyCas9 protein levels through the course of a plasmid  
102 protection assay. We used a crRNA that did not target our plasmid backbone to ensure that *orf\_1*  
103 expression remained high to maximize its potential impact on SpyCas9 expression levels. We  
104 observed that *orf\_1* expression had no meaningful effect on SpyCas9 expression at any timepoint  
105 (Supplemental Figure 2). Thus, we conclude that *orf\_1* does not impact SpyCas9's translation or  
106 degradation rate. Therefore, *orf\_1* must act via an alternative mechanism to inhibit SpyCas9  
107 activity. Based on these findings, we conclude that *orf\_1* encodes a *bona fide* anti-CRISPR  
108 protein and hereafter refer to it as *acrIIA22*.

109 Next, we investigated whether *acrIIA22* could also allow phages to escape from SpyCas9  
110 immunity (Supplemental Figure 3). We measured SpyCas9's ability to protect *E. coli* from infection  
111 by phage Mu, in the presence or absence of *acrIIA22*. As a control, we carried out similar phage  
112 infections in the presence or absence of the well-established SpyCas9 inhibitor, *acrIIA4*. As  
113 anticipated, SpyCas9 significantly impaired Mu when targeted to the phage's genome but not if a  
114 non-targeting CRISPR RNA (crRNA) was used. Consistent with previous findings<sup>12</sup>, phage Mu  
115 could infect targeting strains equally well as non-targeting strains when *acrIIA4* was expressed,  
116 indicating that SpyCas9 immunity was completely abolished by this *acr*. In comparison, *acrIIA22*  
117 improved the infectivity of phage Mu by a factor of 100 to 1,000 across multiple experimental  
118 conditions (Supplemental Figure 3). We therefore conclude that *acrIIA22* only partially protects  
119 phage Mu from SpyCas9 whereas it completely protects plasmids against SpyCas9 cleavage.

## 120 ***AcrIIA22 homologs are found in hypervariable regions of bacterial and prophage genomes***

121 *AcrIIA22* is 54 amino acids in length and has no sequence homology to any protein of known  
122 function, including all previously described *Acrs*. We examined the distribution of *acrIIA22*  
123 homologs in NCBI's NR and WGS databases but found just seven hits, limiting our ability to make  
124 evolutionary inferences about its origins or prevalence. We therefore expanded our search to  
125 include IMG/VR, a curated database of cultured and uncultured DNA viruses<sup>17</sup>, and assembly  
126 data from a meta-analysis of 9,428 diverse human microbiome samples<sup>18</sup>. With an additional 23  
127 unique homologs from these databases, we found that the majority of *acrIIA22* homologs exist in  
128 either of two genomic contexts: prophage genomes (Figure 2A, Supplemental Figure 4A) or small,  
129 hypervariable regions of bacterial genomes, which we refer to hereafter as 'genomic islands'  
130 (Figure 2B, Supplemental Figure 4B). The original metagenomic DNA fragment from our  
131 selection, F01A\_4, shared perfect nucleotide identity with one of these genomic islands (Figure  
132 2B).

133 Because most *acrs* are found in phage genomes, we first examined the prophages that  
134 encoded *AcrIIA22* homologs. These prophages were clearly related, based on many homologous  
135 genes and a similar genome organization (Supplemental Figure 4A). We found that these  
136 prophages had inserted into several different bacterial loci, including one site between the  
137 bacterial genes *purF* and *radC* (locus #3, Supplemental Figure 4A). This insertion site is nearly  
138 identical to the highly conserved sequences that flanked *acrIIA22*-encoding bacterial genomic  
139 islands (Supplemental Figure 4B). Based on this common insertion site, we hypothesize that the  
140 apparently bacterial genomic islands with *acrIIA22* homologs originated from a common prophage  
141 insertion at this locus. We speculate that the original *acrIIA22*-encoding bacterial genomic island  
142 resulted from the incomplete excision of an ancestral, *acrIIA22*-encoding prophage. Supporting

143 this hypothesis, *acrIIA22* homologs are always found at the end of prophage genomes, near their  
144 junction with a host bacterial genome (Figure 2A, Supplemental Figure 4A).

145 To better understand *acrIIA22*'s gene neighborhood, we again searched the assemblies of  
146 over 9,400 human microbiomes for more examples of these genomic islands<sup>18</sup>. We did not include  
147 *acrIIA22* as a query. Instead, we only considered contigs with ≥98% nucleotide identity to *purF*  
148 and *radC*, the conserved genes that flanked the genomic islands. This search yielded 258 contigs.  
149 Aligning these sequences revealed that each contig encoded a short, hypervariable region of  
150 small ORFs which was flanked by conserved genomic sequences (Figure 2B, Supplemental  
151 Figure 4B). In total, we observed 128 unique examples of these hypervariable loci, which  
152 displayed considerable gene turnover, resulting in 54 distinct gene arrangements among the 128  
153 unique loci. Despite not being included in our search criteria, *acrIIA22* homologs were universally  
154 conserved in all 128 unique genomic islands. In contrast, no other gene was present in more than  
155 two-thirds of the 54 distinct gene arrangements (Figure 2B, Supplemental Figure 4C). Based on  
156 this finding, we infer that the arrival of *acrIIA22* preceded the diversification seen at this locus and  
157 has been retained despite the considerable gene turnover that has occurred subsequently.

158 Though most ORFs in these islands were of unknown function, many had close homologs in  
159 the genomes of nine representative *acrIIA22*-encoding phage (Supplemental Figures 4A, 4B, 4C).  
160 This suggests that phages continue to supply the genetic diversity seen at these hypervariable  
161 genomic loci. These rapid gene gains and losses likely occur as they do in other genomic islands,  
162 via recombination between this locus and related MGEs that infect the same host bacterium,  
163 without the MGE necessarily integrating into the locus<sup>19</sup>. Taken together, our data suggest that  
164 an incomplete prophage excision event left *acrIIA22* behind in a bacterial genomic locus, which  
165 then diversified via gene exchange with additional phage genomes (Figure 2C, Supplemental  
166 Figure 4D).

167 Like in the genomic islands (Figure 2B), we found *acrIIA22* homologs in hypervariable regions  
168 of prophage genomes, where they were consistently near the junction with a host bacterial  
169 genome (Supplemental Figure 4A). Thus, nearly all *acrIIA22*-encoding loci show signatures of  
170 frequent recombination. Despite this, we could find no gene consistently present within or outside  
171 of *acrIIA22*-encoding genomic islands that could account for their hypervariable nature (e.g. an  
172 integrase, transposase, recombinase, or similar function that is typically associated with locus-  
173 specific recombination<sup>20</sup>). Instead, *acrIIA22* was the only gene conserved at this locus. This  
174 conservation led us to speculate that *acrIIA22* might promote recombination, either alone or with  
175 other factors. If this were true, it could explain the high rates of gene exchange observed adjacent  
176 to the *acrIIA22* gene in phage and bacterial genomes (Figure 2, Supplemental Figure 4).

177 In total, we identified 30 unique *acrIIA22* homologs, 25 of which were predicted to originate  
178 from the unnamed clostridial genus, CAG-217 (Figure 3A). Because *acr*s are only beneficial to  
179 phages if they inhibit CRISPR-Cas activity, they are typically found only in taxa with a high  
180 prevalence of susceptible Cas proteins<sup>9</sup>. If AcrIIA22 functions naturally as an Acr, we would  
181 predict that Cas9-encoding, type II-A CRISPR-Cas systems like SpyCas9 would be common in  
182 CAG-217 bacteria. To test this idea, we examined 779 draft assemblies of CAG-217 genomes  
183 and found that 179 of the 181 predicted CRISPR-Cas systems were type II-A systems (the  
184 remaining two loci were Cas12-encoding, type V-A systems). This enrichment for Cas9 is  
185 particularly striking as *Clostridia* typically encode other CRISPR-Cas defenses and only rarely  
186 encode Cas9-based systems<sup>21</sup>. Moreover, prophages from CAG-217 encode 78 type II-A Acrs  
187 (homologs of AcrIIA7, AcrIIA17, and AcrIIA21), suggesting they are actively engaged in an arms

188 race with Cas9-based defenses in these bacteria. In one case, we found *acrIIA17* and *acrIIA22*  
189 homologs within one kilobase of each other in a prophage genome (Supplemental Figure 5)<sup>22</sup>.  
190 Phages often collect *acr* genes in the same genomic locus<sup>23</sup>, commonly pairing narrow-spectrum  
191 *acs* that act during lytic infection alongside broad-spectrum *acs* that operate during lysogeny<sup>24</sup>.  
192 Together, these observations support our hypothesis that prophages encode *acrIIA22* homologs  
193 to inhibit type II-A CRISPR-Cas (Cas9) systems in CAG-217 genomes.

194 We next tested whether the ability to inhibit type II-A CRISPR-Cas systems was shared among  
195 *acrIIA22* homologs from CAG-217 bacteria. To do so, we selected *acrIIA22* homologs that  
196 spanned the phylogenetic diversity present among CAG-217 genomes (Figure 3A) and tested  
197 their ability to protect a target plasmid from SpyCas9 elimination. These analyses revealed that  
198 diverse *acrIIA22* homologs from CAG-217 bacteria (for example, sharing only 56.9% identity)  
199 could antagonize SpyCas9 activity at least partially (Figure 3B), reminiscent of the broad inhibition  
200 that has been previously observed for some other type II-A *Acrs*<sup>12</sup>. To determine if this anti-  
201 CRISPR activity extended beyond SpyCas9, we used a slightly modified plasmid protection assay  
202 (see methods) to test whether *acrIIA22* could inhibit other type II and type V CRISPR-Cas  
203 systems, as these were the only two CRISPR-Cas types present in CAG-217 genomes. Though  
204 *acrIIA22* could not inhibit any of the type V (Cas12-encoding) systems we tested, it did protect a  
205 target plasmid from two substantially diverged type II CRISPR-Cas systems, consistent with the  
206 high prevalence of Cas9-based systems among CAG-217 bacteria (Figure 3C). Such broad-  
207 spectrum inhibition can occur either by targeting a conserved feature of Cas9 or by inhibiting Cas9  
208 via an indirect mechanism that it cannot easily evade.

209 **AcrIIA22 functions via a non-canonical mechanism**

210 Almost all characterized *Acrs* inhibit their cognate Cas proteins via direct binding without the  
211 involvement of additional co-factors. As a result, they exhibit strong inhibitory activity when tested  
212 *in vitro* (Supplemental Table 1). To determine if this was the case for AcrIIA22, we purified it from  
213 *E. coli* and asked whether it could bind and inhibit SpyCas9. To test for binding, we asked whether  
214 twin-strep-tagged AcrIIA22 co-precipitated with untagged SpyCas9 when mixed as purified  
215 proteins. Unlike with AcrIIA4, which binds strongly to SpyCas9 and inhibits its activity *in vitro*, we  
216 detected little to no binding between AcrIIA22 and SpyCas9, regardless of whether a single-guide  
217 RNA (sgRNA) was included or not (Supplemental Figure 6). We also observed that AcrIIA22 had  
218 no impact on SpyCas9's ability to cleave linear, double-stranded DNA (dsDNA), even when  
219 AcrIIA22 was included at substantial molar excess over SpyCas9 (Supplemental Figure 7). These  
220 results suggest that AcrIIA22 cannot bind and inhibit SpyCas9, at least in isolation. Thus, AcrIIA22  
221 lacks the predominant biochemical activities exhibited by previous *Acrs* that have been  
222 mechanistically characterized.

223 We therefore considered the possibility that AcrIIA22 encodes an unconventional anti-  
224 CRISPR that acts via a non-canonical mechanism. However, the only AcrIIA22 homologs we  
225 could detect using BLAST were proteins of unknown function, which provided few clues about  
226 AcrIIA22 activity or biochemical mechanisms. Anticipating that structural homology might provide  
227 better insight into its mechanism of inhibition, we solved AcrIIA22's structure using X-ray  
228 crystallography. We first built a *de novo* model from AcrIIA22's primary sequence with Robetta<sup>25</sup>.  
229 We then used this model as a molecular replacement probe to solve its structure at 2.80 Å  
230 resolution (PDB:7JTA). The asymmetric unit in AcrIIA22's crystal comprises two monomers  
231 stacked end-to-end, with each monomer folding into a four-stranded β-sheet (Figure 4A, Table  
232 1). A DALI structure-structure search revealed that the AcrIIA22 monomer is similar to members

233 of the newly recognized PC4-like structural fold (Figure 4B, Supplemental Table 2). PC4-like  
234 proteins have independently evolved in all domains of life, typically adopt a  $\beta$ - $\beta$ - $\beta$ - $\beta$ - $\alpha$  topology,  
235 and often homodimerize to bind diverse RNA and DNA species using variably positioned  $\beta$ -  
236 sheets<sup>26</sup>.

237 Despite crystallizing as a homodimer, AcrIIA22 migrated from a size exclusion  
238 chromatography (SEC) column at an elution volume corresponding to a calculated mass  
239 approximately four times larger than its expected monomeric molecular weight (Figure 4B). This  
240 suggested that AcrIIA22 may oligomerize *in vivo*. Indeed, AcrIIA22 was predicted to form a stable  
241 tetramer when analyzed with PISA, a tool for inferring macromolecular assemblies from crystal  
242 structures<sup>27</sup> (Figure 4C, Supplemental Figures 8A, 8B). This putative tetramer has a molecular  
243 mass consistent with that observed by SEC and comprises pairs of outward-facing, concave  $\beta$ -  
244 sheets. A series of hydrophobic interactions likely stabilize this configuration of  $\beta$ -sheets instead  
245 of the typical  $\alpha$ -helical interactions seen in other PC4-like proteins, potentially explaining the  
246 absence of an  $\alpha$ -helix in AcrIIA22 (Supplemental Figures 8C, 8D). Interestingly, many PC4-like  
247 proteins bind nucleic acids using similar concave  $\beta$ -sheets, and in some instances form higher-  
248 order oligomers as an obligate step for binding and/or unwinding DNA or RNA<sup>26</sup>. Consistent with  
249 this possibility, AcrIIA22's  $\beta$ -sheets orient along each outward face of the putative tetramer,  
250 resemble those in PC4-like proteins, and form a groove that could potentially accommodate a  
251 nucleic acid substrate (Figure 4D, Supplemental Figures 8A, 8B, 8E). Thus, AcrIIA22's structural  
252 and functional attributes led us to suspect that it could also interact with nucleic acids and  
253 potentially affect their topology.

254 Our tetramer model predicts that an interface at the C-terminus of AcrIIA22 is required for  
255 adjacent  $\beta$ -sheets to bind one another and form a grooved, oligomeric structure (Figures 4C, 4F).  
256 We reasoned that a two-residue, C-terminal truncation of AcrIIA22 would disrupt this interface  
257 (Figure 4F, Supplemental Figure 8G). To test this hypothesis, we examined the oligomeric state  
258 of this 2-aa AcrIIA22 deletion mutant by SEC. Consistent with our hypothesis, we found that the  
259 mutant AcrIIA22 complexes migrated at half the size of the wild-type complexes, corresponding  
260 to approximately twice AcrIIA22's molecular weight (Figure 4B). This suggests that the C-terminal  
261 interface is required to progress from a two to four-membered oligomer, consistent with our model.  
262 Moreover, we found that the 2-aa deletion mutant was also impaired for SpyCas9 antagonism in  
263 our plasmid protection assay (Supplemental Figure 9A). Thus, this C-terminal motif is necessary  
264 for protection from SpyCas9 and for higher-order oligomerization, suggesting that oligomerization  
265 may be necessary for AcrIIA22's anti-SpyCas9 activity.

## 266 **AcrIIA22 is a DNA nickase that relieves torsion of supercoiled plasmids**

267 Our structural analyses indicated that AcrIIA22 is a PC4-like nucleic acid-interacting protein.  
268 Like AcrIIA22, many of the known PC4-like proteins are encoded in phage genomes. Among  
269 these is AcrIIA22's closest structural relative in the PC4-like family: a predicted single-stranded  
270 binding (SSB) protein from phage T5 (Figure 4E)<sup>28</sup>. This putative SSB protein has been predicted  
271 to directly stimulate recombination during the recombination-dependent replication of phage T5's  
272 genome<sup>29</sup>. This prediction, together with our inference from genomic analyses (Figure 2,  
273 Supplemental Figure 4), led us to hypothesize that AcrIIA22 may have similar recombination-  
274 stimulating activity. Indeed, other PC4-like proteins have been observed experimentally to unwind  
275 duplex DNA, a function consistent with their proposed roles in transcription and recombination<sup>26,30</sup>.  
276 Therefore, we investigated whether AcrIIA22 might also similarly interact with duplexed DNA to  
277 affect its topology.

278 We investigated whether we could detect any biochemical effect of *acrIIA22* on a double-  
279 stranded DNA (dsDNA) plasmid *in vivo*. In this experiment, we compared two *acrIIA22* genotypes:  
280 the wild-type sequence and a null mutant with a single base pair change to create an early stop  
281 codon. We grew overnight cultures of plasmids expressing each genotype, purified plasmid DNA,  
282 and analyzed its topology using gel electrophoresis (Figure 5A). As is typical for plasmid  
283 purifications from *E. coli*, the plasmid encoding the null mutant was predominantly recovered in a  
284 supercoiled form. In contrast, *AcrIIA22* expression shifted much of the target plasmid to a slowly  
285 migrating form, consistent with an open-circle conformation. These findings suggest that *AcrIIA22*  
286 expression could relieve plasmid supercoiling, potentially via DNA nicking activity.

287 Though *acrIIA22* expression appeared to alter plasmid topology *in vivo*, DNA topology is a  
288 dynamic process, regulated by many competing factors and dependent on cellular physiology<sup>31</sup>.  
289 Thus, we could not attribute the observed change in plasmid conformation solely to *AcrIIA22*. To  
290 more directly investigate *AcrIIA22*'s effect on plasmid topology, we purified an N-terminal, His6-  
291 tagged *AcrIIA22* protein and examined its impact on a plasmid DNA substrate *in vitro*. By gel  
292 electrophoresis, we observed that *AcrIIA22* shifted a supercoiled plasmid to a slowly migrating  
293 form in a time and concentration-dependent manner (Figure 5B, Supplemental Figure 10D). For  
294 comparison, we also treated a plasmid with the nickase Nb.BssSI, yielding a band that migrated  
295 at the same position as the putatively open-circle product generated via *AcrIIA22* activity (Figure  
296 5B). High concentrations of *AcrIIA22* resulted in conversion of plasmids to a linearized DNA  
297 product, consistent with a nickase-like nuclease activity acting on both strands of DNA (Figure  
298 5B). This nicking activity was strongly stimulated in the presence of Mn<sup>2+</sup>, Co<sup>2+</sup>, and Mg<sup>2+</sup>, weakly  
299 with Ni<sup>2+</sup> and Zn<sup>2+</sup>, and not at all with Ca<sup>2+</sup> (Supplemental Figure 11). To confirm that the observed  
300 gel-shift was the result of nicking activity and not protein-bound DNA, we purified an *AcrIIA22*-  
301 treated plasmid with phenol-chloroform and re-examined it by gel electrophoresis. We observed  
302 that the open-circle form of the plasmid persisted through purification, establishing it as the  
303 product of a *bona-fide* nickase (Supplemental Figure 11). Consistent with our *in vivo* observations  
304 (Supplemental Figure 9A), we found that the 2-aa deletion mutant was impaired for nicking activity  
305 relative to wildtype *AcrIIA22* (Supplemental Figure 9B). These data suggested that *acrIIA22* may  
306 encode for a protein that nicks DNA.

307 No known nuclease has been previously characterized among the PC4-family proteins<sup>26</sup>.  
308 Therefore, to further test our hypothesis that *AcrIIA22* nicks supercoiled plasmids, we performed  
309 several additional experiments. First, we re-purified an N-terminal, His6-tagged *AcrIIA22* protein,  
310 but this time examined individual fractions for nicking activity. Consistent with *AcrIIA22*'s  
311 hypothesized function, nicking activity correlated with *AcrIIA22* concentration across these  
312 fractions (Supplemental Figures 10B, 10C); no co-purifying contaminant was detected via  
313 Coomassie stain (Supplemental Figure 10A). This nicking activity, however, was low enough that  
314 we could not eliminate the possibility that another protein, undetectable via Coomassie stain,  
315 might have co-purified with *AcrIIA22* and could explained this behavior. Reasoning that different  
316 contaminating proteins would result from different purification strategies, we generated a new  
317 version of the *AcrIIA22* protein and purified it via a C-terminal, twin-strep-tag. A more sensitive,  
318 silver-stained gel indicated that this *AcrIIA22* preparation was also very pure (Supplemental  
319 Figure 10E). We subsequently confirmed that it nicked supercoiled plasmids with a specific  
320 activity of 5.1x10<sup>-7</sup> nmol/min/mg (Figures 5C, Supplemental Figures 10G, 10H). This activity is  
321 comparable to other nickases involved in phage-bacterial conflicts (including *SspB*, which nicks  
322 at a rate of 8.9x10<sup>-7</sup> nmol/min/mg)<sup>32</sup>. Notably, this specific activity is significantly higher than we  
323 observed for our original, N-terminal His6-tagged variant (compare *AcrIIA22* concentrations in

324 Figures 5B and 5C). This difference in nicking activity is also reflected in plasmid protection  
325 phenotypes observed *in vivo*; only C-terminally tagged AcrlIA22, but not N-terminally tagged  
326 AcrlIA22, protected a plasmid from SpyCas9 attack (Supplemental Figure 10F). Thus, our studies  
327 find a strong correlation between AcrlIA22's nicking and plasmid protection activities.

328 If AcrlIA22 encoded a true nickase, we hypothesized that we might be able to abrogate this  
329 activity via point mutations in putative catalytic residues. Therefore, we searched for individual  
330 point mutations that impaired nicking activity *in vitro*. If such mutants existed, they would allow us  
331 to test our hypothesis that AcrlIA22 is a nickase. Reasoning that acidic amino acids were likely to  
332 be important catalytic residues<sup>33</sup>, we individually changed each aspartic acid and glutamic acid in  
333 AcrlIA22 to an alanine. Hypothesizing that AcrlIA22's *in vitro* biochemical activity would correlate  
334 with its anti-Cas9 function *in vivo*, we tested whether these alanine variants still inhibited SpyCas9  
335 in our plasmid protection assay. Of the 11 mutants tested, D14A stood out. This mutant showed  
336 clear SpyCas9-dependent plasmid loss, with a >250-fold reduction in plasmid retention compared  
337 to a wild-type AcrlIA22 control (Figure 6A).

338 Purification of the D14A mutant (via a C-terminal twin-strep tag) revealed that it displayed  
339 similar expression level, purification yield, oligomeric size distribution and solution behavior as  
340 wild-type AcrlIA22 (Figure 6B, Supplemental Figure 10E), indicating that the mutant protein is still  
341 properly folded. The D14A mutant was substantially impaired for nicking activity compared to the  
342 wild-type AcrlIA22 protein (Figures 6C, Supplemental Figure 10G), consistent with its diminished  
343 anti-Cas9 activity *in vivo* (Figure 6A). Unlike previous observations with the 2-aa deletion mutant  
344 (Figure 4B), the reduction in nicking for the D14A mutant is unlikely to be the result of oligomeric  
345 differences between it and wild-type AcrlIA22 (Figure 6B). Instead, we speculate that D14 may  
346 contribute to AcrlIA22's nicking activity, as two D14 residues from different AcrlIA22 monomers  
347 sit very near to one another in our proposed tetramer, such that they may be stabilized via the  
348 presence of a divalent cation under physiological conditions (Supplemental Figure 8F).

349 Our surveys of divergent AcrlIA22 homologs also revealed a naturally occurring AcrlIA22  
350 homolog with diminished function *in vivo* (AcrlIA22a, Fig. 3B). Despite encoding for a protein that  
351 differs by only two amino acids from the original sequence (V3I and R30K), *acrlIA22a* was >450-  
352 fold less effective at protecting a plasmid from SpyCas9 than *acrlIA22* (Fig. 3B). We examined  
353 whether this loss of SpyCas9 protection correlated with loss of nicking activity, just like the D14A  
354 mutant. Upon purification, a twin-strep-tagged AcrlIA22a protein eluted with an SEC profile identical  
355 to that of AcrlIA22, suggesting a similar oligomeric state (Figure 6B). Yet, AcrlIA22a exhibited  
356 substantially less nicking activity than wild-type AcrlIA22 *in vitro* (Figure 6C). In our proposed  
357 AcrlIA22 tetramer, R30 likely forms a hydrogen bond with the C-terminus of a diagonal monomer,  
358 raising the possibility that the R30K variant alters the protein's conformational plasticity or  
359 mediates other allosteric effects (Supplemental Figure 8G). As with D14A, the partial loss of  
360 nicking activity seen for AcrlIA22a (Figure 6C) correlated with a partial loss of plasmid protection  
361 against SpyCas9 (Figure 3B). Thus, we describe two closely related AcrlIA22 variants, one  
362 engineered and one naturally occurring, whose nicking activity *in vitro* corresponds directly to  
363 plasmid protection *in vivo*. From these data, along with our other *in vitro* and *in vivo* findings, we  
364 conclude that *acrlIA22* encodes a nickase protein that relieves the torsional stress of supercoiled  
365 plasmids.

366 **AcrlIA22's nicking activity indirectly impairs SpyCas9**

367 Having established that AcrlIA22 is a DNA nickase, we next investigated how this biochemical  
368 activity may enable its inhibition of SpyCas9 without directly binding the Cas protein. We therefore  
369 tested the consequences of expressing AcrlIA22 on a target plasmid in the presence of SpyCas9.  
370 As before, we began by comparing overnight plasmid purifications of a target plasmid expressing  
371 AcrlIA22 and a null mutant with an early stop codon as a negative control. For both genotypes,  
372 we subjected the *acrIIA22*-encoding plasmid to SpyCas9 targeting during bacterial growth. We  
373 were unable to recover the negative control target plasmid after overnight growth, implying that  
374 this target plasmid was eliminated by SpyCas9 (Figure 7A). In contrast, SpyCas9 did not eliminate  
375 a target plasmid that expressed full-length AcrlIA22 (Figure 7A), consistent with AcrlIA22's  
376 capacity to protect against SpyCas9 (Figure 1C).

377 To be effective, a CRISPR-Cas system must eliminate its target at a faster rate than the target  
378 can replicate<sup>34</sup>. Our findings raised the possibility that AcrlIA22 modifies a target plasmid into a  
379 SpyCas9-resistant conformation to win this 'kinetic race' against SpyCas9, potentially shifting the  
380 equilibrium to favor plasmid persistence instead of elimination. To test this kinetic race model, we  
381 asked whether a plasmid that had been pre-treated with AcrlIA22 could resist digestion by  
382 SpyCas9 *in vitro*. Therefore, we purified the open-circle plasmid that resulted from AcrlIA22 pre-  
383 treatment and determined how efficiently it was cleaved by SpyCas9 compared to an unmodified,  
384 supercoiled plasmid (Figure 7B). SpyCas9 showed a clear preference for cleaving the supercoiled  
385 substrate versus the AcrlIA22-treated open-circle plasmid (Figures 7C, 7D, 7E), consistent with  
386 previous reports<sup>13-16</sup>. An open-circle plasmid pre-treated with the nickase Nb.BssSI was similarly  
387 recalcitrant to SpyCas9 digestion (Figures 7C, 7D). Taken together, our findings suggest that  
388 relieving DNA torsion provides the mechanistic explanation for AcrlIA22's ability to inhibit  
389 SpyCas9 *in vivo*.

390 **Discussion**

391 In this study, we identify and characterize *acrIIA22*, a previously undescribed gene that can  
392 antagonize SpyCas9. We show that AcrlIA22 homologs are common in genomes and prophages  
393 of CAG-217 bacteria, which have a high prevalence of Cas9 homologs. Using a combination of  
394 structural and biochemical studies, we show that AcrlIA22 acts by nicking supercoiled DNA to  
395 relieve torsional stress on a target plasmid, and that this activity correlates with protection against  
396 SpyCas9 *in vivo* and *in vitro*. This torsion-based model for SpyCas9 inhibition helps explain why  
397 AcrlIA22 protects plasmids more effectively than phage Mu against SpyCas9. Because plasmids  
398 are maintained as circular, extrachromosomal elements, they are more likely to undergo torsional  
399 change when nicked than the dsDNA genome of phage Mu, which is injected as linear DNA and  
400 spends significant time integrated into *E. coli*'s genome<sup>35</sup>. Additionally, linear DNA experiences  
401 much lower torsional stress and therefore is less susceptible than supercoiled plasmids to  
402 cleavage by SpyCas9<sup>15</sup>. This difference also likely explains why AcrlIA22 failed to protect a linear  
403 dsDNA substrate from SpyCas9 during our earlier *in vitro* experiments (Supplemental Figure 7).

404 Previous *in vitro* experiments indicate that Cas9 requires a higher degree of negative  
405 supercoiling than type I CRISPR-Cas systems to provide the free energy needed for R-loop  
406 formation<sup>13</sup>. Similarly, *in vivo* observations have shown that DNA supercoiling promotes the  
407 recruitment of SpyCas9 to its target site in bacteria<sup>14</sup>. Based on these published findings, we  
408 speculate that Cas9 may be particularly susceptible to changes in DNA torsion among CRISPR-  
409 Cas systems. Thus, factors that modify DNA torsion, like AcrlIA22, could provide a general means  
410 to protect against Cas9 or other enzymes with a strong preference for negative supercoils.

411        Taken together, our data implicate DNA topology as a new battleground in the evolutionary  
412        arms race between CRISPR-Cas systems and MGEs. Because DNA topology is dynamically  
413        regulated in phages, plasmids and other MGEs, many topology-modifying factors already exist in  
414        these genomes. Our findings suggest that at least some of these factors could have secondary  
415        effects on CRISPR-Cas activity and thus prove useful in the context of a molecular arms race<sup>31,36</sup>.  
416        For instance, though not studied in the context of bacterial defense systems, the fitness of phage  
417        T4 is improved via the expression of an accessory protein that modifies DNA supercoiling and the  
418        propensity of R-loops to form<sup>37</sup>. Other phages, such as the intrinsically Cas9-resistant phage T5<sup>38</sup>,  
419        incorporate regular nicks into their genome, the function of which has eluded description for over  
420        40 years<sup>39</sup>. Additionally, conjugative plasmids were recently shown to evade CRISPR-Cas in  
421        *Vibrio cholerae* by the action of homologs of the recombination proteins Red $\beta$  and  $\lambda$ Exo<sup>40</sup>. Based  
422        on our findings, we hypothesize that phages and MGEs targeted by Cas9 exploit factors that  
423        modify DNA topology as a general tactic to evade host immunity.

424        Functional selections like ours are biased towards identifying genes that work well in  
425        heterologous contexts. For example, even though AcrIIA22 is encoded on the genome of a  
426        genetically intractable bacterium, we could identify it using a functional metagenomic selection for  
427        SpyCas9 antagonism in *E. coli*. Although we have characterized its activities in *E. coli* and *in vitro*,  
428        we cannot be certain that AcrIIA22 functions similarly in its native context. Little is known about  
429        the life cycle of native CAG-217 phages, though many dsDNA phage genomes undergo circular,  
430        topologically-constrained stages during their replicative cycles<sup>41</sup>, during which AcrIIA22 might act  
431        to specifically overcome Cas9 immunity. Alternatively, AcrIIA22 may enable Cas9 evasion as a  
432        secondary function related to some other activity. Comparative genomics (Figure 2) and structural  
433        homology to a proposed recombination-stimulating protein of phage T5 suggest a potential role  
434        for AcrIIA22 in recombination, a process which has recently been shown to promote CRISPR-  
435        Cas evasion<sup>40</sup>.

436        Nevertheless, the heterologous behavior of AcrIIA22 in *E. coli* is clearly sufficient for SpyCas9  
437        antagonism *in vivo* and its nicking activity can protect plasmids from SpyCas9 *in vitro*.  
438        Furthermore, AcrIIA22 mutants that are defective for nicking *in vitro* (Figure 6C, Supplemental  
439        Figure 9B) are orders of magnitude less effective at protecting a plasmid from SpyCas9 *in vivo*  
440        (Figures 3B, 6A, Supplemental Figure 9A). This indicates that modest changes in nicking activity  
441        can have major consequences for plasmid survival, which is consistent with our kinetic race model  
442        (Figure 7B) and previous observations that non-linear equilibrium dynamics determine whether  
443        an MGE withstands CRISPR-Cas immunity<sup>34</sup>.

444        Our results suggest that other proteins that affect DNA torsion may also enable Cas9  
445        antagonism. For example, in addition to AcrIIA22, the Nb.BssSI nickase was capable of protecting  
446        a plasmid from SpyCas9 *in vitro*. Yet, despite the regular occurrence of nickases in nature,  
447        functional selections for anti-Cas9 activity have not previously recovered such enzymes<sup>12,42</sup>. We  
448        speculate that AcrIIA22 was identified from a metagenomic library because it treads a balance  
449        between activity and toxicity in *E. coli*; its nicking activity is high enough to antagonize SpyCas9  
450        in a kinetic race, but not so high that it would be toxic to the host cell (Supplemental Figure 1).  
451        Such a balance could result from the inherent activity of the enzyme or via some form of  
452        regulation, either direct or indirect. AcrIIA22's activity is probably also regulated in its native  
453        context to avoid secondary impacts on other essential processes. Potential forms of regulation  
454        include sequence preference, oligomerization, or transient interactions with Cas9 or other host  
455        factors (Figures 4B, 4C). Studies of other phage- and bacterial-encoded nickases may provide

456 further insight into whether AcrIIA22 proteins have additional properties that render them  
457 especially well-suited to antagonize Cas9.

458 Is AcrIIA22 a true anti-CRISPR? AcrIIA22 lacks features that are typical of conventional Acrs,  
459 such as the ability to bind Cas proteins or to inhibit CRISPR-Cas activity as a purified protein.  
460 However, other Acr proteins also lack these features. For example, the well-characterized  
461 SpyCas9 antagonist AcrIIA1 does not inhibit purified SpyCas9, but instead stimulates Cas9  
462 degradation *in vivo*<sup>24</sup>. Similarly, AcrIIA7 does not appear to bind SpyCas9 but can nevertheless  
463 inhibit it via an unknown mechanism *in vitro*<sup>42</sup>. Indeed, anti-CRISPR proteins are defined by a  
464 common strategy and outcome rather than by a common biochemical mechanism. Our finding  
465 that *AcrIIA22* is encoded by prophages as a single gene that strongly protects plasmids and  
466 partially protects phages from SpyCas9 (Figure 3B, Supplemental Figure 3) makes it much more  
467 similar to other Acrs<sup>23</sup> and distinct from non-canonical CRISPR-Cas evasion strategies like DNA  
468 glucosylation<sup>6</sup>.

469 Although it can protect phage Mu from SpyCas9, AcrIIA22 does not appear to provide the  
470 same potency of Cas9 inhibition as some other characterized Acrs. However, potent inhibition is  
471 not a pre-requisite for effective anti-CRISPR activity. In nature, multiple phages can cooperate to  
472 overcome Cas9 immunity by each contributing some anti-CRISPR protein to overcome a common  
473 foe<sup>43,44</sup>. These dynamics can favor weak anti-CRISPRs over strong ones, as the latter permits a  
474 higher incidence of cheater phages (those without anti-CRISPRs) to persist in mixed phage  
475 populations<sup>45</sup>. Thus, even in cases where AcrIIA22 only weakly inhibits Cas9 (Supplemental  
476 Figure 3), it may nonetheless confer substantial benefit. Additionally, slowing down Cas9  
477 cleavage could increase the time and probability for escape mutants to arise (e.g. Cas9 target-  
478 site variants<sup>1</sup>, deletion mutants<sup>40</sup>), allow for additional Acr expression<sup>43,44</sup>, or permit further  
479 genome replication to overwhelm CRISPR-Cas immunity<sup>34</sup>. This phenomenon – weak inhibition  
480 giving rise to long-term resistance – is reproducibly observed in cases of strong selective  
481 pressure. For instance, in the context of antibiotic resistance, the expression of QNR pentapeptide  
482 proteins by many human pathogens can provide low-level drug tolerance, extend survival, and  
483 allow time for additional mutations to develop that completely resist quinolone antibiotics<sup>46</sup>.

484 As the use of functional metagenomics to study phage-bacterial conflicts grows more  
485 common, many novel genes and mechanisms for CRISPR-Cas inhibition are likely to be  
486 described<sup>12,42</sup>. Like AcrIIA22, which has no homology to any previously described anti-CRISPR  
487 and lacks other genetic signatures used for *acr* discovery (e.g., linkage with helix-turn-helix  
488 transcription factors)<sup>47,48</sup>, these new genes may not exhibit canonical Acr behaviors. It is inevitable  
489 that these discoveries will lead to a more nuanced understanding of the arms race between  
490 CRISPR-Cas systems and MGEs. These findings will also reveal undiscovered strategies for  
491 molecular antagonism and new battlegrounds in the age-old conflict between bacteria and their  
492 phages.

493 **Methods**

494 **Plasmid protection assay**

495 All plasmid protection assays were done in *Escherichia coli* (strain: NEB Turbo). As  
496 described previously<sup>12</sup>, SpyCas9 was expressed via the arabinose-inducible promoter pBAD on  
497 a CloDF13-based plasmid marked with a spectinomycin resistance cassette. The SpyCas9  
498 construct, called pSpyCas9\_crA, was designed to eliminate a target vector with a kanamycin  
499 resistance cassette. This target vector also expressed a gene-of-interest (e.g., an *acr*) via the  
500 doxycycline-inducible pLtetO-1 promoter (Supplemental Table 4). We induced expression from  
501 the target vector via depression of the TetR transcription factor with doxycycline (we generically  
502 named this vector pZE21\_tetR; Supplemental Table 4). IPTG was used in samples with the target  
503 vector to ensure high levels of TetR expression (which was driven by the lac promoter) and thus  
504 inducible control of our gene of interest. Unless noted in Supplemental Table 5, all genes,  
505 including each alanine mutant depicted in Figure 6A, were synthesized by Synbio technologies  
506 and cloned directly into pZE21\_tetR for functional testing.

507 Cultures of each sample were grown overnight at 37°C with shaking at 220 rpm in lysogeny  
508 broth (LB; 10 g/L casein peptone, 10 g/L NaCl, 5 g/L ultra-filtered yeast powder) containing  
509 spectinomycin 50 µg/ml, kanamycin 50 µg/ml, and 0.5mM IPTG. These growth conditions kept  
510 both SpyCas9 and the gene of interest in uninduced states. The next morning, overnight cultures  
511 were diluted 1:50 into LB broth containing spectinomycin (at 50 µg/ml), kanamycin (at 50 µg/ml),  
512 0.5mM IPTG, and doxycycline 100 ng/ml to induce the gene of interest. Cultures were grown at  
513 37°C on a roller drum to mid-log phase (for approximately 1.5 hours to OD600 of 0.3-0.6). Once  
514 cells reached mid-log phase, they were diluted to OD600 value of 0.01 into two media types: (a)  
515 LB containing spectinomycin 50 µg/ml, 0.5mM IPTG, and doxycycline 100 ng/ml, and (b) LB  
516 containing spectinomycin 50 µg/ml, 0.5mM IPTG, doxycycline 100 ng/ml, and 0.2% (L) arabinose.  
517 These media induced either the gene of interest alone, or both the gene of interest and SpyCas9,  
518 respectively. Each sample was grown in triplicate in a 96 well plate in a BioTek Cytation 3 plate  
519 reader. After 6 hours of growth at 37°C with shaking at 220 rpm, each sample was diluted ten-  
520 fold and plated on two types of media: (a) LB spectinomycin 50 µg/ml + 0.5mM IPTG or (b) LB  
521 spectinomycin 50 µg/ml, kanamycin 50 µg/ml, 0.5mM IPTG. Plates were incubated at 37°C  
522 overnight. Then, colonies were counted to determine the fraction of colony forming units (cfus)  
523 that maintained kanamycin resistance (and thus the target vector). All figures depicting these data  
524 show the log-transformed proportion of Kan<sup>R</sup>/total cfu, with or without SpyCas9 induction. The  
525 growth curves in Supplemental Figure 1 match the experiment depicted in Figure 1C for the  
526 uninduced SpyCas9 samples. For the uninduced *orf\_1* control samples, doxycycline was omitted  
527 from media throughout the experiment. Growth rates referenced in the text and in Supplemental  
528 Figure 1 were calculated using the slope of the OD600 growth curves during log phase, following  
529 a natural log transformation.

530 To test AcrlIA22 function against a panel of Cas9 and Cas12 orthologs in Figure 3C, we  
531 used a slightly modified, three-plasmid setup. As before, *spyCas9*, *nmCas9*, *fnCas12* and  
532 *lbCas12* were encoded in a CloDF13-based plasmid with a spectinomycin resistance cassette.  
533 Expression of the Cas effector was controlled by promoter J23100 and a theophylline riboswitch.  
534 The accompanying gRNAs were encoded in a separate set of plasmids called pDual4 under an  
535 arabinose expression system, in a p15A-based plasmid and a chloramphenicol resistance  
536 cassette (Supplemental Table 4). The gRNAs in the different pDual4 constructs were  
537 programmed to target the kanamycin-marked target plasmid in the same manner as

538 pSpyCas9\_crA. All assays were done in *Escherichia coli* (strain: NEB Turbo) following the same  
539 plasmid protection assay described previously. However, in this case, we induced expression of  
540 the different Cas effectors and gRNAs, by adding 2 mM theophylline and 0.2% (L) arabinose,  
541 respectively, to the media.

#### 542 **Impact of AcrIIA22 on GFP expression**

543 We swapped *spyCas9* for *egfp* in our CloDF13-based plasmid and co-expressed AcrIIA22  
544 to determine if AcrIIA22 impacted expression from this construct. If AcrIIA22 influenced CloDF13's  
545 copy number or the transcription of *spyCas9*, we anticipated that it would also impact GFP levels  
546 in this construct (pCloDF13\_GFP; Supplemental Table 4). To perform this experiment, we co-  
547 transformed pCloDF13\_GFP and pZE21\_tetR encoding *acrIIA22* into *E. coli* Turbo. Single  
548 colonies were picked into 4 ml of LB containing spectinomycin at 50 µg/ml ('spec50') and  
549 kanamycin at 50 µg/ml ('kan50') and 0.5mM IPTG and grown overnight at 37°C shaking at  
550 220rpm. The next morning the overnight culture was diluted 1:50 into both LB spec50 Kan50 +  
551 0.5mM IPTG with or without doxycycline (to induce *acrIIA22*) and grown at 37°C for about 1.5  
552 hours to mid-log phase (OD600 0.2-0.6). The OD600 was measured, and all samples were diluted  
553 to OD600 of 0.01 in two media types: (a) LB spec50 + kan50 + 0.5mM IPTG + 0.2% arabinose  
554 (inducing *gfp* only) or (b) LB spec50 + kan50 + 0.5mM IPTG + 0.2% arabinose + 100ng/ml  
555 doxycycline (inducing *gfp* and *acrIIA22*). A volume of 200 µl of each sample was then transferred  
556 to a 96-well plate in triplicate and GFP fluorescence was measured every 15 minutes for 24 hours  
557 (GFP was excited using 485 nm light and emission detected via absorbance at 528 nm). In  
558 parallel, we included control samples that lacked the kanamycin-marked plasmid and varied  
559 whether doxycycline was added or not (at 100 ng/ml). In these control samples, we noticed that  
560 doxycycline slightly diminished GFP expression (it is possible that sub-lethal levels of the  
561 antibiotic may still depress translation). Thus, we normalized GFP fluorescence measurements in  
562 our experiment with AcrIIA22 to account for this effect in all samples containing doxycycline.  
563 These normalized fluorescence measurements are shown in Supplemental Figure 2B.

#### 564 **Western blots to determine AcrIIA22's impact on SpyCas9 expression**

565 We grew overnight cultures of *E. coli* Turbo that expressed pSpyCa9\_crNT and  
566 pZE21\_tetR encoding a gene of interest (Supplemental Tables 4, 5) in LB spec50 + kan50 +  
567 0.5mM IPTG. The next morning, we diluted these cultures 1:100 in 4ml of either (a) LB spec50 +  
568 kan50 + 0.5mM IPTG or (b) LB spec50 + kan50 + 0.5mM IPTG + 100 ng/ml doxycycline (to induce  
569 the gene of interest). We included samples that expressed either *acrIIA22* or *gfp* as a gene of  
570 interest. In all SpyCas9 constructs, we used a crRNA that did not target our plasmid backbone  
571 (pSpyCa9\_crNT) to ensure that *acrIIA22* expression remained high and its potential impact on  
572 SpyCas9 expression levels would be most evident. All samples were grown for two hours at 37°C  
573 to reach mid-log phase (OD600 0.3 to 0.5) and transferred into media that contained 0.2%  
574 arabinose to induce SpyCas9. At transfer, volumes were normalized by OD600 value to ensure  
575 that an equal number of cells were used (diluted to a final OD600 of 0.05 in the arabinose-  
576 containing medium). This second medium either contained or lacked 100 ng/ml doxycycline to  
577 control expression of *acrIIA22* or *gfp*, as with the initial media. Throughout this experiment, we  
578 included a control strain that lacked pZE21\_tetR and only expressed SpyCas9. Kanamycin and  
579 doxycycline were omitted from its growth media. For this control strain, we also toggled the  
580 addition of arabinose in the second growth medium to ensure that positive and negative controls  
581 for SpyCas9 expression were included in our experiment. After three hours and six hours of  
582 SpyCas9 induction, OD600 readings were again taken and these values used to harvest an equal

583 number of cells per sample (at three hours, OD600 values were between 0.76 and 0.93 and  
584 0.75ml to 0.9ml volumes harvested; at six hours 0.4ml was uniformly harvested as all absorbance  
585 readings were approximately 1.6).

586 All samples were centrifuged at 4100g to pellet cells, resuspended in 100  $\mu$ l of denaturing  
587 lysis buffer (12.5 mM Tris-HCl, pH 6.8; 4% SDS), and passed through a 25 gauge needle several  
588 times to disrupt the lysate. Samples were then boiled at 100°C for 10 minutes, spun at 13,000  
589 rpm at 4°C for 15 minutes and the supernatants removed and frozen at -20°C. The next day, 12  
590  $\mu$ l of lysate was mixed with 4  $\mu$ l of 4x sample buffer (200 mM Tris-HCl, 8% SDS, 40% glycerol,  
591 200 mM DTT, and 0.05% bromophenol blue) and boiled at 100°C for 10 minutes. Then, 10  $\mu$ l  
592 sample was loaded onto a BioRad Mini-Protean “any KD Stain Free TGX” gel (cat. #4569035)  
593 and run at 150V for 62 minutes. To verify that equivalent amounts of each sample were run, gels  
594 were visualized on a BioRad chemidoc for total protein content. Protein was then transferred to a  
595 0.2  $\mu$ M nitrocellulose membrane using the Bio-Rad Trans-Blot Turbo system (25 V, 1.3 A for 10  
596 min). We then washed membranes in PBS/0.1% Triton-X before incubating them with a mixture  
597 of the following two primary antibodies, diluted in in LI-COR Odyssey Blocking Solution (cat.  
598 #927-40000): (i) monoclonal anti-SpyCas9, Diagenode cat. #C15200229-50, diluted 1:5,000; (ii)  
599 polyclonal anti-GAPDH, GeneTex cat. # GTX100118, diluted 1:5,000. The GAPDH antibody  
600 served as a loading control and a second check to ensure equal protein levels were run.  
601 Membranes were left shaking overnight at 4°C, protected from light. Then, membranes were  
602 washed four times in PBS/0.1% Triton-X (ten-minute washes) before they were incubated for 30  
603 minutes at room temperature with a mixture of secondary antibodies conjugated to infrared dyes.  
604 Both antibodies were diluted 1:15,000 in LI-COR Odyssey Blocking Solution. To detect SpyCas9,  
605 the following secondary antibody was used: IR800 donkey, anti-mouse IgG, LI-COR cat# 926-  
606 32212. To detect GAPDH, IR680 goat, anti-rabbit IgG, LI-COR cat# 926-68071 was used. Blots  
607 were imaged on a LI-COR Odyssey CLx after three additional washes.

## 608 Phage plaquing assay

609 We grew overnight cultures of *E. coli* Turbo expressing pSpyCa9\_crMu and pZE21\_tetR  
610 encoding a gene of interest (Supplemental Tables 4, 5) at 37°C in LB spec50 + kan50 + 0.5 mM  
611 IPTG. Genes of interest were either *acrIIA4*, *gfp*, or *acrIIA22*. The pSpyCas9 construct targeted  
612 phage Mu and was previously demonstrated to confer strong anti-phage immunity in this  
613 system<sup>12</sup>. A control strain expressing pZE21-tetR-gfp and SpyCas9\_crNT (which encoded a  
614 CRISPR RNA that does not target phage Mu) was grown similarly. The next morning, all cultures  
615 were diluted 50-fold into LB spec50 + kan50 + 0.5 mM IPTG + 5 mM MgCl2 and grown at 37°C  
616 for three hours. Then, doxycycline was added to a final concentration of 100 ng/ml to induce the  
617 gene of interest. Two hours later, SpyCas9 was induced by adding a final concentration of 0.2%  
618 w/v arabinose. Two hours after that, cultures were used in soft-agar overlays on one of two media  
619 types, discordant for arabinose, to either maintain SpyCas9 expression or let it fade as arabinose  
620 was diluted in top agar and consumed by the host bacteria (per Supplemental Figure S2). Top  
621 and bottom agar media were made with LB spec50 + kan50 + 0.5 mM IPTG + 5 mM MgCl2. In  
622 cases where SpyCas9 expression was maintained, arabinose was also added at a final  
623 concentration of 0.02% to both agar types. Top agar was made using 0.5% Difco agar and bottom  
624 agar used a 1% agar concentration. For the plaquing assay, 100  $\mu$ l of bacterial culture was mixed  
625 with 3 ml of top agar, allowed to solidify, and ten-fold serial dilutions of phage Mu spotted on top  
626 using 2.5  $\mu$ l droplets. After the droplets dried, plates were overturned and incubated at 37°C  
627 overnight before plaques were imaged the following day.

628 **Identification of AcrIIA22 homologs and hypervariable genomic islands**

629 We searched for AcrIIA22 homologs in three databases: NCBI nr, IMG/VR, and a set of  
630 assembled contigs from 9,428 diverse human microbiome samples<sup>18</sup>. Accession numbers for the  
631 NCBI homologs are indicated on the phylogenetic tree in Figure 3A. We retrieved AcrIIA22  
632 homologs via five rounds of an iterative PSI-BLAST search against NCBI nr performed on October  
633 2<sup>nd</sup>, 2017. In each round of searching, at least 90% of the query protein (the original AcrIIA22 hit)  
634 was covered, 88% of the subject protein was covered, and the minimum amino acid identity of an  
635 alignment was 23% (minimum 47% positive residues; e-value ≤ 0.001). Only one unique AcrIIA22  
636 homolog was identified in IMG/VR (from several different phage genomes) via a blastp search  
637 against the July, 2018 IMG/VR proteins database (using default parameters). This homolog was  
638 also found in other databases and its amino acid sequence is identical to that of AcrIIA22b (Figure  
639 3A).

640 Most unique AcrIIA22 homologs were identified in the assembly data of over 9,400 human  
641 microbiomes performed by Pasolli and colleagues<sup>18</sup>. These data are grouped into multiple  
642 datasets: (i) the raw assembly data, and (ii) a set of unique species genome bins (SGBs), which  
643 were generated by first assigning species-level phylogenetic labels to each assembly and then  
644 selecting one representative genome assembly per species. We identified AcrIIA22 homologs  
645 using several queries against both databases. First, we performed a tblastn search against the  
646 SGB database using the AcrIIA22 sequence as a query, retrieving 141 hits from 137 contigs. A  
647 manual inspection of the genome neighborhoods for these hits revealed that most homologs  
648 originated from a short, hypervariable genomic island; some homologs were encoded by  
649 prophages. No phage-finding software was used to identify prophages; they were apparent from  
650 a manual inspection of the gene annotations that neighbored *acrIIA22* homologs (see the section  
651 entitled “Annotation and phylogenetic assignment of metagenomic assemblies” for details).

652 To find additional examples of AcrIIA22 homologs and of these genomic islands, we then  
653 queried the full raw assembly dataset. To do so without biasing for *acrIIA22*-encoding sequences,  
654 we used the *purF* gene that flanked *acrIIA22*-encoding genomic islands as our initial query  
655 sequence. Specifically, we used the *purF* gene from contig number 1 in Supplemental Table 3;  
656 its sequence is also in Supplemental Table 5. To consider only the recent evolutionary history of  
657 this locus, we required all hits have ≥98% nucleotide identity and required all hits to be larger than  
658 15 kilobases in length to ensure sufficient syntenic information. From these contigs, we further  
659 filtered for those that had ≥98% nucleotide identity to *radC*, the gene which flanked the other end  
660 of *acrIIA22*-encoding genomic islands. Again, we used the variant from contig number 1 in  
661 Supplemental Table 3; its sequence is also in Supplemental Table 5. In total, this search yielded  
662 258 contig sequences; nucleotide sequences and annotations for these contigs are provided in  
663 Supplemental Dataset 5. We then searched for *acrIIA22* homologs in these sequences using  
664 tblastn, again observing them in genomic islands and prophage genomes (which were assembled  
665 as part of the 258 contigs). In total, this search revealed 320 *acrIIA22* homologs from 258 contigs.  
666 The 258 genomic islands from these sequences were retrieved manually by extracting all  
667 nucleotides between the *purF* and *radC* genes. These extracted sequences were then clustered  
668 at 100% nucleotide identity with the sequence analysis suite Geneious Prime 2020 v1.1 to identify  
669 128 unique genomic islands.

670 Altogether, our two searches yielded 461 AcrIIA22 sequences from these metagenomic  
671 databases that spanned 410 contig sequences. The 461 AcrIIA22 homologs broke down into two  
672 groups: 410 clustered with genomic island-like sequences whereas 51 clustered with prophage-

673 like homologs. In nature, the relative prevalence of *AcrlIA22* in genomic islands or prophages may  
674 not be accurately reflected by these numbers because we never directly searched for prophage-  
675 encoded homologs. We then combined these 461 *AcrlIA22* sequences with those from NCBI and  
676 IMG/VR and clustered the group on 100% amino acid identity to reveal 30 unique proteins. To  
677 achieve this, we used the software cd-hit<sup>49</sup> with the following parameters: -d 0 -g 1 -aS 1.0 -c 1.0.  
678 These 30 sequences were numbered to match one of their parent contigs (as indicated in  
679 Supplemental Table 3) and used to create the phylogenetic tree depicted in Figure 3A. For  
680 *AcrlIA22* homologs found outside NCBI, the nucleotide sequences and annotations of their parent  
681 contigs can be found in Supplemental Datasets 1 and 2. For NCBI sequences, accession  
682 numbers are shown in Figure 3A. The gene sequences used in functional assays (Figure 3B)  
683 have been reprinted in Supplemental Table 5, for convenience.

684 **Annotation and phylogenetic assignment of metagenomic assemblies**

685 Contig sequences from IMG/VR, the Pasolli metagenomic assemblies, and some NCBI  
686 entries lacked annotations, making it difficult to make inferences about *acrlIA22*'s genomic  
687 neighborhood. To facilitate these insights, we annotated all contigs as follows. We used the gene-  
688 finder MetaGeneMark<sup>50</sup> to predict open reading frames (ORFs) using default parameters. We  
689 then used their amino acid sequences in a profile HMM search with HMMER3<sup>51</sup> against  
690 TIGRFAM<sup>52</sup> and Pfam<sup>53</sup> profile HMM databases. The highest scoring profile was used to annotate  
691 each ORF. We annotated these contigs to facilitate genomic neighborhood analyses for *acrlIA22*;  
692 these are not intended to provide highly accurate functional predictions of their genes. Thus, we  
693 erred on the side of promiscuously assigning gene function; our annotations should therefore be  
694 treated with appropriate caution. A visual inspection of these annotated contigs made apparent  
695 several examples of *acrlIA22*-encoding prophages (we noticed 35-40 kilobase insertions in some  
696 contigs that were otherwise nearly identical to those without prophages). We were confident that  
697 these insertions were prophages because they contained mostly co-linear genes with key phage  
698 functions annotated. As a simple means to sample this phage diversity, we manually extracted  
699 nine examples of these prophage sequences (their raw sequences and annotated genomes can  
700 be found in Supplemental Datasets 3 and 4). Annotations were imported into the sequence  
701 analysis suite Geneious Prime 2020 v1.1 for manual inspection of genome neighborhoods.

702 We used the genome taxonomy database (GTDB) convention for all sequences discussed  
703 in this manuscript<sup>54</sup>. In part, this was because all *acrlIA22* genomes are found in clostridial  
704 genomes, which are notoriously polyphyletic in NCBI taxonomies (for instance, species in the  
705 NCBI genus *Clostridium* appear in 121 GTDB genera and 29 GTDB families)<sup>55</sup>. All SGBs that we  
706 retrieved from the Pasolli assemblies were assigned taxonomy as part of that work and were  
707 called *Clostridium* sp. CAG-217. Similarly, NCBI assemblies that encoded the most closely  
708 *acrlIA22* homologs to our original hit were assigned to the GTDB genus CAG-217<sup>54,55</sup>. The raw  
709 assembly data from the Pasolli database was not assigned a taxonomic label but was nearly  
710 identical in nucleotide composition to the CAG-217 contigs (Figure 2, Supplemental Figure 4,  
711 Supplemental Datasets 1 and 2). Therefore, we also refer to these sequences as originating in  
712 CAG-217 genomes but take care to indicate which assemblies have been assigned a rigorous  
713 taxonomy and which ones for which taxonomy has been inferred in this fashion (Supplemental  
714 Table 3).

715 **Comparing genes in genomic islands to phage genomes**

716 We first examined the annotated genes within each of the 128 unique genomic islands.  
717 Manual inspection revealed 54 unique gene arrangements that differed in gene content and  
718 orientation. We then selected one representative from each arrangement and extracted amino  
719 acid sequences from each encoded gene (n=506). Next, we collapsed these 506 proteins into  
720 orthologous groups by clustering at 65% amino acid using cd-hit with the following parameters: -  
721 d 0 -g 1 -aS 0.95 -c 0.65. These cluster counts were used to generate the histogram depicted in  
722 Supplemental Figure 4C. To determine which protein families may also be phage-encoded, we  
723 queried the longest representative from each cluster with at least two sequences against the  
724 database of nine CAG-217 phages described in the section entitled “Annotation and phylogenetic  
725 assignment of metagenomic assemblies”. We used tblastn with default parameters to perform this  
726 search, which revealed that some proteins in the CAG-217 genomic islands have homologs in  
727 prophage genomes that are out-of-frame with respect to the MetaGeneMark annotations depicted  
728 in Supplemental Figure 4A.

## 729 **Phylogenetic tree of *AcrlIA22* homologs**

730 The 30 unique *AcrlIA22* homologs we retrieved were used to create the phylogeny  
731 depicted in Figure 3A. These sequences were aligned using the sequence alignment tool in the  
732 sequence analysis suite Geneious Prime 2020 v1.1. This alignment is provided as Supplemental  
733 Dataset 6. From this alignment, the phylogenetic tree in Figure 3A was generated using PhyML  
734 with the LG substitution model<sup>56</sup> and 100 bootstraps. Coloration and tip annotations were then  
735 added in Adobe Illustrator.

## 736 **Identification of CRISPR-Cas systems and Acrs in CAG-217 assemblies**

737 To determine the type and distribution of CRISPR-Cas systems and Acrs in CAG-217  
738 genomes, we downloaded all assembly data for the 779 SGBs assigned to CAG-217 in Pasolli  
739 *et. al*<sup>8</sup> (bin 4303). We then predicted CRISPR-Cas systems for all 779 assemblies in bulk using  
740 the command line version of the CRISPR-Cas prediction suite, cctyper<sup>57</sup>. Specifically, we used  
741 version 1.2.1 of cctyper with the following options: --prodigal meta --keep\_tmp. To identify type II-  
742 A Acrs, we first downloaded representative sequences for each of the 21 experimentally  
743 confirmed type II-A Acrs from the unified resource for tracking anti-CRISPRs<sup>58</sup>. We then used  
744 tblastn to query these proteins against the 779 CAG-217 genome bins and considered any hit  
745 with e-value better than 0.001 (which included all hits with >30% identity across 50% of the query).  
746 To check if these Acrs were present in *acrlIA22*-encoding phages, we performed an identical  
747 tblastn search, but this time using the set of nine *acrlIA22*-encoding prophages as a database.

## 748 **Recombinant protein overexpression and purification**

749 The *AcrlIA22* protein and its mutants were codon optimized for *E. coli* (Genscript or SynBio  
750 Technologies) and the gene constructs were cloned into the pET15HE or pET15b plasmid<sup>12</sup> to  
751 contain an N-terminal, thrombin-cleavable 6XHistidine (His6) tag. These plasmids differ by only a  
752 few bases just upstream of the N-terminal thrombin tag. For purified, twin-strep tagged proteins,  
753 constructs were cloned into a modified pET15b that lacks the N-terminal tag but instead has a C-  
754 terminal twin-strep tag (Supplemental Table 4). Constructs were transformed and overexpressed  
755 in BL21 (DE3) RIL or BL21 (DE3) pLysS *E. coli* cells. A 10 mL overnight culture (grown in LB +  
756 100 µg/mL ampicillin) was diluted 100-fold into the same media and grown at 37°C with shaking  
757 to an OD600 of 0.8 for His6-tagged constructs and 0.3 for twin-strep-tagged constructs.  
758 Expression was then induced with 0.5 mM IPTG. For His6-tagged constructs, the culture was

759 shaken for an additional 3 hours at 37°C; twin-strep-tagged constructs were induced at 16C for  
760 22 hours. Cells were harvested by centrifugation and the pellet stored at -20°C.

761 Cell pellets for His6-tagged constructs were resuspended in 25 mM Tris, pH 7.5, 300 mM  
762 NaCl, 20 mM imidazole; twin-strep tagged constructs were resuspended in Tris 100nM 8.0 pH,  
763 150mM NaCl, 1mM EDTA. Cells were lysed by sonication on ice. The lysate was centrifuged in  
764 an SS34 rotor at 18,000 rpm for 25 minutes, followed by filtering through a 5 µm syringe filter for  
765 the His6-tagged constructs and a 0.45 µM syringe filter for the twin-strep-tagged constructs.

766 To purify His6-tagged constructs, the clarified lysate was bound using the batch method to Ni-  
767 NTA agarose resin (Qiagen) at 4°C for 1 hour. The resin was transferred to a gravity column  
768 (Biorad), washed with >50 column volumes of Lysis Buffer, and eluted with 25 mM Tris, pH 7.5,  
769 300 mM NaCl, 200 mM imidazole. The protein was diluted with 2 column volumes of 25 mM Tris,  
770 pH 7.5 and purified on a HiTrapQ column (GE Healthcare) using a 20 mL gradient from 150 mM  
771 to 1 M NaCl in 25 mM Tris, pH 7.5. Peak fractions were pooled, concentrated, and buffer  
772 exchanged into 200 mM NaCl, 25 mM Tris, pH 7.5 using an Amicon Ultra centrifugal filter with a  
773 3,000 molecular weight cutoff (Millipore, UFC900324), then cleaved in an overnight 4°C  
774 incubation with biotinylated thrombin (EMD Millipore). Streptavidin agarose slurry (Novagen) was  
775 incubated with cleaved protein at 4°C for 30 minutes to remove thrombin. The sample was then  
776 passed through a 0.22 µm centrifugal filter and loaded onto a HiLoad 16/60 Superdex 200 prep  
777 grade size exclusion column (Millipore Sigma) equilibrated in 25 mM Tris, pH 7.5, 200 mM NaCl.  
778 The peak fractions were pooled, concentrated, and confirmed for purity by SDS-PAGE before use  
779 in most assays. Figure 4B depicts size exclusion chromatography data generated for thrombin-  
780 cleaved AcrIIA22 variants generated using a Superdex75 16/60 (GE HealthCare) column with 25  
781 mM Tris, pH 7.5, 200mM NaCl. To correlate nicking activity with protein content across fractions  
782 (Supplemental Figure 10B), we collected 13 fractions that span the entire elution peak as well as  
783 fractions without AcrIIA22 protein. The protein gel shown in Supplemental Figures 10A and 10B  
784 was loaded with 5ul of each concentrated fraction.

785 For two additional proteins, we also performed similar Ni-NTA-based purifications of His6-  
786 tagged constructs, with small deviations from the protocol described in the preceding paragraph.  
787 Recombinant AcrIIA4 was purified similarly to other His6-tagged Acr proteins but with the  
788 following deviations, as previously described<sup>12</sup>. IPTG was used at 0.2 mM and cells were  
789 harvested after 18 hours of induction at 18°C. Thrombin cleavage also occurred at 18°C. This  
790 untagged version was used to help generate Supplemental Figure 6. Peak fractions for all proteins  
791 were pooled, concentrated, flash frozen as single-use aliquots in liquid nitrogen, and stored at  
792 -80°C. SpyCas9 was expressed in *E. coli* from plasmid pMJ806 (addgene #39312) to contain a  
793 TEV-cleavable N-terminal 6XHis-MBP tag and was purified as described previously<sup>12</sup> with  
794 sequential steps of purification consisting of Ni-NTA affinity chromatography, TEV cleavage,  
795 Heparin HiTrap chromatography, and SEC. The protein was stored in a buffer consisting of 200  
796 mM NaCl, 25 mM Tris (pH 7.5), 5% glycerol, and 2 mM DTT. Again, peak fractions were pooled,  
797 concentrated, and flash frozen as single-use aliquots.

798 We also purified AcrIIA22 and AcrIIA4 constructs with a C-terminal twin-strep tag. The protein  
799 was expressed and lysed as described above and purified according to the manufacturer's  
800 guidelines (IBA Life Sciences, Inc.). Clarified lysates were passed over Strep-Tactin-Sepharose  
801 resin using a gravity filtration column. The flow through was passed over the resin a second time.  
802 The column was washed with a minimum of 20 column volumes of buffer W, followed by elution  
803 in buffer E (150 mM NaCl, 100 mM Tris, pH 8.0 mM, 1 EDTA, 2.5 mM desthiobiotin). The eluted

804 protein was purified over a HiTrapQ column (GE Healthcare) using a 40 mL gradient from 150  
805 mM to 0.5 M NaCl in 25 mM Tris, pH 7.5. Peak fractions were pooled and then purified again via  
806 size exclusion chromatography with a Biorad Enrich SEC650 10x300mm column in 150mM NaCl,  
807 25 mM Tris, pH 7.5. These elution data are shown for AcrlIA22 and its variants in Figure 6B.  
808 Fractions were collected across the elution peak and confirmed for purity via silver stain  
809 (Supplemental Figure 10E), per manufacturer's recommendations (Thermo Fisher Cat. No.  
810 24612). For these proteins, we chose fraction number four to carry forward, as it eluted at  
811 approximately four times the monomer's molecular weight, consistent with our proposed tetramer,  
812 which is depicted in Figure 4C. Protein was then concentrated and flash frozen as single-use  
813 aliquots for later use.

#### 814 **X-ray crystallography and structural analyses**

815 An AcrlIA22 crystal was grown using 14mg/mL protein via the hanging drop method using  
816 200mM ammonium nitrate, 40% (+/-)-2-methyl-2,4-pentanediol (MPD, Hampton Research),  
817 10mM MgCl<sub>2</sub> as a mother liquor. Diffraction data was collected at the Argonne National  
818 Laboratory Structural Biology Center synchrotron facility (Beamline 19BM). Data was processed  
819 with HKL2000 in space group P4332, then built and refined using COOT<sup>59</sup> and PHENIX<sup>60</sup>. The  
820 completed 2.80Å structure was submitted to the Protein Data Bank with PDB Code 7JTA. The  
821 detailed PDB validation report is provided (Supplemental Dataset 7). We submitted this finished  
822 coordinate file to the PDBe PISA server (Protein Data Bank Europe, Protein Interfaces, Surfaces  
823 and Assemblies; <http://pdbe.org/pisa/>) which uses free energy and interface contacts to calculate  
824 likely multimeric assemblies<sup>27</sup>. The server calculated tetrameric, dimeric and monomeric  
825 structures to be thermodynamically stable in solution. The tetrameric assembly matches the  
826 molecular weight expected from the size exclusion column elution peak and is the most likely  
827 quaternary structure as calculated by the PISA server. The tetramer gains -41.8 kcal/mol free  
828 energy by solvation when formed and requires an external driving force of 3.1 kcal/mol to  
829 disassemble it according to PISA  $\Delta G$  calculations.

#### 830 **sgRNA generation**

831 The single-guide RNA (sgRNA) for use in *in vitro* experiments was generated as described  
832 previously<sup>12</sup>. We made the dsDNA template via one round of thermal cycling (98°C for 90 s, 55°C  
833 for 15 s, 72°C for 60 s) in 50 µl reactions. We used the Phusion PCR polymerase mix (NEB)  
834 containing 25 pmol each of the following two oligo sequences; the sequence that binds the  
835 protospacer on our pIDTsmart target vector is underlined:

836 (i) GAAATTAAATACGACTCACTATAGGTAAATGAAATAAGATCACTACGTTTAGAGCT  
837 AGAAATAGCAAGTTAAATAAGGCTAGTCG  
838 (ii) AAAAAAGCACCGACTCGGTGCCACTTTCAAGTTGATAACGGACTAGCCTTAT  
839 TTTAACTTGC.

840 The dsDNA templates were then purified using an Oligo Clean and Concentrator Kit  
841 (ZymoResearch) before quantification via the Nanodrop. Single-guide RNA (sgRNA) was  
842 transcribed from this double-stranded DNA (dsDNA) template by T7 RNA polymerase using  
843 Megashortscript Kit (Thermo Fisher #AM1354). Reactions were then treated with DNase,  
844 extracted via phenol-chloroform addition and then chloroform addition, ethanol precipitated,

845 resuspended in RNase free water, quantified by Nanodrop, analyzed for quality on 15%  
846 acrylamide/TBE/UREA gels, and frozen at -20°C.

#### 847 **Pulldown assay using twin-strep-tagged AcrIIA22 and AcrIIA4**

848 The same buffer, consisting of 200 mM NaCl, 25 mM Tris (pH 7.5), was used for pulldowns  
849 and to dilute proteins. As a precursor to these assays, 130 pmol SpyCas9 and sgRNA were  
850 incubated together at room temperature for 15 minutes where indicated. SpyCas9, with or without  
851 pre-complexed sgRNA, was then incubated with 230 pmol AcrIIA4 or 320 pmol AcrIIA22 for 25  
852 minutes at room temperature. Subsequently, 50 µl of a 10% slurry of Strep-Tactin Resin (IBA  
853 Lifesciences #2-1201-002), which was pre-equilibrated in binding buffer, was added to the binding  
854 reactions, and incubated at 4°C on a nutator for 45 minutes. Thereafter, all incubations and  
855 washes were carried out at 4°C or on ice. Four total washes of this resin were performed, which  
856 included one tube transfer. Washes proceeded via centrifugation at 2000 rpm for one minute,  
857 aspiration of the supernatant with a 25-gauge needle, and resuspension of the beads in 100 µl  
858 binding buffer. Strep-tagged proteins were eluted via suspension in 40 µl of 1x BXT buffer (100  
859 mM Tris-Cl, 150 mM NaCl, 1 mM EDTA, 50 mM Biotin, pH 8.0) and incubated for 15 min at room  
860 temperature. After centrifugation, 30 µl of supernatant was removed and mixed with 4X reducing  
861 sample buffer (Thermo Fisher). Proteins were then separated by SDS PAGE on BOLT 4–12%  
862 gels in MES buffer (Invitrogen) and visualized by Coomassie staining.

#### 863 **SpyCas9 linear DNA cleavage assay**

864 All SpyCas9 cleavage reactions using linear DNA were performed in cleavage buffer<sup>61</sup>  
865 (20mM Tris HCl (pH7.5), 5% glycerol, 100mM KCl, 5mM MgCl<sub>2</sub>, 1mM DTT). In preparation for  
866 these reactions, all proteins were diluted in 30 mM NaCl / 25 mM Tris, pH 7.4 / 2.7mM KCl,  
867 whereas all DNA and sgRNA reagents were diluted in nuclease-free water. Where indicated,  
868 SpyCas9 (0.36 µM) was incubated with sgRNA (0.36 µM) for 10 minutes at room temperature.  
869 Before use, sgRNA was melted at 95°C for five minutes and then slowly cooled at 0.1 °C/s to  
870 promote proper folding. SpyCas9 (either pre-complexed with sgRNA or not, as indicated in  
871 Supplemental Figure 7) was then incubated for 10 minutes at room temperature with AcrIIA4 (2.9  
872 µM) or AcrIIA22 at each of the following concentrations: [23.2, 11.6, 5.8, and 2.9 µM]. As  
873 substrate, the plasmid pIDTsmart was linearized by restriction digest and used at a final  
874 concentration of 3.6 nM. The reaction was initiated by the addition of this DNA substrate either in  
875 isolation or in combination with sgRNA (0.36 µM) as indicated in Supplemental Figure 7.  
876 Reactions were immediately moved to a 37°C incubator and the reaction stopped after fifteen  
877 minutes via the addition of 0.2% SDS/100 mM EDTA and incubation at 75°C for five minutes.  
878 Samples were then run on a 1.5% TAE agarose gel at 120V for 40 minutes. Densitometry was  
879 used to calculate the proportion of DNA cleaved by SpyCas9; band intensities were quantified  
880 using the BioRad ImageLab software v5.0.

#### 881 ***In vivo* assay to assess impact of AcrIIA22 on plasmid topology**

882 In all experiments, cultures were first grown overnight at 37°C with shaking at 220 rpm in  
883 LB with 0.5mM IPTG and, if included, spectinomycin at 50 µg/mL, and kanamycin at 50 µg/mL.  
884 For each sample with a SpyCas9-expressing plasmid (e.g. Figure 7A), overnight cultures were  
885 grown with spectinomycin and kanamycin and diluted 1:50 into LB with 0.5mM IPTG,

886 spectinomycin (at 50  $\mu$ g/mL), and, where indicated, doxycycline (at 100 ng/mL, to induce *acrs*).  
887 Cultures were grown at 37°C with shaking at 220 rpm. If required, 0.2% (L)-arabinose was added  
888 after two hours of growth to induce *spyCas9* expression. The next morning, cultures were  
889 centrifuged at 4100g and plasmids purified using a miniprep kit (Qiagen). We measured the  
890 concentration of dsDNA in each miniprep using the Qubit-4 fluorometer and the associated  
891 dsDNA high sensitivity assay kit (Invitrogen). For each sample with a SpyCas9-expressing  
892 plasmid, 150ng of DNA was digested with the restriction enzyme HinclI (NEB) per manufacturer's  
893 recommendations, except that digests were incubated overnight before being stopped by heating  
894 at 65°C for 20 minutes. This restriction enzyme will cut once, only in the SpyCas9 plasmid, to  
895 linearize it. This allowed us to visualize the SpyCas9 plasmid as a single band, which allowed us  
896 to identify bands from *acrIIA22*-encoding undigested plasmids more easily. It also served as an  
897 internal control for plasmid DNA that is unaffected by SpyCas9 targeting or AcrIIA22 expression  
898 (Supplemental Figure 2). Following restriction digest, 30ng of sample was analyzed via gel  
899 electrophoresis using a 0.7% TAE-agarose gel run at 120V for 30 minutes.

900 In samples that lacked a SpyCas9-expressing plasmid (e.g. Figure 5A), overnight cultures  
901 were grown with kanamycin and diluted into LB. Where required, 0.5mM IPTG and doxycycline  
902 at 100 ng/mL were added to induce the gene of interest. The next morning, cultures were  
903 centrifuged at 4100g and plasmids purified using a miniprep kit (Qiagen). The concentration of  
904 dsDNA in each miniprep was measured using the Qubit-4 fluorometer and the associated dsDNA  
905 high sensitivity assay kit (Invitrogen). Then, 30ng of purified plasmid was directly analyzed by gel  
906 electrophoresis using a 0.7% TAE-agarose gel run at 120V for 30 minutes.

#### 907 ***In vitro* AcrIIA22 plasmid nicking assay**

908 Except for the divalent cation experiment, all reactions were performed using NEB buffer  
909 3.1 (100 mM NaCl, 50 mM Tris-HCl, pH 7.9, 10 mM MgCl<sub>2</sub>, 100  $\mu$ g/mL BSA). To determine cation  
910 preference, the same reaction buffer was re-created, but MgCl<sub>2</sub> was omitted. All proteins were  
911 diluted in 130 mM NaCl, 25 mM Tris, pH 7.4, 2.7 mM KCl. DNA was diluted in nuclease-free water.  
912 In the cation preference experiment, 60  $\mu$ M His6-AcrIIA22 and 6 nM of purified pIDTsmart plasmid  
913 DNA were used. All other reactions were set up with AcrIIA22 constructs and concentrations  
914 indicated in figure panels and captions. In the cation preference experiment (Supplemental Figure  
915 11A), reactions were started by adding 10 mM of the indicated cation. All other reactions were  
916 initiated via the addition of 2 nM pIDTsmart plasmid DNA. In these cases, reactions were  
917 immediately transferred to a 37°C incubator. At 0.5, 1, 2, 4, 6, or 20-hour timepoints, a subset of  
918 the reaction was removed and run on a 1.5% TAE agarose gel at 120V for 30 minutes. For the  
919 fractionation experiment depicted in Supplemental Figure 10B, 5ul of each concentrated fraction  
920 was used in a 15ul reaction volume and the reaction was incubated for 24 hours at 37°C. For the  
921 cation preference experiment, only the 2-hour timepoint was considered and the reaction was  
922 stopped via the addition of NEB loading buffer and 100 mM EDTA. In this case, DNA was  
923 visualized on a 1% TBE gel run for 60 minutes at 110V. Densitometry was used to calculate the  
924 proportion of DNA in each topological form via band intensities quantified using the BioRad  
925 ImageLab software v5.0.

#### 926 **SpyCas9 cleavage kinetics assay**

927 All cleavage reactions were performed in the cleavage buffer<sup>61</sup> containing 20mM Tris HCl  
928 (pH7.5), 5% glycerol, 100mM KCl, 5mM MgCl<sub>2</sub>, 1mM DTT. In preparation for these reactions, all  
929 proteins were diluted in 30 mM NaCl / 25 mM Tris, pH 7.4 / 2.7mM KCl, whereas all DNA and  
930 sgRNA reagents were diluted in nuclease-free water.

931 Purified pIDTsmart plasmid was pre-treated with either AcrlIA22, the nickase Nb.BssSI  
932 (NEB), or no enzyme. For the AcrlIA22 pre-treatment, 3.1 µg of plasmid was incubated with 230  
933 µM AcrlIA22 and the plasmid nicked as described previously. Plasmid nicking with Nb.BssSI was  
934 carried out via manufacturer's recommendations (NEB). Both reactions were incubated at 37 °C  
935 for 2 hours. To isolate the nicked plasmid, samples were then run on a 1.5% agarose gel for 2  
936 hours and the open-circle form of the plasmid was excised and purified using the Zymo Research  
937 Gel DNA Recovery Kit. Untreated plasmid was also purified via gel extraction. Plasmid yield was  
938 quantified using a Nanodrop.

939 To determine SpyCas9's substrate preference, we incubated each pre-treated plasmid  
940 substrate with SpyCas9 and assayed for the appearance of a linearized plasmid as indication of  
941 SpyCas9 digestion. In all cases, SpyCas9 was used at a final concentration of 0.32 µM. All  
942 reaction components except dsDNA were added on ice, following which SpyCas9 was complexed  
943 with equimolar levels of its sgRNA for ten minutes at room temperature. Before addition to the  
944 reaction, sgRNA was melted at 95°C for five minutes and then slowly cooled at 0.1 °C/s to promote  
945 proper folding. To begin the reaction, DNA substrate was added to the reaction mix at a final  
946 concentration of 2 nM and the samples moved immediately to 37 °C. At each timepoint, a subset  
947 of the reaction was removed, and digestion stopped with 0.2% SDS/100 mM EDTA and by  
948 incubating at 75°C for 5 minutes. Samples were run on a 1.5% TAE gel at 120V for 40 minutes  
949 and densitometry was used to calculate the proportion of DNA in each topological form via band  
950 intensities quantified with the BioRad ImageLab software v5.0.

951 **Acknowledgements**

952 We thank Kaylee Dillard, Ilya Finkelstein, Yu-Ying Phoebe Hsieh, Tera Levin, and Janet  
953 Young for comments on the manuscript. Use of the Advanced Photon Source, an Office of  
954 Science User Facility operated for the U.S. Department of Energy (DOE) Office of Science by  
955 Argonne National Laboratory, was supported by the U.S. DOE under Contract No. DE-AC02-  
956 06CH11357. This work was supported by a Helen Hay Whitney Foundation postdoctoral  
957 fellowship awarded to KJF, a Seattle University summer faculty fellowship to BKK, NIH grant  
958 R01GM105691 and discretionary funding from the Fred Hutchinson Cancer Research Center to  
959 BLS, and grants from the G. Harold and Leila Y. Mathers Foundation and the Howard Hughes  
960 Medical Institute to HSM. The funders played no role in study design, data collection and  
961 interpretation, or the decision to publish this study. HSM is an Investigator of the Howard Hughes  
962 Medical Institute.

963 **Competing Interests**

964 All authors declare no significant competing financial, professional, or personal interests that  
965 might have influenced the performance or presentation of the work described in this manuscript.

966 **Main Figure Captions**

967 **Figure 1. Functional selection reveals a metagenomic contig encoding a novel SpyCas9**  
968 **inhibitor. (A)** A plasmid protection assay was used to reveal SpyCas9 inhibition. In this assay,  
969 plasmids without SpyCas9 inhibitors are cleaved by Cas9 and do not give rise to Kan<sup>R</sup> colonies,  
970 whereas those encoding inhibitors withstand SpyCas9 attack and yield Kan<sup>R</sup> colonies. **(B)** The  
971 contig F01A\_4 protects a plasmid from SpyCas9 attack but an early stop codon in *orf\_1* ( $\Delta 1$ )  
972 eliminates this phenotype. Stop codons in *orf\_2* or *orf\_3* ( $\Delta 2$  and  $\Delta 3$ ) have no effect. Thus, we  
973 conclude that *orf\_1* is necessary for inhibition of SpyCas9. Asterisks depict statistically significant  
974 differences in plasmid retention between the indicated genotype and an empty vector control in  
975 SpyCas9-inducing conditions (Student's t-test,  $p < 0.002$ ,  $n=3$ ); ns indicates no significance. All p-  
976 values were corrected for multiple hypotheses using Bonferroni's method. **(C)** Expression of *orf\_1*  
977 (which we name *acrlIA22*) is sufficient for SpyCas9 antagonism, protecting a plasmid as  
978 effectively as *acrlIA4*. Asterisks are as in panel B but relate to the GFP negative control rather  
979 than to an empty vector. The individual numerical values that underlie the summary data in this  
980 figure may be found as supporting information file SI\_Data.

981 **Figure 2. *AcrlIA22* homologs are found in hypervariable regions of prophage and bacterial**  
982 **genomes in the unnamed clostridial genus, CAG-217. (A)** We show a schematic  
983 representation of an *acrlIA22* homolog embedded in a prophage genome, which is integrated into  
984 a bacterial genome (contig #57). We can delineate precise boundaries of the inserted prophage  
985 based on comparison to a near-identical bacterial contig (contig #55). Prophage genes are  
986 colored by functional category, according to the legend at the top. Bacterial genes are colored  
987 light gray. **(B)** Homologs of *acrlIA22* are depicted in diverse genomic islands, including Contig #1,  
988 whose sequence includes a portion identical to F01A\_4, the original metagenomic contig we  
989 recovered. All *acrlIA22* homologs in these loci are closely related but their adjacent genes are  
990 different, unrelated gene families (depicted by different colors). Genomic regions flanking these  
991 hypervariable islands, including genes immediately adjacent to these islands (*purF* and *radC*, in  
992 bold outlines), are nearly identical to one another ( $\geq 98\%$  nucleotide identity). Contigs are  
993 numbered to indicate their descriptions in Supplemental Table 3, which contains their metadata,  
994 taxonomy, and sequence retrieval information. All sequences and annotations may also be found  
995 in Supplemental Datasets 1 and 2. **(C)** We propose an evolutionary model for the origin of the  
996 *acrlIA22*-encoding hypervariable genomic islands depicted in panel B. We propose that *acrlIA22*  
997 moved via prophage integration into a bacterial genomic locus but remained following an  
998 incomplete prophage excision event. Its neighboring genes subsequently diversified via horizontal  
999 exchange with additional phage genomes without these phage genomes inserting into the locus.  
1000 Supplemental Figure 4 depicts a more detailed version of the genomic data underlying this model.

1001 **Figure 3. Several *AcrlIA22* homologs in the CAG-217 clostridial genus can inhibit SpyCas9.**  
1002 **(A)** A phylogeny of all unique *AcrlIA22* homologs identified from metagenomic and NCBI  
1003 databases. Phylogenetic classifications were assigned corresponding to the GTDB naming  
1004 convention (Methods). Prophage sequences are shaded brown and homologs from hypervariable  
1005 bacterial genomic islands are shaded yellow. Sequences obtained from NCBI are labeled with  
1006 protein accession numbers. In other cases, *AcrlIA22* homologs are numbered to match their  
1007 contig-of-origin (Supplemental Table 3). In some cases, more than one *AcrlIA22* homolog is found  
1008 on the same contig ('gi' or 'p' indicates its presence in a hypervariable genomic island or prophage  
1009 genome, respectively). Circles at nodes indicate bootstrap support  $\geq 0.75$ . Dashed boxes  
1010 separate sequences identified from CAG-217 versus *Eubacterium\_R* bacterial genera. Filled

1011 green circles indicate homologs that were tested for their ability to inhibit SpyCas9 in the plasmid  
1012 protection assay in panel B. These homologs have been named with 'a', 'b', or 'c' suffixes to  
1013 distinguish them from the original AcrlIA22 metagenomic hit; their amino acid identity to the  
1014 original hit is shown in parentheses. **(B)** Several homologs of AcrlIA22 in CAG-217 genomes  
1015 inhibit SpyCas9. Asterisks depict statistically significant differences in plasmid retention under  
1016 SpyCas9-inducing conditions between the indicated sample and a null mutant with an early stop  
1017 codon in *acrlIA22*, as indicated in the legend at right (ns indicates no significance;  $p > 0.05$ ). All  
1018 p-values were corrected for multiple hypotheses using Bonferroni's method (Student's t-test,  $n=3$ ).  
1019 **(C)** AcrlIA22 inhibits divergent Cas9 proteins from *Streptococcus pyogenes* (SpyCas9) or  
1020 *Neisseria meningitidis* (NmCas9) but not Cas12 proteins from *Lachnospiraceae bacterium*  
1021 (LbCas12) or *Francisella novicida* (FnCas12). As in panel B, green bars indicate samples with  
1022 expression of the indicated Cas nuclease while unexpressed controls are depicted with gray lines.  
1023 For Cas-expressing samples, significance was determined via a Student's t-test ( $n=3$ ) and  
1024 denoted as follows: '\*'  $p \leq 0.05$  ; '\*\*'  $p \leq 0.001$  ; 'ns' no significance. Due to slight differences in the  
1025 plasmid protection assay in panel C compared to panel B, A22 was re-tested against SpyCas9 to  
1026 confirm activity (Methods). The individual numerical values that underlie the summary data in this  
1027 figure may be found as supporting information file SI\_Data.

1028 **Figure 4. AcrlIA22 is an oligomeric PC4-like protein.** **(A)** AcrlIA22's crystal structure reveals a  
1029 homodimer of two four-stranded  $\beta$ -sheets. **(B)** AcrlIA22 elutes as an oligomer that is  
1030 approximately four times the predicted molecular mass of its monomer, which is 7 kDa. The gray,  
1031 dashed trace depicts protein standards of the indicated molecular weight, in kDa. The orange  
1032 trace depicts the elution profile of a two-amino acid C-terminal AcrlIA22 truncation mutant that is  
1033 predicted to disrupt oligomerization. **(C)** Ribbon diagram of a proposed AcrlIA22 tetramer which  
1034 requires binding between anti-parallel  $\beta$ -strands at the C-termini of AcrlIA22 monomers to form  
1035 extended, concave  $\beta$ -sheets. The putative oligomerization interface is indicated by the regions  
1036 highlighted in yellow and the dashed box, and is detailed further in panel F. Each monomer in the  
1037 proposed tetramer is labeled with lower-case Roman numerals (i-iv). **(D)**  $\beta$ -sheet topology and  
1038 orientation in AcrlIA22 (blue) resemble that of PC4-like family proteins (in gray, PDB:4BG7 from  
1039 phage T5). **(E)** A monomer of AcrlIA22 (in blue, PDB:7JTA) is structurally similar to a PC4-like  
1040 single-stranded DNA binding protein, which is proposed to promote recombination in phage T5  
1041 (in gray, PDB:4BG7, Z-score=6.2, matched residues 15%), except for a missing C-terminal alpha  
1042 helix. **(F)** A putative oligomerization interface between the C-termini of two AcrlIA22 monomers  
1043 from panel (C) is shown in more detail. Dashed lines indicate potential hydrogen bonds between  
1044 the polypeptide backbones. This interface occurs twice in the putative tetramer, between red-  
1045 hued and blue-hued monomers in panel C.

1046 **Figure 5. AcrlIA22 nicks supercoiled plasmids *in vivo* and *in vitro*.** **(A)** Gel electrophoresis of  
1047 plasmids purified from overnight *E. coli* cultures expressing either *acrlIA22*, or a null mutant with  
1048 an early stop codon, or neither. Compared to the null mutant, more plasmid runs in a slowly  
1049 migrating, open-circle conformation (OC) rather than supercoiled plasmid (SC) with the wild-type  
1050 *acrlIA22* allele, suggesting that *acrlIA22* may impact plasmid topology. %SC indicates the  
1051 percentage of DNA in the supercoiled form for each sample. **(B)** N-terminally His6-tagged  
1052 AcrlIA22 nicks supercoiled plasmids *in vitro*. **(C)** C-terminally twin-strep-tagged AcrlIA22 nicks  
1053 supercoiled plasmids *in vitro* with higher specific activity than shown in panel B (compare protein  
1054 concentrations). Original, uncropped versions of images depicted in figure may be found in the  
1055 supporting information file, SI\_raw\_images.

1056 **Figure 6. Impaired nicking activity of AcrIIA22 variants *in vitro* correlates with lower**  
1057 **SpyCas9 inhibition *in vivo*.** (A) Alanine mutagenesis of acidic amino acid residues (glutamic  
1058 acid or aspartic acid) in AcrIIA22 reveals that D14 is important for plasmid protection against  
1059 SpyCas9. Asterisks depict statistically significant differences in plasmid retention under SpyCas9-  
1060 inducing and non-inducing conditions, per the legend at right. The D14A mutant is significantly  
1061 impaired, the E4A mutant is slightly impaired, whereas all other mutants are not impaired for  
1062 plasmid protection against SpyCas9 compared to an uninduced control. All p-values were  
1063 corrected for multiple hypotheses using Bonferroni's method (Student's t-test, n=3). (B) AcrIIA22  
1064 (black), AcrIIA22a (dark gray), and a D14A mutant (light gray) all elute with similar oligomer  
1065 profiles via SEC. The dashed trace depicts protein standards of the indicated molecular weight,  
1066 in kDa. (C) AcrIIA22a and the D14A mutant are impaired for nicking relative to AcrIIA22. All  
1067 experiments were performed in triplicate, with standard deviations indicated by dashed lines (in  
1068 most cases, the data points obscure these error bars). Asterisks denote cases where AcrIIA22 is  
1069 significantly different than both AcrIIA22a and the D14A mutant after correcting for multiple  
1070 hypotheses (Student's t-test, n=3, Bonferroni correction). A single asterisk (\*) means that adjusted  
1071 p-values for both comparisons are below 0.05. A double asterisk (\*\*) means that adjusted p-  
1072 values are both below 0.005. Supplemental Figures 10G and 10H show representative gels for  
1073 these nicking experiments. The individual numerical values that underlie the summary data in this  
1074 figure may be found as supporting information file SI\_Data.

1075 **Figure 7. Nicking by AcrIIA22 protects plasmids from SpyCas9 *in vivo* and *in vitro*.** (A) Gel  
1076 electrophoresis of plasmids purified from overnight *E. coli* cultures expressing either wildtype  
1077 *acrIIA22* or a mutant with an early stop codon ('null'). In these cultures, SpyCas9 was expressed  
1078 from a second plasmid, which was linearized via a unique restriction site before electrophoresis.  
1079 The *acrIIA22*-encoding plasmids are indicated with the 'pTarget' label. OC, open-circle; SC,  
1080 supercoiled. The '%pTarget' figure indicates the fraction of total DNA attributable to pTarget,  
1081 quantified by densitometry analysis. In cases with complete pTarget elimination, all DNA comes  
1082 from the SpyCas9 expression plasmid, and thus these bands are more pronounced. However, in  
1083 the presence of wildtype *acrIIA22*, pTarget is protected from SpyCas9-mediated cleavage and  
1084 makes up 43% of total plasmid DNA. (B) We present a schematic of the experimental design for  
1085 the data depicted in panel C. The experiment tests whether SpyCas9 preferentially cleaves a  
1086 supercoiled or open-circle plasmid target *in vitro*. Though both plasmid substrates will be  
1087 linearized following SpyCas9 cleavage, linear DNA will accumulate more readily with a preferred  
1088 substrate. (C) Plasmid purifications from overnight cultures were either left unmodified or pre-  
1089 treated with one of two nickase enzymes, AcrIIA22 or Nb.BssSI, following which each substrate  
1090 was digested with SpyCas9 *in vitro*. The percentage of DNA in the linear form is quantified below  
1091 the gel, which indicates complete SpyCas9 cleavage. Linear, open-circle (OC), and supercoiled  
1092 (SC) plasmid forms are indicated along with the left of the gel, and reaction components below  
1093 the gel. SpyCas9 cuts DNA strands sequentially; incomplete digestions with supercoiled  
1094 substrates produce open-circle plasmids if only one strand has been cleaved (e.g. lane 5). Pre-  
1095 nicked plasmids, by either AcrIIA22 or Nb.BssSI, are less susceptible to linearization via SpyCas9  
1096 cleavage. (D) Endpoint measurements indicate that SpyCas9 more efficiently linearizes  
1097 supercoiled plasmids than substrates nicked with either AcrIIA22 or Nb.BssSI (Student's t-test,  
1098 n=3). (E) A time course experiment demonstrates that SpyCas9 more efficiently linearizes  
1099 supercoiled plasmids than AcrIIA22-treated substrates. An asterisk (\*) denotes significant  
1100 differences between AcrIIA22-treated and untreated substrates (Student's t-test, p < 0.05, n=3).

1101 The individual numerical values and original images for the data presented in this figure may be  
1102 found in the supporting information files SI\_Data and SI\_raw\_images, respectively.

1103 **Supplemental Figure Captions**

1104 **Supplemental Figure 1. *Orf\_1 (acrIIA22)* confers mild toxicity in *E. coli*.** Growth rates with  
1105 *orf\_1* induction (green) are 7% lower than those without *orf\_1* induction (orange). The cfu data  
1106 shown in Figure 1C were generated from the same experiment depicted here (samples were  
1107 removed after six hours of growth to determine these cfu counts). Thus, these data demonstrate  
1108 that anti-SpyCas9 activity occurs under conditions with mild *orf\_1* toxicity. Growth curves are  
1109 shown for samples without SpyCas9 induction to ensure that *orf\_1* toxicity is not mitigated due to  
1110 elimination of its plasmid. Points indicate averages from three replicates. Standard deviations at  
1111 each timepoint are so small that the error bars do not exceed the bounds of the data point. The  
1112 individual numerical values that underlie the summary data in this figure may be found as  
1113 supporting information file SI\_Data.

1114 **Supplemental Figure 2. *Orf\_1 (acrIIA22)* does not impact SpyCas9 expression.** (A) A  
1115 schematic description of the experimental design shown in panel (B) is presented. If ORF\_1  
1116 prevented transcription from pCas9 or altered its copy number, we would expect expression of  
1117 the *orf\_1* gene to deplete the level of green fluorescence observed from a construct that replaces  
1118 the *spycas9* gene with *gfp*. (B) Fluorescence measurements for the experiment depicted in panel  
1119 A show that ORF\_1 does not impact GFP expression throughout an *E. coli* growth curve. Points  
1120 indicate averages from three replicates, error bars indicate standard deviation. A western blot  
1121 shows no depletion of SpyCas9 expression as a function of ORF\_1 or GFP expression in growing  
1122 *E. coli* cultures at three hours (C) or six hours (D). As an internal control, GAPDH expression was  
1123 also detected. The individual numerical values and original images for the data presented in this  
1124 figure may be found in the supporting information files SI\_Data and SI\_raw\_images, respectively.

1125 **Supplemental Figure 3. *AcrIIA22* only modestly protects Mu phages against SpyCas9.** Mu  
1126 phage fitness was measured by plaquing on *E. coli* in the presence of *gfp*, *acrIIA22*, or *acrIIA4*  
1127 via serial ten-fold dilutions. Bacterial clearing (black) occurs when phage Mu overcomes SpyCas9  
1128 immunity and lyses *E. coli*. In (A) and in (B), SpyCas9 with a Mu-targeting crRNA confers  
1129 substantial protection against phage Mu relative to a non-targeting (n.t.) control, in both conditions  
1130 tested. These conditions are depicted at left, with the only difference being whether SpyCas9 was  
1131 only expressed in liquid growth prior to phage infection (panel A) or expressed both in liquid media  
1132 and in solid media throughout infection (panel B). When expressed from a second plasmid, the  
1133 positive control *acrIIA4* significantly enhances Mu fitness by inhibiting SpyCas9 in all conditions  
1134 *in trans*. Though *acrIIA22* confers protection against SpyCas9 compared to *gfp* (negative control),  
1135 this effect is milder than with *acrIIA4* and dependent on SpyCas9 expression.

1136 **Supplemental Figure 4. *AcrIIA22* homologs are found in hypervariable regions of prophage**  
1137 **and bacterial genomes in the CAG-217clostridial genus.** (A) Homologs of *acrIIA22* are  
1138 depicted in three related prophage genomes, integrated at three different genomic loci, revealed  
1139 by a comparison of prophage-bearing contigs (#57, #56, #37) relative to unintegrated contigs  
1140 (#55, #58, #17 respectively), which are otherwise nearly identical. Prophage genes are colored  
1141 by functional category, according to the legend at the left of panel A. Genes immediately adjacent  
1142 to *acrIIA22* (solid boxes) vary across phages, despite strong relatedness across much of the  
1143 prophage genomes. Bacterial genes are colored gray, except for contig #17, which is also  
1144 depicted in panel B, below. (B) Homologs of *acrIIA22* are depicted in diverse genomic islands,

1145 including Contig #1, whose sequence includes a portion that is identical to the original  
1146 metagenomic contig we recovered (F01A\_4). All *acrIIA22* homologs in these loci are closely  
1147 related but differ in their adjacent genes, which often have homologs in the prophages depicted  
1148 in panel A (dashed boxes). Bacterial genomic regions flanking these hypervariable islands are  
1149 nearly identical to one another and to prophage integration locus #3, as shown by homology to  
1150 contig #17 from panel A. Contigs are numbered to indicate their descriptions in Supplemental  
1151 Table 3, which contains their metadata, taxonomy, and sequence retrieval information. All  
1152 sequences and annotations can also be found in Supplemental Datasets 1 and 2. **(C)** We tabulate  
1153 the prevalence of various protein families (clustered at 65% amino acid identity) in a set of 54  
1154 unique genomic islands. Each of these islands is flanked by the conserved genes *purF* and *radC*  
1155 but contains a different arrangement of encoded genes. Domain-level annotations are indicated  
1156 below each protein family (unk; unknown function). Gene symbols above each protein family are  
1157 colored and lettered to indicate their counterparts or homologs in panels A and B. The phage  
1158 capsid icon indicates sequences with homologs in prophage genomes. **(D)** An evolutionary model  
1159 for the origin of the *acrIIA22*-encoding hypervariable genomic islands depicted in panel B is  
1160 shown. This panel is reprinted from Figure 2C, for continuity. We propose that *acrIIA22* moved  
1161 via a phage insertion into a bacterial genomic locus, remained following an incomplete prophage  
1162 excision event, and its neighboring genes subsequently diversified via horizontal exchange with  
1163 additional phage genomes. The individual numerical values that underlie the summary data in  
1164 this figure may be found as supporting information file SI\_Data.

1165 **Supplemental Figure 5. Genomic proximity of *acrIIA22* homologs to other *acr* genes.** An  
1166 *acrIIA22*-encoding prophage like the one depicted in Figure 2A and those in Supplemental Figure  
1167 4A is shown. This prophage encodes for a homolog of the previously described SpyCas9 inhibitor  
1168 *acrIIA17* within one kilobase of an *acrIIA22* homolog. Sequence relatedness between the depicted  
1169 *acrIIA17* gene and the originally discovered *acrIIA17* is shown<sup>22</sup>. Because phages often encode  
1170 multiple *acrs* in the same locus, the co-localization of *acrIIA17* with *acrIIA22* is consistent with the  
1171 latter gene functioning natively to inhibit CRISPR-Cas activity. Prophage genes are colored by  
1172 functional category, per the legend and as in Supplemental Figure 4A. Contigs are numbered to  
1173 indicate their descriptions in Supplemental Table 3, which contains their metadata, taxonomy,  
1174 and sequence retrieval information. All sequences and annotations can also be found in  
1175 Supplemental Datasets 1 and 2.

1176 **Supplemental Figure 6. AcrIIA22 does not strongly bind SpyCas9.** SpyCas9 and sgRNA were  
1177 pre-incubated before mixing with a twin-strep (TS) tagged AcrIIA22 or AcrIIA4. SpyCas9 without  
1178 sgRNA was also used. Strep-Tactin pulldowns on AcrIIA4 also pulled down SpyCas9 pre-  
1179 incubated with sgRNA, as previously reported<sup>12</sup>. Similar pulldowns with AcrIIA22 indicate little to  
1180 no interaction with SpyCas9, regardless of whether sgRNA was used. These images depict total  
1181 protein content visualized by Coomassie stain. Reaction components are indicated below the gel  
1182 image. Asterisks (\*) and dagger (†) symbols indicate AcrIIA4 and AcrIIA22 protein bands that run  
1183 at slightly different positions than expected due to gel distortion. Original, uncropped versions of  
1184 images depicted in figure may be found in the supporting information file, SI\_raw\_images.

1185 **Supplemental Figure 7. AcrIIA22 does not protect linear DNA from SpyCas9 cleavage. (A)**  
1186 A schematic cartoon depicts the experiment in panel (B). SpyCas9 was pre-incubated with sgRNA  
1187 targeting linear DNA. Then, Acr candidates were added. Subsequently, cleavage reactions were  
1188 performed, and the DNA products visualized by gel electrophoresis. **(B)** We show the products of  
1189 the reactions described in panel A for the inhibitors AcrIIA22 and AcrIIA4. SpyCas9 activity is

1190 greatly inhibited by AcrIIA4 but unaffected by AcrIIA22, as indicated by the proportion of cleaved  
1191 DNA product. Reaction components are depicted atop the gel image, with molar equivalents  
1192 relative to SpyCas9 indicated. The percent of DNA substrate cleaved by SpyCas9 is quantified  
1193 below each lane. **(C)** We perform a similar experiment as in panel A, except candidate Acrs were  
1194 incubated with SpyCas9 before sgRNA addition. Reactions were begun via the simultaneous  
1195 addition of sgRNA and linear dsDNA instead of just dsDNA. **(D)** The products of the reactions  
1196 described in panel C for AcrIIA22 and AcrIIA4 inhibitors are shown. SpyCas9 activity is inhibited  
1197 by AcrIIA4 but unaffected by AcrIIA22, as indicated by the proportion of cleaved DNA product.  
1198 The data depicted in this figure are not directly comparable to those in figure 7, due to  
1199 methodological differences and because the preparations of SpyCas9 used in each experiment  
1200 exhibited different activities. Original, uncropped versions of images depicted in figure may be  
1201 found in the supporting information file, SI\_raw\_images.

1202 **Supplemental Figure 8. AcrIIA22 resembles a PC4-like protein.** **(A)** We present a ribbon  
1203 diagram of a proposed AcrIIA22 tetramer, which requires binding between anti-parallel  $\beta$ -strands  
1204 at the C-termini of AcrIIA22 monomers to form extended, concave  $\beta$ -sheets. This putative  
1205 oligomerization interface is indicated by the regions highlighted in yellow. Each monomer in the  
1206 proposed tetramer is labeled with lower-case Roman numerals (i-iv). **(B)** Space filling model of  
1207 the tetrameric AcrIIA22 structure from panel A, with relative charge depicted, highlighting a groove  
1208 (dashed line with arrowhead) that may accommodate nucleic acids (based on analogy to other  
1209 PC4-like proteins). **(C)** AcrIIA22 monomers (i) and (ii) from the tetramer in panel A likely interact  
1210 via a series of hydrophobic interactions, as indicated by the predominantly non-polar sidechains  
1211 colored in yellow. The boxed region highlights residue D14, which is important for nicking activity  
1212 and plasmid protection against SpyCas9, and is enlarged in panel F. **(D)** In conventional PC4-like  
1213 family proteins, such as the putative single-stranded DNA binding protein from phage T5 depicted  
1214 in gray (PDB:4BG7), the same topology of outward facing, concave  $\beta$ -sheets are instead  
1215 stabilized via interactions between opposing  $\alpha$ -helices (depicted in opaque light blue). **(E)** An  
1216 overlay of  $\beta$ -sheets from AcrIIA22 (blue, PDB:7JTA) and the phage T5 PC4-like protein (gray,  
1217 PDB:4BG7) illustrates their similar topologies. **(F)** Two D14 residues in loop regions of AcrIIA22  
1218 monomers (i) and (ii) are in close proximity. These residues are important for nicking activity and  
1219 may bind divalent cations in cells under physiological pH. **(G)** A close view of a putative salt bridge  
1220 between R30 of monomers (i) / (ii) and the peptide backbone of the C-terminus of monomers (iv)  
1221 / (iii), respectively. AcrIIA22 monomers are colored as described in panel A.

1222 **Supplemental Figure 9. A 2-aa truncation mutant of AcrIIA22 is impaired for SpyCas9**  
1223 **inhibition and nicking activity.** **(A)** An *in vivo* plasmid protection assay. Asterisks depict  
1224 statistically significant differences in plasmid retention under SpyCas9-inducing conditions with  
1225 either wild-type AcrIIA22, a null mutant with an early stop codon, a 2-aa truncation, or a negative  
1226 control *gfp* gene (adj.  $p < 0.005$ , Student's t-test,  $n=3$ ). The truncation mutant retains mild but  
1227 severely impaired activity, as it protects a plasmid from SpyCas9 more effectively than a null  
1228 mutant ( $p = 0.012$ ) or GFP control ( $p = 0.015$ ). All p-values were corrected for multiple hypotheses  
1229 using Bonferroni's method. **(B)** The 2-aa truncation mutant is impaired for nicking *in vitro*, relative  
1230 to wild-type AcrIIA22. In both cases, 25  $\mu$ M of protein was used following NiNTA-based purification  
1231 of an N-terminal, His6-tagged construct. An asterisk (\*) denotes significant differences between  
1232 AcrIIA22-treated and untreated substrates (Student's t-test,  $p < 0.05$ ,  $n=3$ ). Standard deviations  
1233 are indicated by dashed lines (in most cases, the data points obscure these error bars). The  
1234 individual numerical values that underlie the summary data in this figure may be found as  
1235 supporting information file SI\_Data.

1236 **Supplemental Figure 10. AcrIIA22 nicks supercoiled plasmids.** (A) A Coomassie stain of an  
1237 N-terminally His6-tagged AcrIIA22 construct shows no co-purifying proteins. (B) The nicking  
1238 activity for this protein preparation (bottom) correlates with the intensity of the Coomassie-stained  
1239 protein band across purification fractions (top). In each lane, supercoiled (SC) plasmid DNA  
1240 represents the un-nicked fraction whereas open circle (OC) and linear DNA have been nicked at  
1241 least once. (C) This panel is a quantification of the experiment depicted in panel B across all 13  
1242 fractions collected. (D) His6-AcrIIA22 nicks supercoiled plasmids in a time and concentration  
1243 dependent manner. A decrease in the proportion of supercoiled plasmid DNA indicates nicking  
1244 activity, as depicted in Figure 5B. (E) A silver stain of a C-terminally twin-strep-tagged AcrIIA22  
1245 construct shows no co-purifying proteins. Equal volumes of each protein fraction were loaded in  
1246 each lane, for all samples. Fraction 4 was concentrated and used for all *in vitro* experiments. (F)  
1247 A C-terminal, but not N-terminal twin-strep tag is compatible with AcrIIA22's ability to protect a  
1248 target plasmid from SpyCas9 elimination *in vivo*. Statistically significant differences in plasmid  
1249 retention between SpyCas9-inducing and non-inducing conditions were determined via a  
1250 Student's t-test (n=3); \*\* indicates p≤0.001. All p-values were adjusted for multiple hypotheses  
1251 using the Bonferroni correction. (G) The D14A mutation in AcrIIA22 impairs nicking activity. Over  
1252 time, the wild-type AcrIIA22-twin-strep construct consistently converts a higher fraction of plasmid  
1253 DNA from its supercoiled (SC) form to an open-circle (OC) conformation than a D14A mutant.  
1254 Control plasmids include a miniprepped sample and sample pre-treated with the commercial  
1255 nickase, Nb.BssSI. Reaction times are indicated to the right of each image. (H) AcrIIA22a (Figure  
1256 3B) is impaired for nicking activity relative to AcrIIA22. As in panel G, both constructs were purified  
1257 via C-terminal twin-strep tags. The individual numerical values and original images for the data  
1258 presented in this figure may be found in the supporting information files SI\_Data and  
1259 SI\_raw\_images, respectively.

1260 **Supplemental Figure 11. Divalent cations influence AcrIIA22's nicking activity.** (A) We  
1261 present the impact of different divalent cations on AcrIIA22's nicking activity, which is highest  
1262 with Mg<sup>2+</sup>, Mn<sup>2+</sup>, and Co<sup>2+</sup>. OC, open-circle plasmid form. SC, supercoiled plasmid. (B) The  
1263 open-circle plasmid product persists through phenol-chloroform extraction following AcrIIA22  
1264 treatment, indicating that it directly results from AcrIIA22's nicking activity.

## References

1265 1 Barrangou, R. *et al.* CRISPR provides acquired resistance against viruses in  
1266 prokaryotes. *Science* **315**, 1709-1712, doi:10.1126/science.1138140 (2007).

1267 2 Marraffini, L. A. & Sontheimer, E. J. CRISPR interference limits horizontal gene transfer  
1268 in staphylococci by targeting DNA. *Science* **322**, 1843-1845,  
1269 doi:10.1126/science.1165771 (2008).

1270 3 Deveau, H. *et al.* Phage response to CRISPR-encoded resistance in *Streptococcus*  
1271 *thermophilus*. *J Bacteriol* **190**, 1390-1400, doi:10.1128/JB.01412-07 (2008).

1272 4 Mendoza, S. D. *et al.* A bacteriophage nucleus-like compartment shields DNA from  
1273 CRISPR nucleases. *Nature* **577**, 244-248, doi:10.1038/s41586-019-1786-y (2020).

1274 5 Malone, L. M. *et al.* A jumbo phage that forms a nucleus-like structure evades CRISPR-  
1275 Cas DNA targeting but is vulnerable to type III RNA-based immunity. *Nat Microbiol* **5**, 48-  
1276 55, doi:10.1038/s41564-019-0612-5 (2020).

1277 6 Bryson, A. L. *et al.* Covalent Modification of Bacteriophage T4 DNA Inhibits CRISPR-  
1278 Cas9. *mBio* **6**, e00648, doi:10.1128/mBio.00648-15 (2015).

1279 7 Stanley, S. Y. & Maxwell, K. L. Phage-Encoded Anti-CRISPR Defenses. *Annu Rev  
1280 Genet* **52**, 445-464, doi:10.1146/annurev-genet-120417-031321 (2018).

1281 8 Trasanidou, D. *et al.* Keeping crispr in check: diverse mechanisms of phage-encoded  
1282 anti-crisprs. *FEMS Microbiol Lett*, doi:10.1093/femsle/fnz098 (2019).

1283 9 Davidson, A. R. *et al.* Anti-CRISPRs: Protein Inhibitors of CRISPR-Cas Systems. *Annu  
1284 Rev Biochem* **89**, 309-332, doi:10.1146/annurev-biochem-011420-111224 (2020).

1285 10 Wiegand, T., Karambelkar, S., Bondy-Denomy, J. & Wiedenheft, B. Structures and  
1286 Strategies of Anti-CRISPR-Mediated Immune Suppression. *Annu Rev Microbiol* **74**, 21-  
1287 37, doi:10.1146/annurev-micro-020518-120107 (2020).

1288 11 Hatfull, G. F. Dark Matter of the Biosphere: the Amazing World of Bacteriophage  
1289 Diversity. *J Virol* **89**, 8107-8110, doi:10.1128/JVI.01340-15 (2015).

1290 12 Forsberg, K. J. *et al.* Functional metagenomics-guided discovery of potent Cas9  
1291 inhibitors in the human microbiome. *eLife* **8**, e46540, doi:10.7554/eLife.46540 (2019).

1292 13 Szczelkun, M. D. *et al.* Direct observation of R-loop formation by single RNA-guided  
1293 Cas9 and Cascade effector complexes. *Proc Natl Acad Sci U S A* **111**, 9798-9803,  
1294 doi:10.1073/pnas.1402597111 (2014).

1295 14 Farasat, I. & Salis, H. M. A Biophysical Model of CRISPR/Cas9 Activity for Rational  
1296 Design of Genome Editing and Gene Regulation. *PLoS Comput Biol* **12**, e1004724,  
1297 doi:10.1371/journal.pcbi.1004724 (2016).

1298 15 Ivanov, I. E. *et al.* Cas9 interrogates DNA in discrete steps modulated by mismatches  
1299 and supercoiling. *Proc Natl Acad Sci U S A* **117**, 5853-5860,  
1300 doi:10.1073/pnas.1913445117 (2020).

1301 16 Tsui, T. K. M., Hand, T. H., Duboy, E. C. & Li, H. The Impact of DNA Topology and  
1302 Guide Length on Target Selection by a Cytosine-Specific Cas9. *ACS Synth Biol* **6**, 1103-  
1303 1113, doi:10.1021/acssynbio.7b00050 (2017).

1304 17 Paez-Espino, D. *et al.* IMG/VR v.2.0: an integrated data management and analysis  
1305 system for cultivated and environmental viral genomes. *Nucleic acids research* **47**,  
1306 D678-D686, doi:10.1093/nar/gky1127 (2019).

1307 18 Pasolli, E. *et al.* Extensive Unexplored Human Microbiome Diversity Revealed by Over  
1308 150,000 Genomes from Metagenomes Spanning Age, Geography, and Lifestyle. *Cell*  
1309 **176**, 649-662 e620, doi:10.1016/j.cell.2019.01.001 (2019).

1310 19 Dobrindt, U., Hochhut, B., Hentschel, U. & Hacker, J. Genomic islands in pathogenic and  
1311 environmental microorganisms. *Nat Rev Microbiol* **2**, 414-424, doi:10.1038/nrmicro884  
1312 (2004).

1313 20 Juhas, M. *et al.* Genomic islands: tools of bacterial horizontal gene transfer and  
1314 evolution. *FEMS Microbiol Rev* **33**, 376-393, doi:10.1111/j.1574-6976.2008.00136.x  
1315 (2009).

1316 21 Makarova, K. S. *et al.* Evolutionary classification of CRISPR-Cas systems: a burst of  
1317 class 2 and derived variants. *Nat Rev Microbiol* **18**, 67-83, doi:10.1038/s41579-019-  
1318 0299-x (2020).

1319 22 Mahendra, C. *et al.* Broad-spectrum anti-CRISPR proteins facilitate horizontal gene  
1320 transfer. *Nat Microbiol* **5**, 620-629, doi:10.1038/s41564-020-0692-2 (2020).

1321 23 Bondy-Denomy, J., Pawluk, A., Maxwell, K. L. & Davidson, A. R. Bacteriophage genes  
1322 that inactivate the CRISPR/Cas bacterial immune system. *Nature* **493**, 429-432,  
1323 doi:10.1038/nature11723 (2013).

1324 24 Osuna, B. A. *et al.* Listeria Phages Induce Cas9 Degradation to Protect Lysogenic  
1325 Genomes. *Cell Host Microbe* **28**, 31-40 e39, doi:10.1016/j.chom.2020.04.001 (2020).

1326 25 Song, Y. *et al.* High-resolution comparative modeling with RosettaCM. *Structure* **21**,  
1327 1735-1742, doi:10.1016/j.str.2013.08.005 (2013).

1328 26 Janowski, R. & Niessing, D. The large family of PC4-like domains - similar folds and  
1329 functions throughout all kingdoms of life. *RNA Biol* **17**, 1228-1238,  
1330 doi:10.1080/15476286.2020.1761639 (2020).

1331 27 Krissinel, E. & Henrick, K. Inference of macromolecular assemblies from crystalline  
1332 state. *J Mol Biol* **372**, 774-797, doi:10.1016/j.jmb.2007.05.022 (2007).

1333 28 Steigemann, B., Schulz, A. & Werten, S. Bacteriophage T5 encodes a homolog of the  
1334 eukaryotic transcription coactivator PC4 implicated in recombination-dependent DNA  
1335 replication. *J Mol Biol* **425**, 4125-4133, doi:10.1016/j.jmb.2013.09.001 (2013).

1336 29 Werten, S. Identification of the ssDNA-binding protein of bacteriophage T5: Implications  
1337 for T5 replication. *Bacteriophage* **3**, e27304, doi:10.4161/bact.27304 (2013).

1338 30 Werten, S. *et al.* High-affinity DNA binding by the C-terminal domain of the  
1339 transcriptional coactivator PC4 requires simultaneous interaction with two opposing  
1340 unpaired strands and results in helix destabilization. *J Mol Biol* **276**, 367-377,  
1341 doi:10.1006/jmbi.1997.1534 (1998).

1342 31 Dorman, C. J. & Ni Bhriain, N. CRISPR-Cas, DNA Supercoiling, and Nucleoid-  
1343 Associated Proteins. *Trends Microbiol* **28**, 19-27, doi:10.1016/j.tim.2019.08.004 (2020).

1344 32 Xiong, X. *et al.* SspABCD–SspE is a phosphorothioation-sensing bacterial defence  
1345 system with broad anti-phage activities. *Nature Microbiology* **5**, 917-928,  
1346 doi:10.1038/s41564-020-0700-6 (2020).

1347 33 Yang, W. Nucleases: diversity of structure, function and mechanism. *Q Rev Biophys* **44**,  
1348 1-93, doi:10.1017/S0033583510000181 (2011).

1349 34 Vink, J. N. A. *et al.* Direct Visualization of Native CRISPR Target Search in Live Bacteria  
1350 Reveals Cascade DNA Surveillance Mechanism. *Mol Cell* **77**, 39-50 e10,  
1351 doi:10.1016/j.molcel.2019.10.021 (2020).

1352 35 Harshey, R. M. Transposable Phage Mu. *Microbiol Spectr* **2**,  
1353 10.1128/microbiolspec.MDNA1123-0007-2014, doi:10.1128/microbiolspec.MDNA3-  
1354 0007-2014 (2014).

1355 36 Westra, E. R. *et al.* CRISPR immunity relies on the consecutive binding and degradation  
1356 of negatively supercoiled invader DNA by Cascade and Cas3. *Mol Cell* **46**, 595-605,  
1357 doi:10.1016/j.molcel.2012.03.018 (2012).

1358 37 Mattenberger, Y., Silva, F. & Belin, D. 55.2, a phage T4 ORFan gene, encodes an  
1359 inhibitor of *Escherichia coli* topoisomerase I and increases phage fitness. *PLoS One* **10**,  
1360 e0124309, doi:10.1371/journal.pone.0124309 (2015).

1361 38 Ramirez-Chamorro, L., Boulanger, P. & Rossier, O. Strategies for Bacteriophage T5  
1362 Mutagenesis: Expanding the Toolbox for Phage Genome Engineering. *Frontiers in*  
1363 *Microbiology* **12**, 816 (2021).

1364 39 Johnston, J. V., Nichols, B. P. & Donelson, J. E. Distribution of "minor" nicks in  
1365 bacteriophage T5 DNA. *J Virol* **22**, 510-519 (1977).

1366 40 Roy, D., Huguet, K. T., Grenier, F. & Burrus, V. IncC conjugative plasmids and  
1367 SXT/R391 elements repair double-strand breaks caused by CRISPR–Cas during  
1368 conjugation. *Nucleic Acids Research*, doi:10.1093/nar/gkaa518 (2020).

1369 41 Weigel, C. & Seitz, H. Bacteriophage replication modules. *FEMS Microbiol Rev* **30**, 321-  
1370 381, doi:10.1111/j.1574-6976.2006.00015.x (2006).

1371 42 Uribe, R. V. *et al.* Discovery and Characterization of Cas9 Inhibitors Disseminated  
1372 across Seven Bacterial Phyla. *Cell Host Microbe* **25**, 233-241 e235,  
1373 doi:10.1016/j.chom.2019.01.003 (2019).

1374 43 Borges, A. L. *et al.* Bacteriophage Cooperation Suppresses CRISPR-Cas3 and Cas9  
1375 Immunity. *Cell* **174**, 917-925 e910, doi:10.1016/j.cell.2018.06.013 (2018).

1376 44 Landsberger, M. *et al.* Anti-CRISPR Phages Cooperate to Overcome CRISPR-Cas  
1377 Immunity. *Cell* **174**, 908-916 e912, doi:10.1016/j.cell.2018.05.058 (2018).

1378 45 Chevallereau, A. *et al.* Exploitation of the Cooperative Behaviors of Anti-CRISPR  
1379 Phages. *Cell Host Microbe* **27**, 189-198 e186, doi:10.1016/j.chom.2019.12.004 (2020).

1380 46 Hooper, D. C. & Jacoby, G. A. Mechanisms of drug resistance: quinolone resistance.  
1381 *Ann N Y Acad Sci* **1354**, 12-31, doi:10.1111/nyas.12830 (2015).

1382 47 Pawluk, A., Davidson, A. R. & Maxwell, K. L. Anti-CRISPR: discovery, mechanism and  
1383 function. *Nat Rev Microbiol*, doi:10.1038/nrmicro.2017.120 (2017).

1384 48 Borges, A. L., Davidson, A. R. & Bondy-Denomy, J. The Discovery, Mechanisms, and  
1385 Evolutionary Impact of Anti-CRISPRs. *Annu Rev Virol* **4**, 37-59, doi:10.1146/annurev-  
1386 virology-101416-041616 (2017).

1387 49 Li, W. & Godzik, A. Cd-hit: a fast program for clustering and comparing large sets of  
1388 protein or nucleotide sequences. *Bioinformatics* **22**, 1658-1659,  
1389 doi:10.1093/bioinformatics/btl158 (2006).

1390 50 Zhu, W., Lomsadze, A. & Borodovsky, M. Ab initio gene identification in metagenomic  
1391 sequences. *Nucleic Acids Res* **38**, e132, doi:10.1093/nar/gkq275 (2010).

1392 51 Finn, R. D., Clements, J. & Eddy, S. R. HMMER web server: interactive sequence  
1393 similarity searching. *Nucleic Acids Res* **39**, W29-37, doi:10.1093/nar/gkr367 (2011).

1394 52 Haft, D. H. *et al.* TIGRFAMs: a protein family resource for the functional identification of  
1395 proteins. *Nucleic Acids Res* **29**, 41-43 (2001).

1396 53 Bateman, A. *et al.* The Pfam protein families database. *Nucleic Acids Res* **28**, 263-266  
1397 (2000).

1398 54 Parks, D. H. *et al.* A complete domain-to-species taxonomy for Bacteria and Archaea.  
1399 *Nat Biotechnol*, doi:10.1038/s41587-020-0501-8 (2020).

1400 55 Parks, D. H. *et al.* A standardized bacterial taxonomy based on genome phylogeny  
1401 substantially revises the tree of life. *Nat Biotechnol* **36**, 996-1004, doi:10.1038/nbt.4229  
1402 (2018).

1403 56 Le, S. Q. & Gascuel, O. An Improved General Amino Acid Replacement Matrix.  
1404 *Molecular Biology and Evolution* **25**, 1307-1320, doi:10.1093/molbev/msn067 (2008).

1405 57 Russel, J., Pinilla-Redondo, R., Mayo-Muñoz, D., Shah, S. A. & Sørensen, S. J.  
1406 CRISPRCasTyper: An automated tool for the identification, annotation and classification  
1407 of CRISPR-Cas loci. *bioRxiv*, 2020.2005.2015.097824, doi:10.1101/2020.05.15.097824  
1408 (2020).

1409 58 Bondy-Denomy, J. *et al.* A Unified Resource for Tracking Anti-CRISPR Names. *The  
1410 CRISPR Journal* **1**, 304-305, doi:10.1089/crispr.2018.0043 (2018).

1411 59 Emsley, P., Lohkamp, B., Scott, W. G. & Cowtan, K. Features and development of Coot.  
1412 *Acta Crystallogr D Biol Crystallogr* **66**, 486-501, doi:10.1107/S0907444910007493  
1413 (2010).

1414 60 Adams, P. D. *et al.* PHENIX: a comprehensive Python-based system for macromolecular  
1415 structure solution. *Acta Crystallogr D Biol Crystallogr* **66**, 213-221,  
1416 doi:10.1107/S0907444909052925 (2010).  
1417 61 Harrington, L. B. *et al.* A Broad-Spectrum Inhibitor of CRISPR-Cas9. *Cell*,  
1418 doi:10.1016/j.cell.2017.07.037 (2017).

**Table 1.** Structural features of AcrlIA22.

<b>Data collection</b>	
Space Group	P4332
<i>Cell Dimensions</i>	
a, b, c (Å)	128.56, 128.56, 128.56
α, β, γ (°)	90.0, 90.0, 90.0
Resolution (Å)	50.00 - 2.80
R <sub>merge</sub>	0.106 (0.906)
I/σ <sub>I</sub>	17.4 (2.6)
Completeness (%)	98.7 (100.0)
Redundancy	10.4 (10.7)
CC 1/2	0.837
<b>Refinement</b>	
No. Reflections	9334
R <sub>work</sub> (R <sub>free</sub> ) (%)	22.2 (24.6)
No. Complex in ASU	2
<i>No. atoms</i>	
Protein	810
Heteroatoms	50
Water	3
B-factor	82.82
<i>R.m.s deviations</i>	
Bond lengths (Å)	0.003
Bond angles (°)	0.610
<i>Ramachandran</i>	
Preferred (%)	98.15
Allowed (%)	1.85
Outliers (%)	0

## Other supplemental materials.

**Supplemental Table 1.** Whether known anti-CRISPRs can bind Cas proteins or inhibit their cleavage activity as purified proteins.

**Supplemental Table 2.** PC4-like proteins with structural homology to AcrIIA22.

**Supplemental Table 3.** Descriptions of all sequences used in this study. All sequences and annotations are also available as supplemental data.

**Supplemental Table 4.** Plasmids used in this study.

**Supplemental Table 5.** Gene sequences used in this study.

**SI\_Data.** All raw data for main and supplemental figures depicted in this study (as a spreadsheet).

**SI\_raw\_images.** Full gel images for all cropped gels depicted in this study, compiled into a .pdf document.

**Supplemental Dataset 1.** 68 contigs sequences referenced in the manuscript with Pfam, TIGRFAM, and AcrIIA22 homolog annotations (in genbank format).

**Supplemental Dataset 2.** 68 contigs sequences referenced in the manuscript (in fasta format).

**Supplemental Dataset 3.** Nine AcrIIA22-encoding prophage sequences referenced in the manuscript with Pfam, TIGRFAM, and AcrIIA22 homolog annotations (in genbank format).

**Supplemental Dataset 4.** Nine AcrIIA22-encoding prophage sequences referenced in the manuscript (in fasta format).

**Supplemental Dataset 5.** All metagenomic contigs with  $\geq 98\%$  nucleotide identity to *acrIIA22*-associated genes, *purF* and *radC*. Pfam, TIGRFAM, and AcrIIA22 homolog annotations are also provided (file in genbank format).

**Supplemental Dataset 6.** Amino acid sequence alignment of 30 AcrIIA22 homologs (in fasta format).

**Supplemental Dataset 7.** The detailed PDB validation report for AcrIIA22's crystal structure.

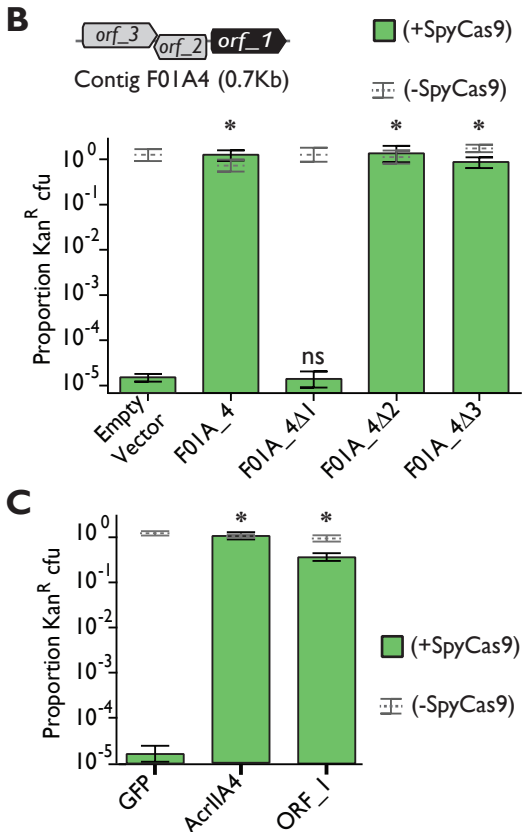
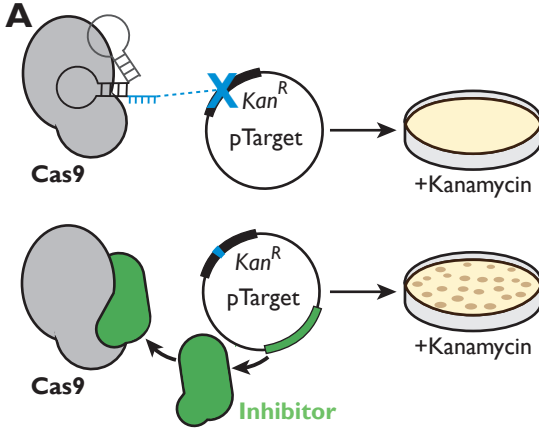


**Figure 1. Functional selection reveals a metagenomic contig encoding a novel SpyCas9 inhibitor.** (A) A plasmid protection assay was used to reveal SpyCas9 inhibition. In this assay, plasmids without SpyCas9 inhibitors are cleaved by Cas9 and do not give rise to Kan<sup>R</sup> colonies, whereas those encoding inhibitors withstand SpyCas9 attack and yield Kan<sup>R</sup> colonies. (B) The contig F01A\_4 protects a plasmid from SpyCas9 attack but an early stop codon in *orf\_1* ( $\Delta 1$ ) eliminates this phenotype. Stop codons in *orf\_2* or *orf\_3* ( $\Delta 2$  and  $\Delta 3$ ) have no effect. Thus, we conclude that *orf\_1* is necessary for inhibition of SpyCas9. Asterisks depict statistically significant differences in plasmid retention between the indicated genotype and an empty vector control in SpyCas9-inducing conditions (Student's t-test,  $p<0.002$ ,  $n=3$ ); ns indicates no significance. All p-values were corrected for multiple hypotheses using Bonferroni's method. (C) Expression of *orf\_1* (which we name *acrlA22*) is sufficient for SpyCas9 antagonism, protecting a plasmid as effectively as *acrlA4*. Asterisks are as in panel B but relate to the GFP negative control rather than to an empty vector. The individual numerical values that underlie the summary data in this figure may be found as supporting information file SI\_Data.

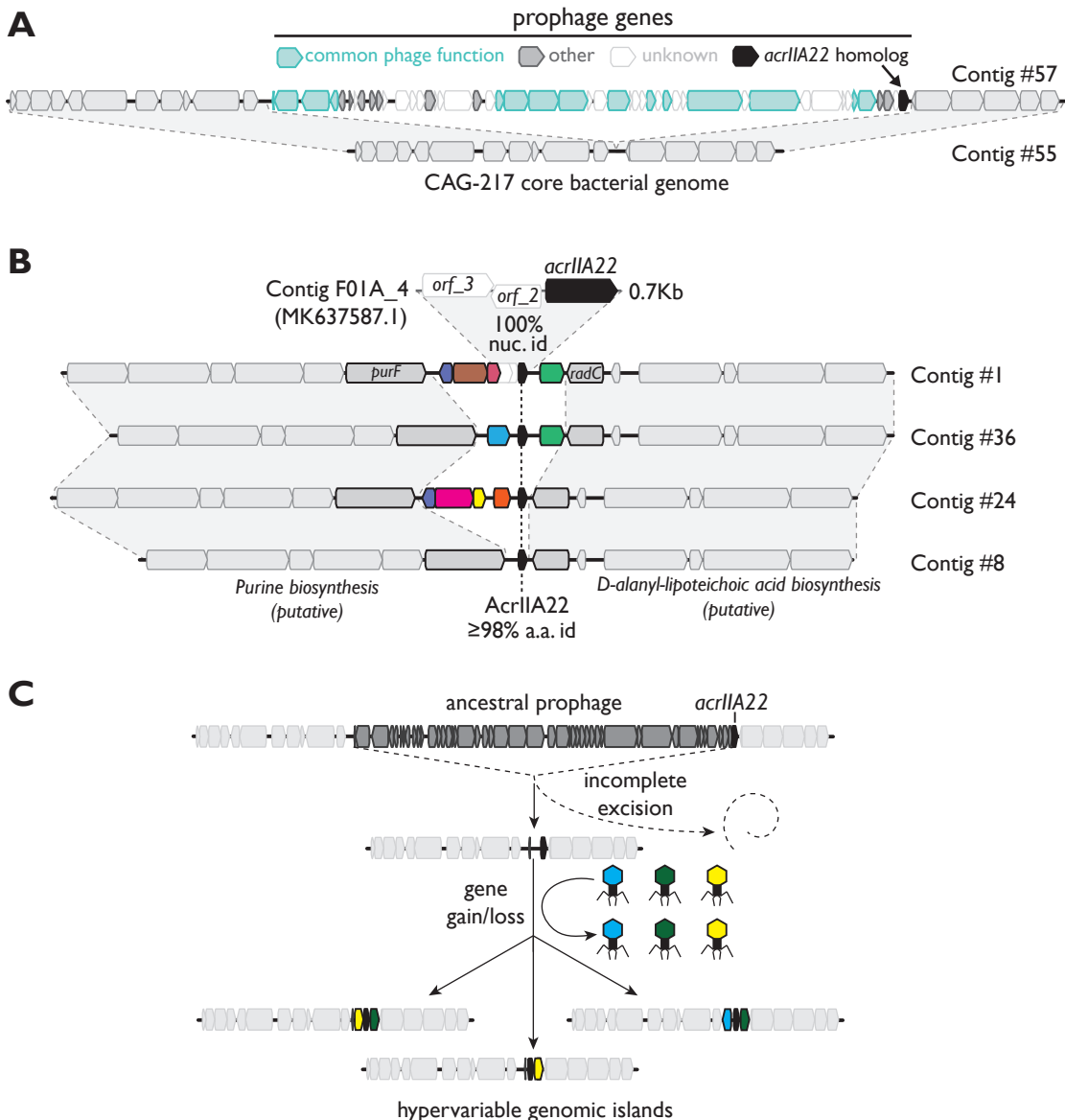


**Figure 2. *AcrIIA22* homologs are found in hypervariable regions of prophage and bacterial genomes in the unnamed clostridial genus, CAG-217. (A)** We show a schematic representation of an *acrIIA22* homolog embedded in a prophage genome, which is integrated into a bacterial genome (contig #57). We can delineate precise boundaries of the inserted prophage based on comparison to a near-identical bacterial contig (contig #55). Prophage genes are colored by functional category, according to the legend at the top. Bacterial genes are colored light gray. **(B)** Homologs of *acrIIA22* are depicted in diverse genomic islands, including Contig #1, whose sequence includes a portion identical to F01A\_4, the original metagenomic contig we recovered. All *acrIIA22* homologs in these loci are closely related but their adjacent genes are different, unrelated gene families (depicted by different colors). Genomic regions flanking these hypervariable islands, including genes immediately adjacent to these islands (*purF* and *radC*, in bold outlines), are nearly identical to one another ( $\geq 98\%$  nucleotide identity). Contigs are numbered to indicate their descriptions in Supplemental Table 3, which contains their metadata, taxonomy, and sequence retrieval information. All sequences and annotations may also be found in Supplemental Datasets 1 and 2. **(C)** We propose an evolutionary model for the origin of the *acrIIA22*-encoding hypervariable genomic islands depicted in panel B. We propose that *acrIIA22* moved via prophage integration into a bacterial genomic locus but remained following an incomplete prophage excision event. Its neighboring genes subsequently diversified via horizontal exchange with additional phage genomes without these phage genomes inserting into the locus. Supplemental Figure 4 depicts a more detailed version of the genomic data underlying this model.

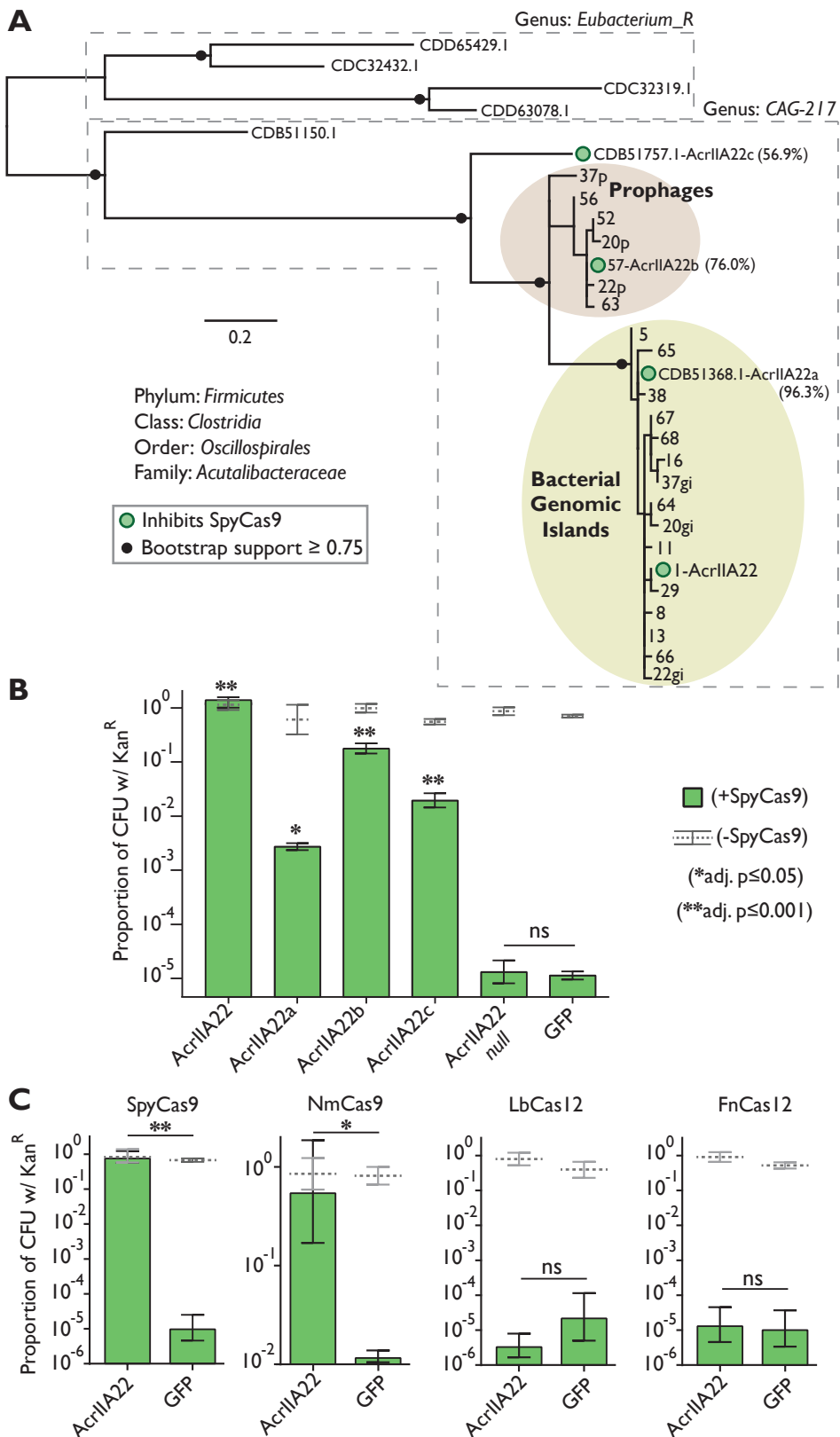


**Figure 3. Several AcrIIA22 homologs in the CAG-217 clostridial genus can inhibit SpyCas9.** (A) A phylogeny of all unique AcrIIA22 homologs identified from metagenomic and NCBI databases. Phylogenetic classifications were assigned corresponding to the GTDB naming convention (Methods). Prophage sequences are shaded brown and homologs from hypervariable bacterial genomic islands are shaded yellow. Sequences obtained from NCBI are labeled with protein accession numbers. In other cases, AcrIIA22 homologs are numbered to match their contig-of-origin (Supplemental Table 3). In some cases, more than one AcrIIA22 homolog is found on the same contig ('gi' or 'p' indicates its presence in a hypervariable genomic island or prophage genome, respectively). Circles at nodes indicate bootstrap support  $\geq 0.75$ . Dashed boxes separate sequences identified from CAG-217 versus *Eubacterium\_R* bacterial genera. Filled green circles indicate homologs that were tested for their ability to inhibit SpyCas9 in the plasmid protection assay in panel B. These homologs have been named with 'a', 'b', or 'c' suffixes to distinguish them from the original AcrIIA22 metagenomic hit; their amino acid identity to the original hit is shown in parentheses. (B) Several homologs of AcrIIA22 in CAG-217 genomes inhibit SpyCas9. Asterisks depict statistically significant differences in plasmid retention under SpyCas9-inducing conditions between the indicated sample and a null mutant with an early stop codon in *acrIIA22*, as indicated in the legend at right (ns indicates no significance;  $p > 0.05$ ). All  $p$ -values were corrected for multiple hypotheses using Bonferroni's method (Student's t-test,  $n=3$ ). (C) AcrIIA22 inhibits divergent Cas9 proteins from *Streptococcus pyogenes* (SpyCas9) or *Neisseria meningitidis* (NmCas9) but not Cas12 proteins from *Lachnospiraceae bacterium* (LbCas12) or *Francisella novicida* (FnCas12). As in panel B, green bars indicate samples with expression of the indicated Cas nuclease while unexpressed controls are depicted with gray lines. For Cas-expressing samples, significance was determined via a Student's t-test ( $n=3$ ) and denoted as follows: \*\*,  $p \leq 0.05$  ; \*\*\*,  $p \leq 0.001$  ; 'ns' no significance. Due to slight differences in the plasmid protection assay in panel C compared to panel B, A22 was re-tested against SpyCas9 to confirm activity (Methods). The individual numerical values that underlie the summary data in this figure may be found as supporting information file SI\_Data.

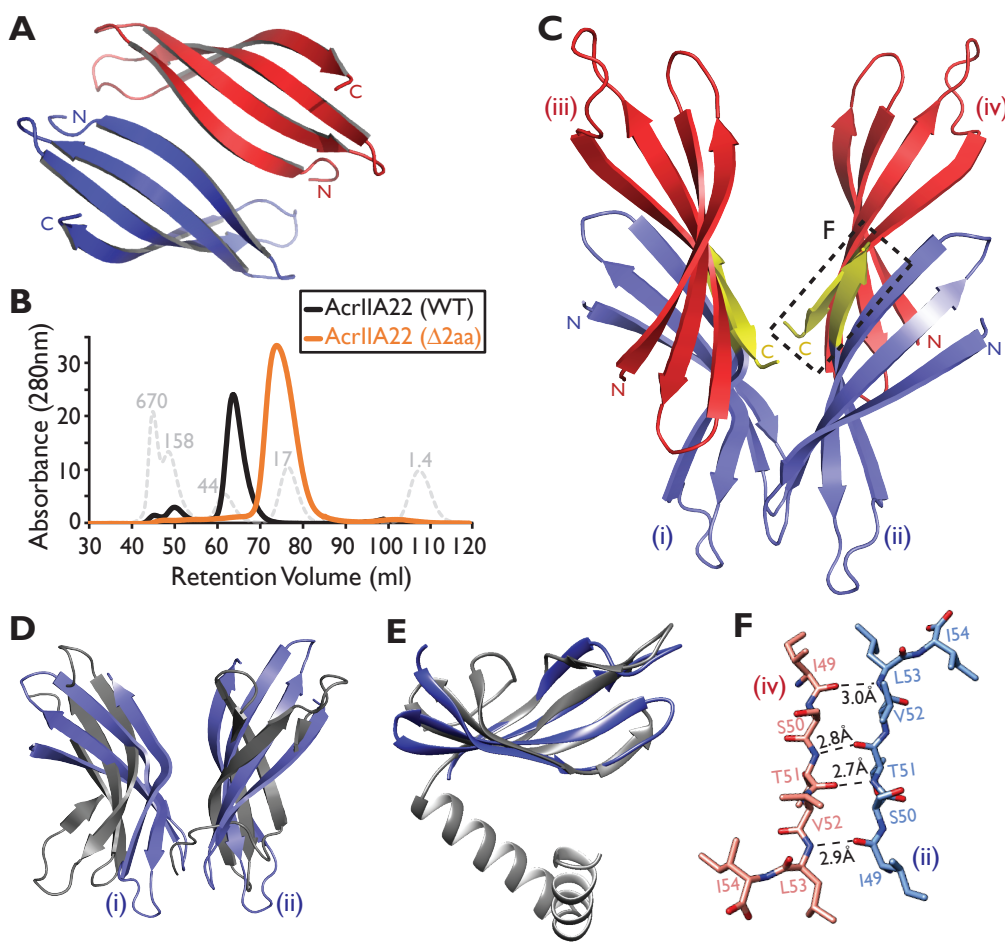


**Figure 4. AcrIIA22 is an oligomeric PC4-like protein.** (A) AcrIIA22's crystal structure reveals a homodimer of two four-stranded  $\beta$ -sheets. (B) AcrIIA22 elutes as an oligomer that is approximately four times the predicted molecular mass of its monomer, which is 7 kDa. The gray, dashed trace depicts protein standards of the indicated molecular weight, in kDa. The orange trace depicts the elution profile of a two-amino acid C-terminal AcrIIA22 truncation mutant that is predicted to disrupt oligomerization. (C) Ribbon diagram of a proposed AcrIIA22 tetramer which requires binding between anti-parallel  $\beta$ -strands at the C-termini of AcrIIA22 monomers to form extended, concave  $\beta$ -sheets. The putative oligomerization interface is indicated by the regions highlighted in yellow and the dashed box, and is detailed further in panel F. Each monomer in the proposed tetramer is labeled with lower-case Roman numerals (i-iv). (D)  $\beta$ -sheet topology and orientation in AcrIIA22 (blue) resemble that of PC4-like family proteins (in gray, PDB:4BG7 from phage T5). (E) A monomer of AcrIIA22 (in blue, PDB:7JTA) is structurally similar to a PC4-like single-stranded DNA binding protein, which is proposed to promote recombination in phage T5 (in gray, PDB:4BG7, Z-score=6.2, matched residues 15%), except for a missing C-terminal alpha helix. (F) A putative oligomerization interface between the C-termini of two AcrIIA22 monomers from panel (C) is shown in more detail. Dashed lines indicate potential hydrogen bonds between the polypeptide backbones. This interface occurs twice in the putative tetramer, between red-hued and blue-hued monomers in panel C.

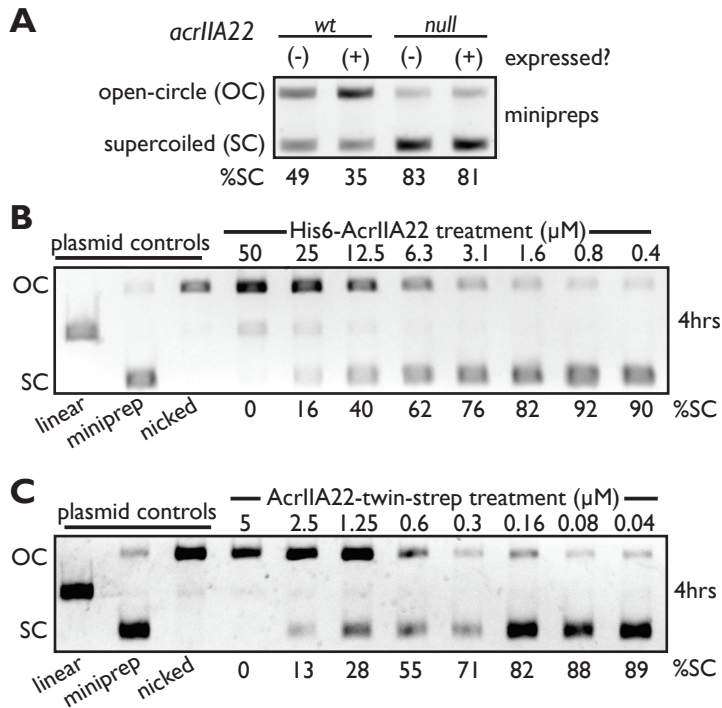


**Figure 5. AcrlIA22 nicks supercoiled plasmids *in vivo* and *in vitro*.** (A) Gel electrophoresis of plasmids purified from overnight *E. coli* cultures expressing either *acrlIA22*, or a null mutant with an early stop codon, or neither. Compared to the null mutant, more plasmid runs in a slowly migrating, open-circle conformation (OC) rather than supercoiled plasmid (SC) with the wild-type *acrlIA22* allele, suggesting that *acrlIA22* may impact plasmid topology. %SC indicates the percentage of DNA in the supercoiled form for each sample. (B) N-terminally His6-tagged AcrlIA22 nicks supercoiled plasmids *in vitro*. (C) C-terminally twin-strep-tagged AcrlIA22 nicks supercoiled plasmids *in vitro* with higher specific activity than shown in panel B (compare protein concentrations). Original, uncropped versions of images depicted in figure may be found in the supporting information file, SI\_raw\_images.

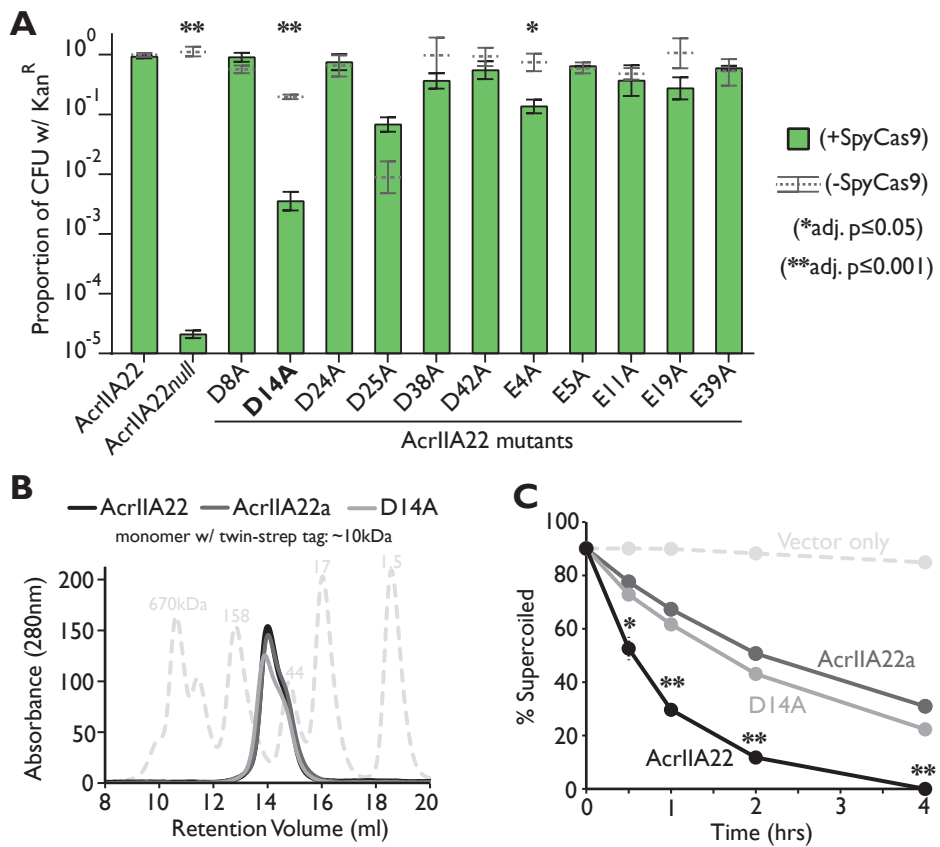


**Figure 6. Impaired nicking activity of AcrlIA22 variants *in vitro* correlates with lower SpyCas9 inhibition *in vivo*.** (A) Alanine mutagenesis of acidic amino acid residues (glutamic acid or aspartic acid) in AcrlIA22 reveals that D14 is important for plasmid protection against SpyCas9. Asterisks depict statistically significant differences in plasmid retention under SpyCas9-inducing and non-inducing conditions, per the legend at right. The D14A mutant is significantly impaired, the E4A mutant is slightly impaired, whereas all other mutants are not impaired for plasmid protection against SpyCas9 compared to an uninduced control. All p-values were corrected for multiple hypotheses using Bonferroni's method (Student's t-test, n=3). (B) AcrlIA22 (black), AcrlIA22a (dark gray), and a D14A mutant (light gray) all elute with similar oligomer profiles via SEC. The dashed trace depicts protein standards of the indicated molecular weight, in kDa. (C) AcrlIA22a and the D14A mutant are impaired for nicking relative to AcrlIA22. All experiments were performed in triplicate, with standard deviations indicated by dashed lines (in most cases, the data points obscure these error bars). Asterisks denote cases where AcrlIA22 is significantly different than both AcrlIA22a and the D14A mutant after correcting for multiple hypotheses (Student's t-test, n=3, Bonferroni correction). A single asterisk (\*) means that adjusted p-values for both comparisons are below 0.05. A double asterisk (\*\*) means that adjusted p-values are both below 0.005. Supplemental Figures 10G and 10H show representative gels for these nicking experiments. The individual numerical values that underlie the summary data in this figure may be found as supporting information file SI\_Data.

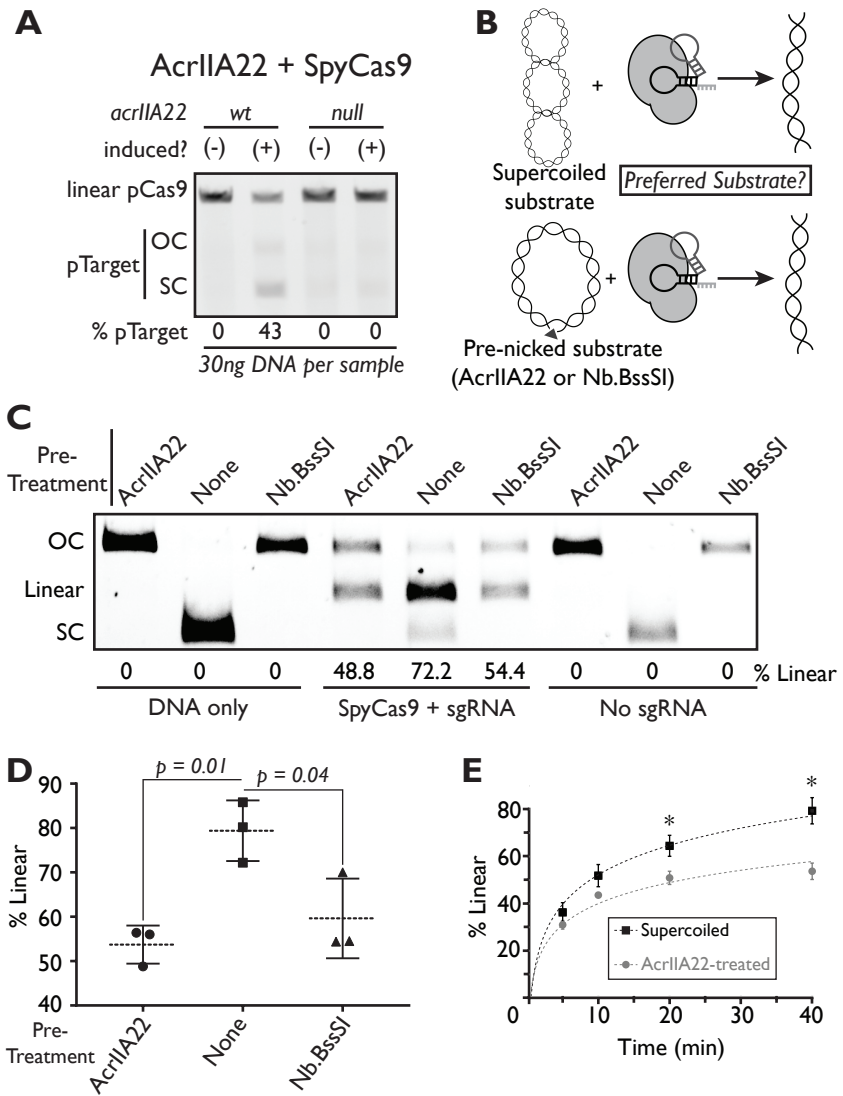
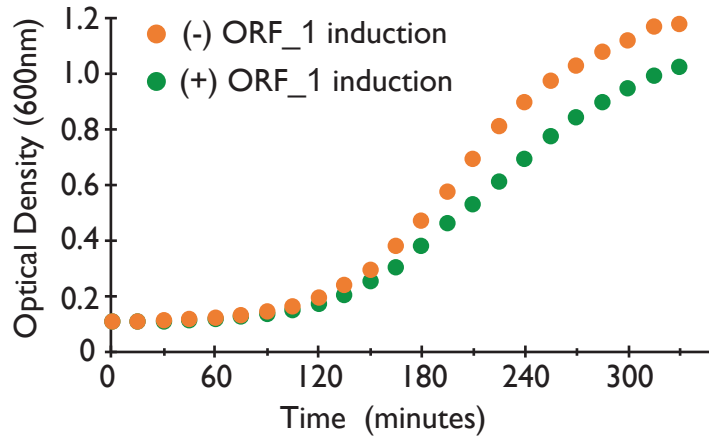
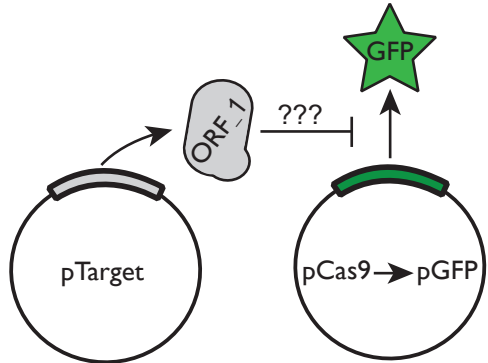


**Figure 7. Nicking by AcrlIA22 protects plasmids from SpyCas9 *in vivo* and *in vitro*.** (A) Gel electrophoresis of plasmids purified from overnight *E. coli* cultures expressing either wildtype *acrlIA22* or a mutant with an early stop codon ('null'). In these cultures, SpyCas9 was expressed from a second plasmid, which was linearized via a unique restriction site before electrophoresis. The *acrlIA22*-encoding plasmids are indicated with the 'pTarget' label. OC, open-circle; SC, supercoiled. The '%pTarget' figure indicates the fraction of total DNA attributable to pTarget, quantified by densitometry analysis. In cases with complete pTarget elimination, all DNA comes from the SpyCas9 expression plasmid, and thus these bands are more pronounced. However, in the presence of wildtype acrlIA22, pTarget is protected from SpyCas9-mediated cleavage and makes up 43% of total plasmid DNA. (B) We present a schematic of the experimental design for the data depicted in panel C. The experiment tests whether SpyCas9 preferentially cleaves a supercoiled or open-circle plasmid target *in vitro*. Though both plasmid substrates will be linearized following SpyCas9 cleavage, linear DNA will accumulate more readily with a preferred substrate. (C) Plasmid purifications from overnight cultures were either left unmodified or pre-treated with one of two nickase enzymes, AcrlIA22 or Nb.BssSI, following which each substrate was digested with SpyCas9 *in vitro*. The percentage of DNA in the linear form is quantified below the gel, which indicates complete SpyCas9 cleavage. Linear, open-circle (OC), and supercoiled (SC) plasmid forms are indicated along with the left of the gel, and reaction components below the gel. SpyCas9 cuts DNA strands sequentially; incomplete digestions with supercoiled substrates produce open-circle plasmids if only one strand has been cleaved (e.g. lane 5). Pre-nicked plasmids, by either AcrlIA22 or Nb.BssSI, are less susceptible to linearization via SpyCas9 cleavage. (D) Endpoint measurements indicate that SpyCas9 more efficiently linearizes supercoiled plasmids than substrates nicked with either AcrlIA22 or Nb.BssSI (Student's t-test,  $n=3$ ). (E) A time course experiment demonstrates that SpyCas9 more efficiently linearizes supercoiled plasmids than AcrlIA22-treated substrates. An asterisk (\*) denotes significant differences between AcrlIA22-treated and untreated substrates (Student's t-test,  $p < 0.05$ ,  $n=3$ ). The individual numerical values and original images for the data presented in this figure may be found in the supporting information files SI\_Data and SI\_raw\_images, respectively.

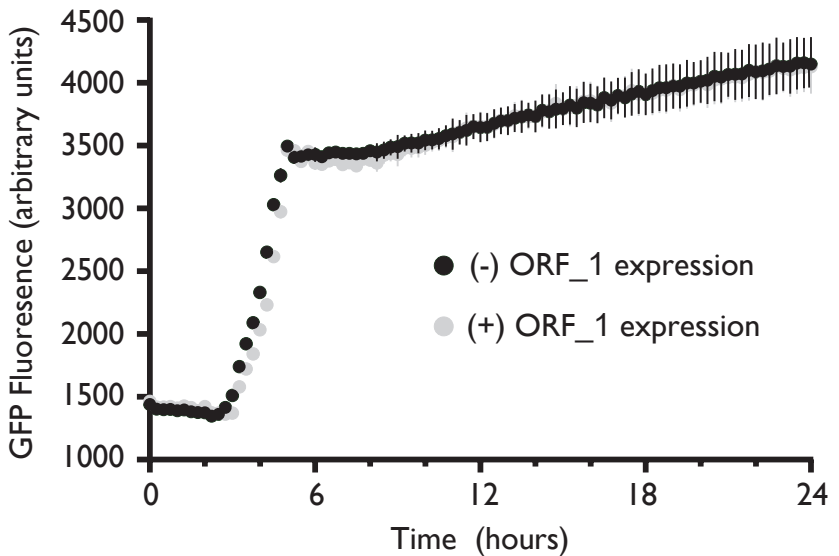


**Supplemental Figure 1. *Orf\_1 (acrIIA22)* confers mild toxicity in *E. coli*.** Growth rates with *orf\_1* induction (green) are 7% lower than those without *orf\_1* induction (orange). The cfu data shown in Figure 1C were generated from the same experiment depicted here (samples were removed after six hours of growth to determine these cfu counts). Thus, these data demonstrate that anti-SpyCas9 activity occurs under conditions with mild *orf\_1* toxicity. Growth curves are shown for samples without SpyCas9 induction to ensure that *orf\_1* toxicity is not mitigated due to elimination of its plasmid. Points indicate averages from three replicates. Standard deviations at each timepoint are so small that the error bars do not exceed the bounds of the data point.

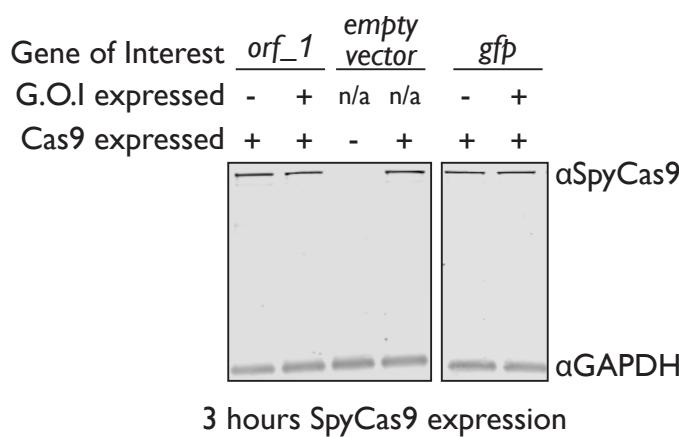
**A**



**B**

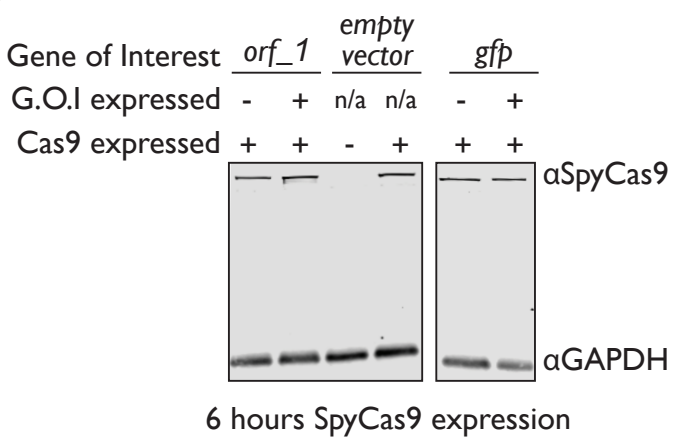


**C**



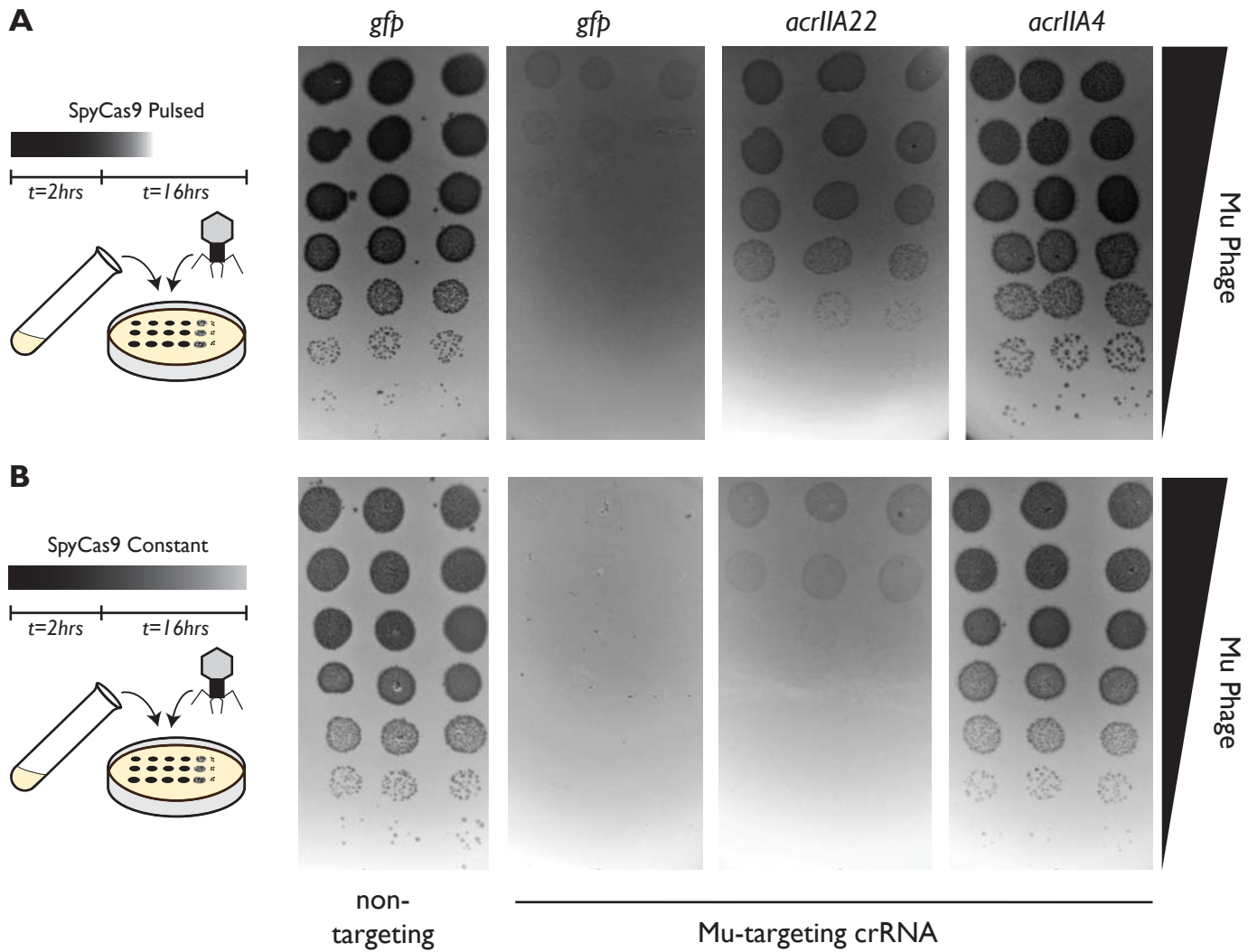
3 hours SpyCas9 expression

**D**

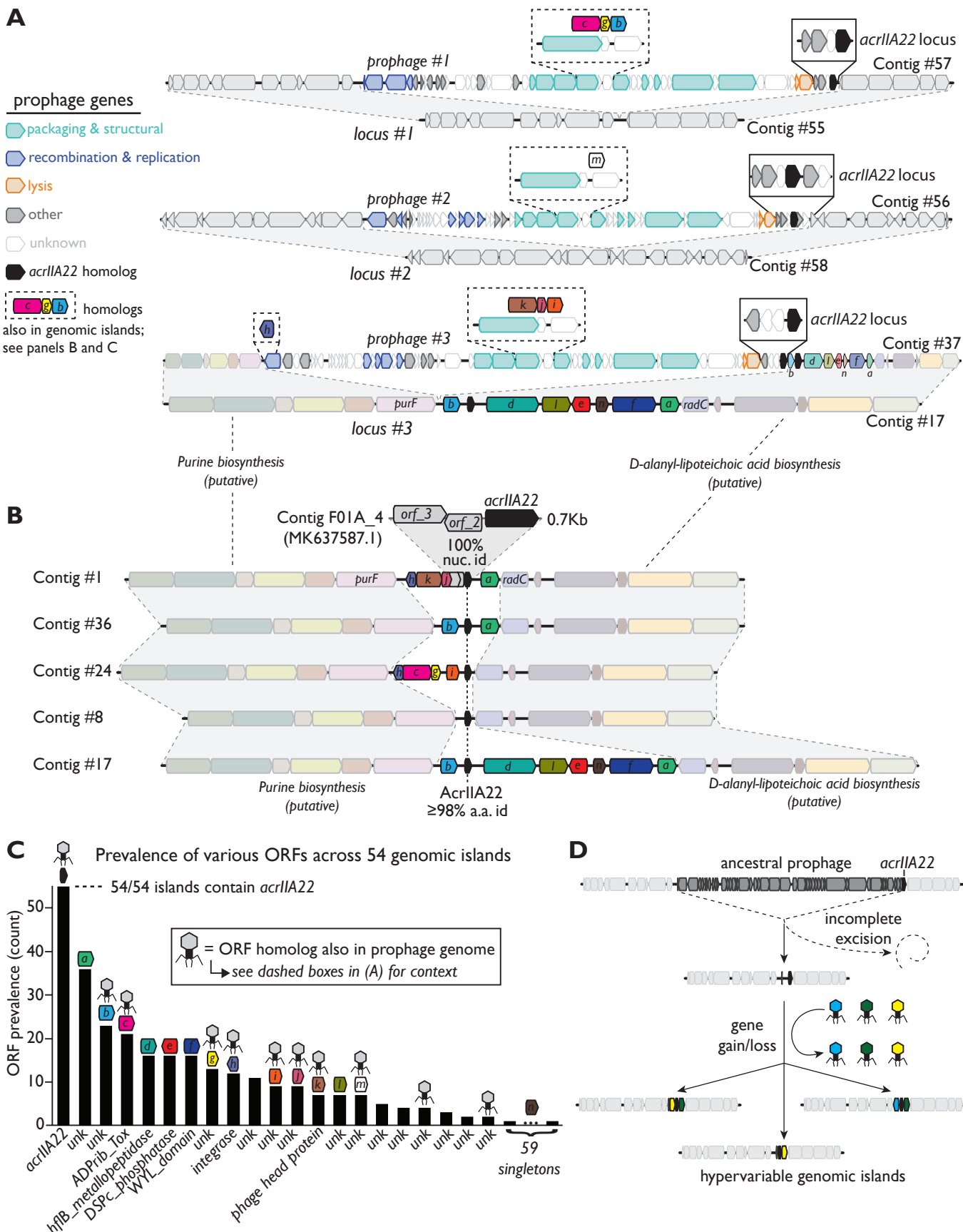


6 hours SpyCas9 expression

**Supplemental Figure 2. *Orf\_1* (*acrIIA22*) does not impact SpyCas9 expression.** (A) A schematic description of the experimental design shown in panel (B) is presented. If ORF\_1 prevented transcription from pCas9 or altered its copy number, we would expect expression of the *orf\_1* gene to deplete the level of green fluorescence observed from a construct that replaces the *spycas9* gene with *gfp*. (B) Fluorescence measurements for the experiment depicted in panel A show that ORF\_1 does not impact GFP expression throughout an *E. coli* growth curve. Points indicate averages from three replicates, error bars indicate standard deviation. A western blot shows no depletion of SpyCas9 expression as a function of ORF\_1 or GFP expression in growing *E. coli* cultures at three hours (C) or six hours (D). As an internal control, GAPDH expression was also detected.

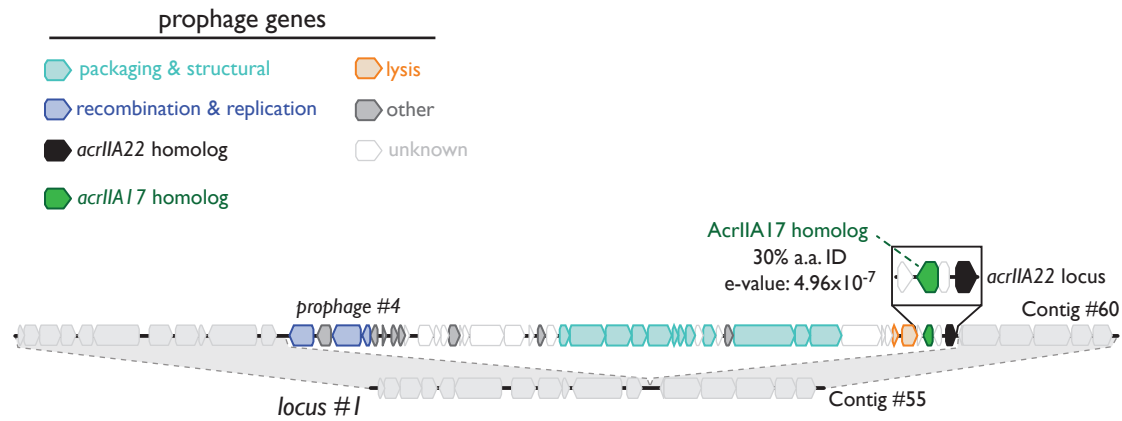


**Supplemental Figure 3. AcrIIA22 only modestly protects Mu phages against SpyCas9.** Mu phage fitness was measured by plaquing on *E. coli* in the presence of *gfp*, *acrIIA22*, or *acrIIA4* via serial ten-fold dilutions. Bacterial clearing (black) occurs when phage Mu overcomes SpyCas9 immunity and lyses *E. coli*. In (A) and in (B), SpyCas9 with a Mu-targeting crRNA confers substantial protection against phage Mu relative to a non-targeting (n.t.) control, in both conditions tested. These conditions are depicted at left, with the only difference being whether SpyCas9 was only expressed in liquid growth prior to phage infection (panel A) or expressed both in liquid media and in solid media throughout infection (panel B). When expressed from a second plasmid, the positive control *acrIIA4* significantly enhances Mu fitness by inhibiting SpyCas9 in all conditions *in trans*. Though *acrIIA22* confers protection against SpyCas9 compared to *gfp* (negative control), this effect is milder than with *acrIIA4* and dependent on SpyCas9 expression.

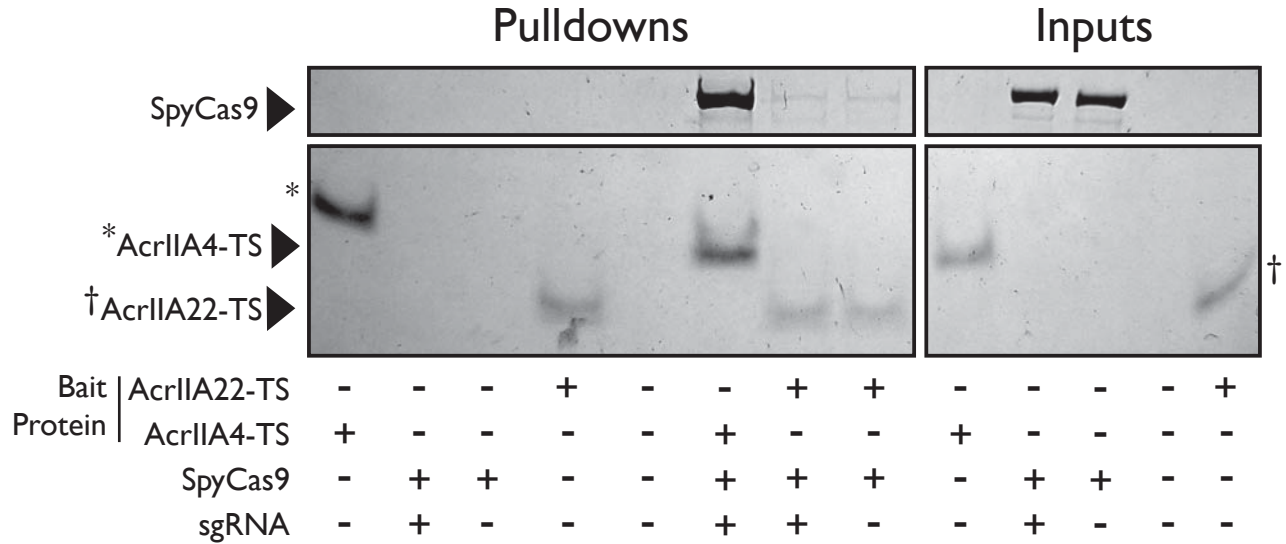


## Supplemental Figure 4.

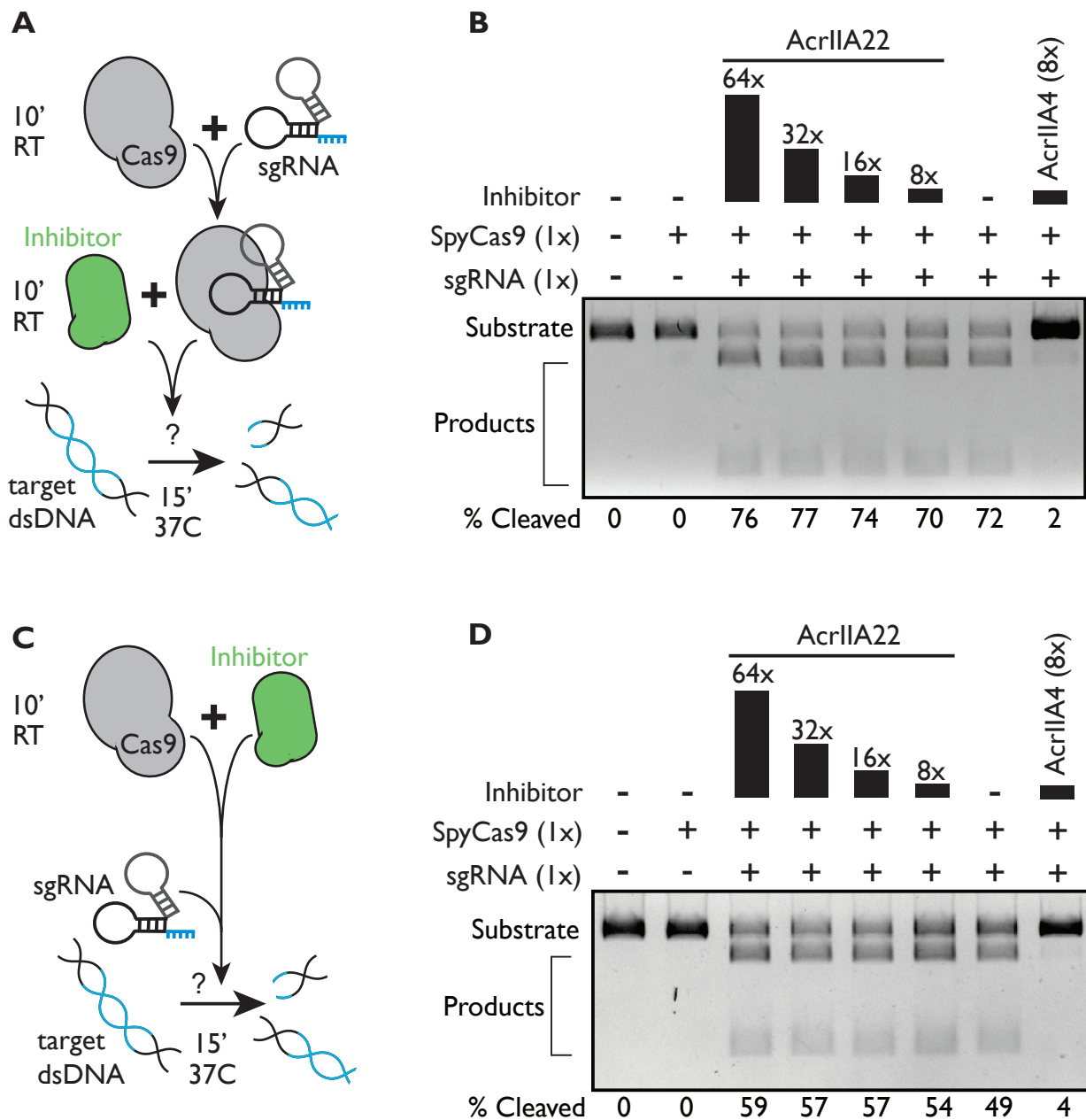
**Supplemental Figure 4. *AcrlIA22* homologs are found in hypervariable regions of prophage and bacterial genomes in the CAG-217clostridial genus.** (A) Homologs of *acrlIA22* are depicted in three related prophage genomes, integrated at three different genomic loci, revealed by a comparison of prophage-bearing contigs (#57, #56, #37) relative to unintegrated contigs (#55, #58, #17 respectively), which are otherwise nearly identical. Prophage genes are colored by functional category, according to the legend at the left of panel A. Genes immediately adjacent to *acrlIA22* (solid boxes) vary across phages, despite strong relatedness across much of the prophage genomes. Bacterial genes are colored gray, except for contig #17, which is also depicted in panel B, below. (B) Homologs of *acrlIA22* are depicted in diverse genomic islands, including Contig #1, whose sequence includes a portion that is identical to the original metagenomic contig we recovered (F01A\_4). All *acrlIA22* homologs in these loci are closely related but differ in their adjacent genes, which often have homologs in the prophages depicted in panel A (dashed boxes). Bacterial genomic regions flanking these hypervariable islands are nearly identical to one another and to prophage integration locus #3, as shown by homology to contig #17 from panel A. Contigs are numbered to indicate their descriptions in Supplemental Table 3, which contains their metadata, taxonomy, and sequence retrieval information. All sequences and annotations can also be found in Supplemental Datasets 1 and 2. (C) We tabulate the prevalence of various protein families (clustered at 65% amino acid identity) in a set of 54 unique genomic islands. Each of these islands is flanked by the conserved genes *purF* and *radC* but contains a different arrangement of encoded genes. Domain-level annotations are indicated below each protein family (unk; unknown function). Gene symbols above each protein family are colored and lettered to indicate their counterparts or homologs in panels A and B. The phage capsid icon indicates sequences with homologs in prophage genomes. (D) An evolutionary model for the origin of the *acrlIA22*-encoding hypervariable genomic islands depicted in panel B is shown. This panel is reprinted from Figure 2C, for continuity. We propose that *acrlIA22* moved via a phage insertion into a bacterial genomic locus, remained following an incomplete prophage excision event, and its neighboring genes subsequently diversified via horizontal exchange with additional phage genomes.



**Supplemental Figure 5. Genomic proximity of *acrIIA22* homologs to other *acr* genes.** An *acrIIA22*-encoding prophage like the one depicted in Figure 2A and those in Supplemental Figure 4A is shown. This prophage encodes for a homolog of the previously described SpyCas9 inhibitor *acrIIA17* within one kilobase of an *acrIIA22* homolog. Sequence relatedness between the depicted *acrIIA17* gene and the originally discovered *acrIIA17* is shown<sup>22</sup>. Because phages often encode multiple *acrs* in the same locus, the co-localization of *acrIIA17* with *acrIIA22* is consistent with the latter gene functioning natively to inhibit CRISPR-Cas activity. Prophage genes are colored by functional category, per the legend and as in Supplemental Figure 4A. Contigs are numbered to indicate their descriptions in Supplemental Table 3, which contains their metadata, taxonomy, and sequence retrieval information. All sequences and annotations can also be found in Supplemental Datasets 1 and 2.

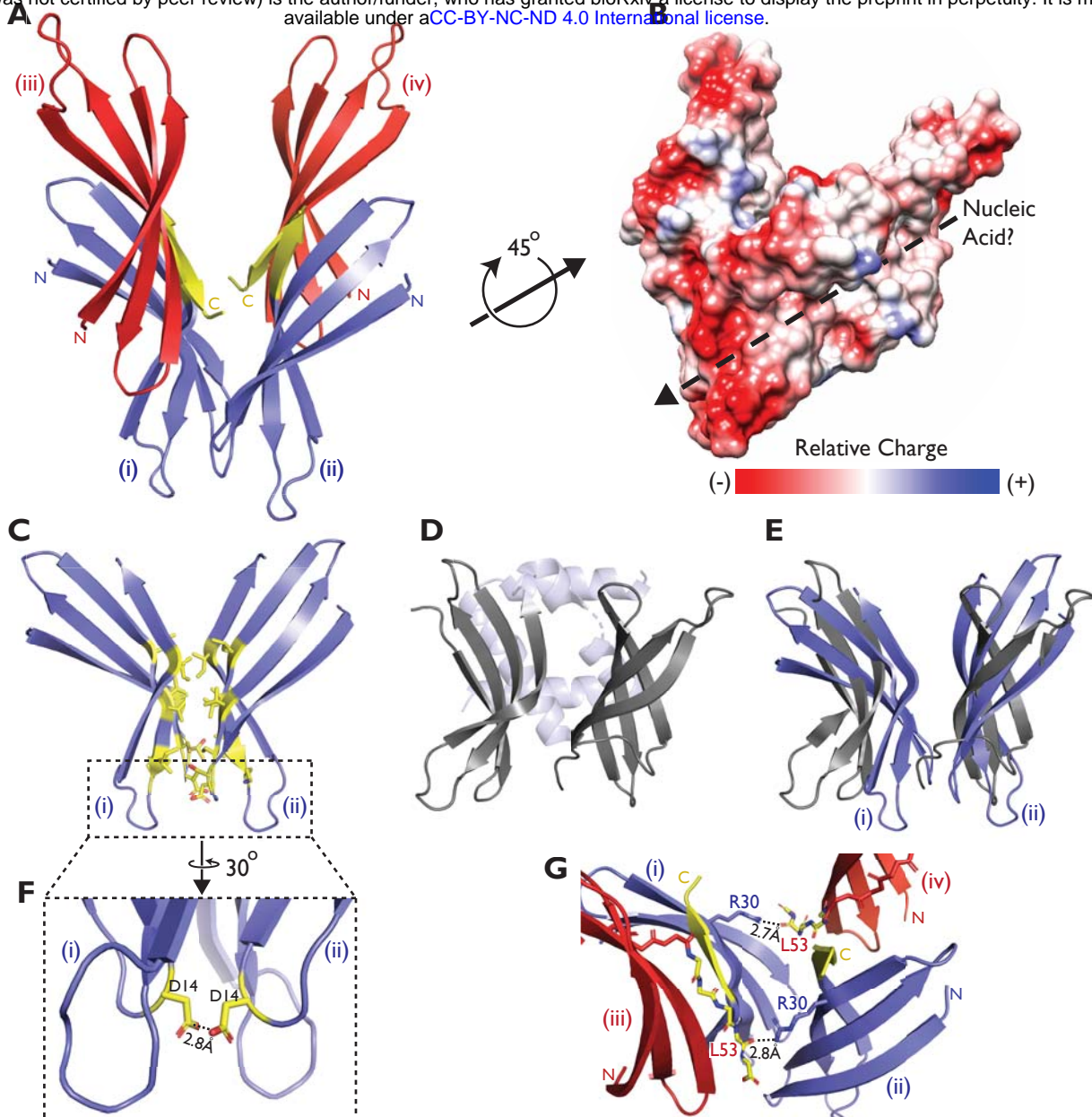


**Supplemental Figure 6. AcrlIA22 does not strongly bind SpyCas9.** SpyCas9 and sgRNA were pre-incubated before mixing with a twin-strep (TS) tagged AcrlIA22 or AcrlIA4. SpyCas9 without sgRNA was also used. Strep-Tactin pulldowns on AcrlIA4 also pulled down SpyCas9 pre-incubated with sgRNA, as previously reported<sup>12</sup>. Similar pulldowns with AcrlIA22 indicate little to no interaction with SpyCas9, regardless of whether sgRNA was used. These images depict total protein content visualized by Coomassie stain. Reaction components are indicated below the gel image. Asterisks (\*) and dagger (†) symbols indicate AcrlIA4 and AcrlIA22 protein bands that run at slightly different positions than expected due to gel distortion.

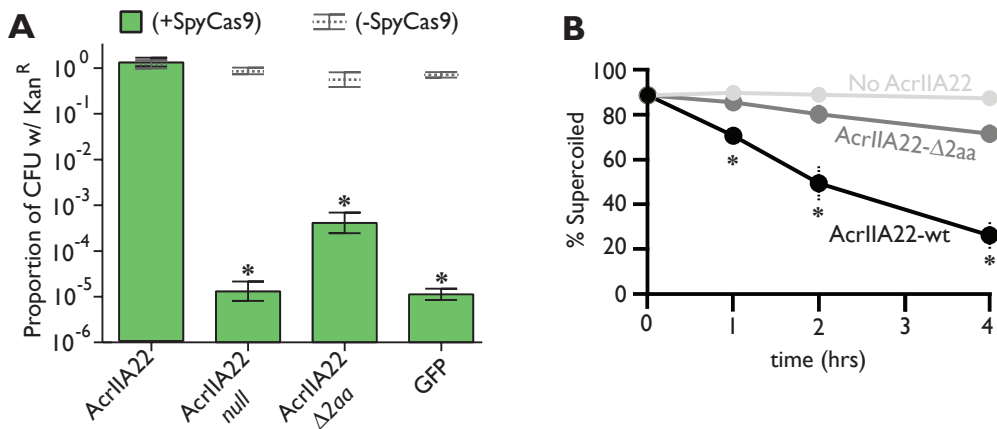


**Supplemental Figure 7. AcrIIA22 does not protect linear DNA from SpyCas9 cleavage. (A)**

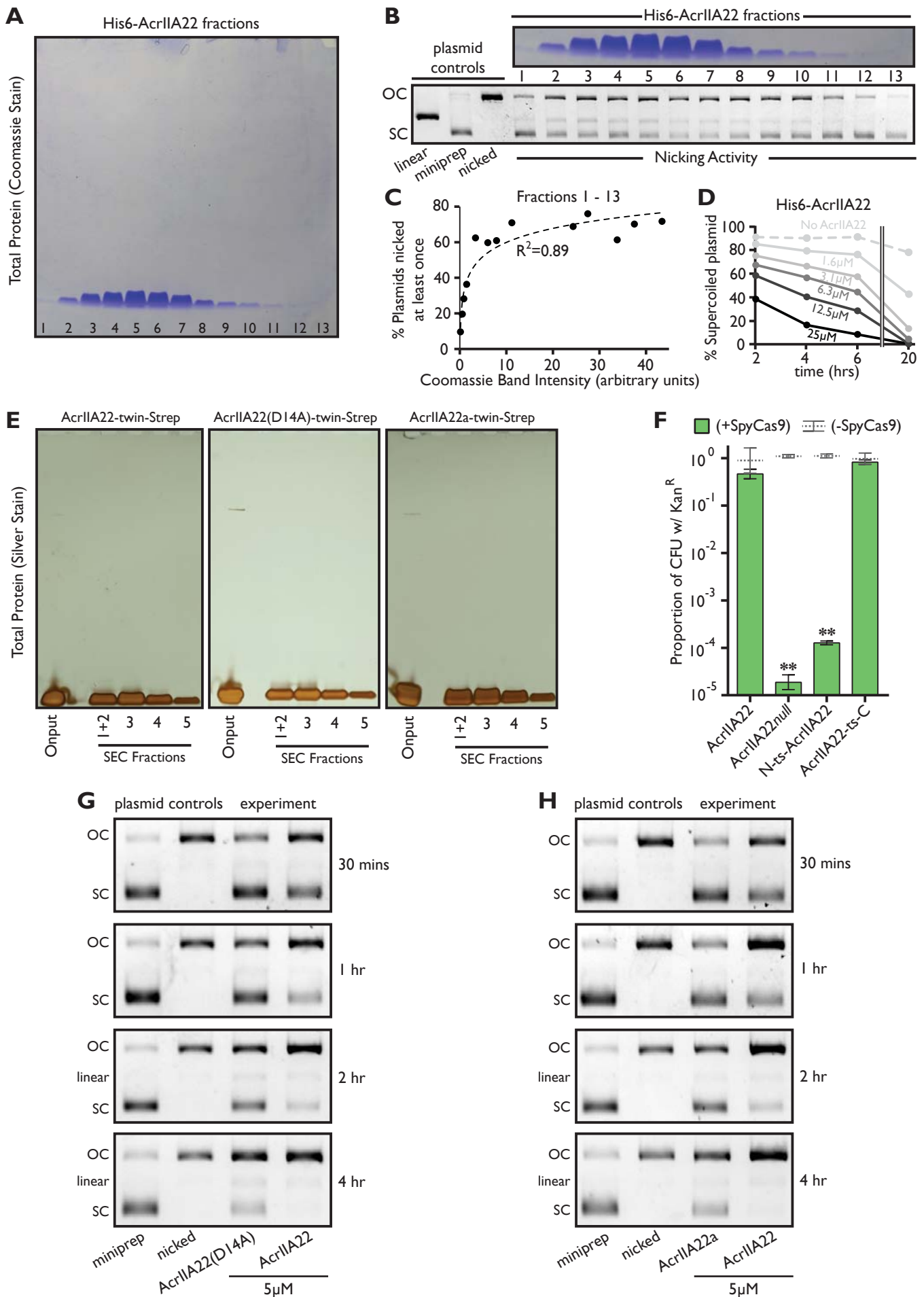
A schematic cartoon depicts the experiment in panel (B). SpyCas9 was pre-incubated with sgRNA targeting linear DNA. Then, Acr candidates were added. Subsequently, cleavage reactions were performed, and the DNA products visualized by gel electrophoresis. (B) We show the products of the reactions described in panel A for the inhibitors AcrIIA22 and AcrIIA4. SpyCas9 activity is greatly inhibited by AcrIIA4 but unaffected by AcrIIA22, as indicated by the proportion of cleaved DNA product. Reaction components are depicted atop the gel image, with molar equivalents relative to SpyCas9 indicated. The percent of DNA substrate cleaved by SpyCas9 is quantified below each lane. (C) We perform a similar experiment as in panel A, except candidate Acrs were incubated with SpyCas9 before sgRNA addition. Reactions were begun via the simultaneous addition of sgRNA and linear dsDNA instead of just dsDNA. (D) The products of the reactions described in panel C for AcrIIA22 and AcrIIA4 inhibitors are shown. SpyCas9 activity is inhibited by AcrIIA4 but unaffected by AcrIIA22, as indicated by the proportion of cleaved DNA product. The data depicted in this figure are not directly comparable to those in figure 7, due to methodological differences and because the preparations of SpyCas9 used in each experiment exhibited different activities.



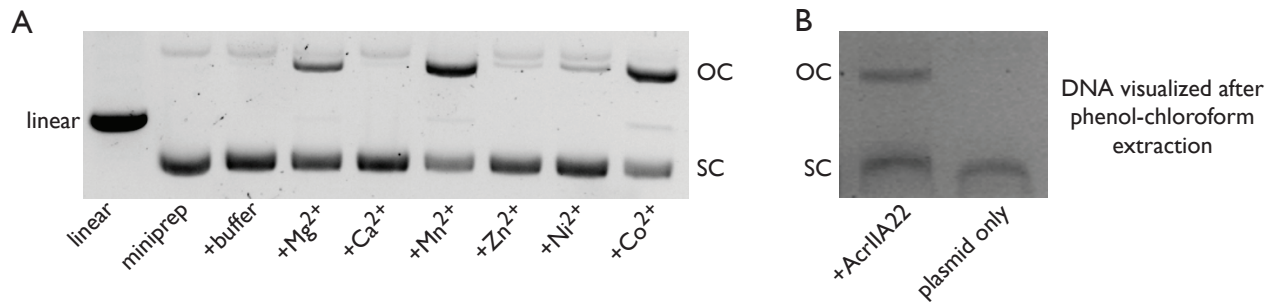
**Supplemental Figure 8. AcrIIA22 resembles a PC4-like protein.** (A) We present a ribbon diagram of a proposed AcrIIA22 tetramer, which requires binding between anti-parallel  $\beta$ -strands at the C-termini of AcrIIA22 monomers to form extended, concave  $\beta$ -sheets. This putative oligomerization interface is indicated by the regions highlighted in yellow. Each monomer in the proposed tetramer is labeled with lower-case Roman numerals (i-iv). (B) Space filling model of the tetrameric AcrIIA22 structure from panel A, with relative charge depicted, highlighting a groove (dashed line with arrowhead) that may accommodate nucleic acids (based on analogy to other PC4-like proteins). (C) AcrIIA22 monomers (i) and (ii) from the tetramer in panel A likely interact via a series of hydrophobic interactions, as indicated by the predominantly non-polar sidechains colored in yellow. The boxed region highlights residue D14, which is important for nicking activity and plasmid protection against SpyCas9, and is enlarged in panel F. (D) In conventional PC4-like family proteins, such as the putative single-stranded DNA binding protein from phage T5 depicted in gray (PDB:4BG7), the same topology of outward facing, concave  $\beta$ -sheets are instead stabilized via interactions between opposing  $\alpha$ -helices (depicted in opaque light blue). (E) An overlay of  $\beta$ -sheets from AcrIIA22 (blue, PDB:7JTA) and the phage T5 PC4-like protein (gray, PDB:4BG7) illustrates their similar topologies. (F) Two D14 residues in loop regions of AcrIIA22 monomers (i) and (ii) are in close proximity. These residues are important for nicking activity and may bind divalent cations in cells under physiological pH. (G) A close view of a putative salt bridge between R30 of monomers (i) / (ii) and the peptide backbone of the C-terminus of monomers (iv) / (iii), respectively. AcrIIA22 monomers are colored as described in panel A.



**Supplemental Figure 9. A 2-aa truncation mutant of AcrIIA22 is impaired for SpyCas9 inhibition and nicking activity.** (A) An *in vivo* plasmid protection assay. Asterisks depict statistically significant differences in plasmid retention under SpyCas9-inducing conditions with either wild-type AcrIIA22, a null mutant with an early stop codon, a 2-aa truncation, or a negative control *gfp* gene (adj.  $p < 0.005$ , Student's t-test,  $n=3$ ). The truncation mutant retains mild but severely impaired activity, as it protects a plasmid from SpyCas9 more effectively than a null mutant ( $p = 0.012$ ) or GFP control ( $p = 0.015$ ). All  $p$ -values were corrected for multiple hypotheses using Bonferroni's method. (B) The 2-aa truncation mutant is impaired for nicking *in vitro*, relative to wild-type AcrIIA22. In both cases, 25 $\mu$ M of protein was used following NiNTA-based purification of an N-terminal, His6-tagged construct. An asterisk (\*) denotes significant differences between AcrIIA22-treated and untreated substrates (Student's t-test,  $p < 0.05$ ,  $n=3$ ). Standard deviations are indicated by dashed lines (in most cases, the data points obscure these error bars).



**Supplemental Figure 10. AcrlIA22 nicks supercoiled plasmids.** **(A)** A Coomassie stain of an N-terminally His6-tagged AcrlIA22 construct shows no co-purifying proteins. **(B)** The nicking activity for this protein preparation (bottom) correlates with the intensity of the Coomassie-stained protein band across purification fractions (top). In each lane, supercoiled (SC) plasmid DNA represents the un-nicked fraction whereas open circle (OC) and linear DNA have been nicked at least once. **(C)** This panel is a quantification of the experiment depicted in panel B across all 13 fractions collected. **(D)** His6-AcrlIA22 nicks supercoiled plasmids in a time and concentration dependent manner. A decrease in the proportion of supercoiled plasmid DNA indicates nicking activity, as depicted in Figure 5B. **(E)** A silver stain of a C-terminally twin-strep-tagged AcrlIA22 construct shows no co-purifying proteins. Equal volumes of each protein fraction were loaded in each lane, for all samples. Fraction 4 was concentrated and used for all *in vitro* experiments. **(F)** A C-terminal, but not N-terminal twin-strep tag is compatible with AcrlIA22's ability to protect a target plasmid from SpyCas9 elimination *in vivo*. Statistically significant differences in plasmid retention between SpyCas9-inducing and non-inducing conditions were determined via a Student's t-test (n=3); \*\* indicates  $p \leq 0.001$ . All p-values were adjusted for multiple hypotheses using the Bonferroni correction. **(G)** The D14A mutation in AcrlIA22 impairs nicking activity. Over time, the wild-type AcrlIA22-twin-strep construct consistently converts a higher fraction of plasmid DNA from its supercoiled (SC) form to an open-circle (OC) conformation than a D14A mutant. Control plasmids include a miniprepped sample and sample pre-treated with the commercial nickase, Nb.BssSI. Reaction times are indicated to the right of each image. **(H)** AcrlIA22a (Figure 3B) is impaired for nicking activity relative to AcrlIA22. As in panel G, both constructs were purified via C-terminal twin-strep tags.



**Supplemental Figure 11. Divalent cations influence AcrIIA22's nicking activity.** **(A)** We present the impact of different divalent cations on AcrIIA22's nicking activity, which is highest with Mg<sup>2+</sup>, Mn<sup>2+</sup>, and Co<sup>2+</sup>. OC, open-circle plasmid form. SC, supercoiled plasmid. **(B)** The open-circle plasmid product persists through phenol-chloroform extraction following AcrIIA22 treatment, indicating that it directly results from AcrIIA22's nicking activity.

**Supplemental Table 1.** Whether all known anti-CRISPRs can bind Cas proteins or inhibit their cleavage activity as purified proteins.

Acr	Binds cognate Cas protein?	Inhibit as pure proteins?	References
AcrIIA1	Yes	No	(Osuna et al., 2020)
AcrIIA2	Yes	Yes	(Jiang et al., 2019; Liu et al., 2019)
AcrIIA3	unknown	unknown	(Rauch et al., 2017)
AcrIIA4	Yes	Yes	(Dong et al., 2017; Shin et al., 2017; Yang and Patel, 2017)
AcrIIA5	Yes	Yes	(An et al., 2020; Garcia et al., 2019; Song et al., 2019)
AcrIIA6	Yes	Yes	(Fuchsbaier et al., 2019)
AcrIIA7	No	Yes	(Uribe et al., 2019)
AcrIIA8	Yes	Yes	(Uribe et al., 2019)
AcrIIA9	Yes	Yes	(Uribe et al., 2019)
AcrIIA10	Yes	Yes	(Uribe et al., 2019)
AcrIIA11	Yes	Yes	(Forsberg et al., 2019)
AcrIIA12	probable	Yes	(Eitzinger et al., 2020; Osuna et al., 2020)
AcrIIA13	unknown	Yes	(Watters et al., 2020)
AcrIIA14	unknown	Yes	(Watters et al., 2020)
AcrIIA15	unknown	Yes	(Watters et al., 2020)
AcrIIA16	Yes	Yes	(Mahendra et al., 2020)
AcrIIA17	Yes	No	(Mahendra et al., 2020)
AcrIIA18	Yes	No	(Mahendra et al., 2020)
AcrIIA19	Yes	No	(Mahendra et al., 2020)
AcrIIA20	unknown	Yes	(Eitzinger et al., 2020)
AcrIIA21	unknown	Yes	(Eitzinger et al., 2020)
<b>AcrIIA22</b>	<b>No</b>	<b>No</b>	<b>This study</b>
AcrIIA23	unknown	unknown	(Varble et al., 2020)
AcrIIC1	Yes	Yes	(Pawluk et al., 2016)
AcrIIC2	Yes	Yes	(Pawluk et al., 2016)
AcrIIC3	Yes	Yes	(Pawluk et al., 2016)
AcrIIC4	Yes	Yes	(Lee et al., 2018)
AcrIIC5	Yes	Yes	(Lee et al., 2018)
AcrVA1	Yes	Yes	(Knott et al., 2019b; Watters et al., 2018; Zhang et al., 2019)
AcrVA2	unknown	unknown	(Marino et al., 2018)
AcrVA3	unknown	unknown	(Marino et al., 2018)

AcrVA4	Yes	Yes	(Knott et al., 2019a; Knott et al., 2019b; Watters et al., 2018; Zhang et al., 2019)
AcrVA5	transiently	Yes	(Knott et al., 2019b; Watters et al., 2018; Zhang et al., 2019)
AcrVIA1(Lse)	Yes	Yes	(Meeske et al., 2020)
AcrVIA1(Lwa)	Yes	unknown	(Lin et al., 2020)
AcrVIA2	Yes	unknown	(Lin et al., 2020)
AcrVIA3	Yes	unknown	(Lin et al., 2020)
AcrVIA4	Yes	unknown	(Lin et al., 2020)
AcrVIA5	Yes	unknown	(Lin et al., 2020)
AcrVIA6	Yes	unknown	(Lin et al., 2020)
AcrVIA7	unknown	unknown	(Lin et al., 2020)
AcrlB1	unknown	unknown	(Lin et al., 2020)
AcrlC1	unknown	unknown	(Leon et al., 2020)
AcrlC2	probable	unknown	(Leon et al., 2020)
AcrlC3	unknown	unknown	(Leon et al., 2020)
AcrlC4	probable	unknown	(Leon et al., 2020)
AcrlC5	probable	unknown	(Leon et al., 2020)
AcrlC6	unknown	unknown	(Leon et al., 2020)
AcrlC7	probable	unknown	(Leon et al., 2020)
AcrlC8	probable	unknown	(Leon et al., 2020)
AcrlD1	Yes	unknown	(He et al., 2018)
AcrlE1	Yes	unknown	(Pawluk et al., 2017)
AcrlE2	unknown	unknown	(Pawluk et al., 2014)
AcrlE3	probable	unknown	(Stanley, 2018)
AcrlE4	unknown	unknown	(Pawluk et al., 2014)
AcrlE5	unknown	unknown	(Pawluk et al., 2014)
AcrlE6	unknown	unknown	(Pawluk et al., 2014)
AcrlE7	unknown	unknown	(Pawluk et al., 2014)
AcrlE4-IF7	unknown	unknown	(Marino et al., 2018)
AcrlE8	unknown	unknown	(Pinilla-Redondo et al., 2020)
AcrlF1	Yes	unknown	(Bondy-Denomy et al., 2015; Chowdhury et al., 2017; Guo et al., 2017)
AcrlF2	Yes	unknown	(Bondy-Denomy et al., 2015; Chowdhury et al., 2017; Guo et al., 2017)
AcrlF3	Yes	unknown	(Bondy-Denomy et al., 2015; Wang et al., 2016a; Wang et al., 2016b)
AcrlF4	Yes	unknown	(Bondy-Denomy et al., 2015)
AcrlF5	unknown	unknown	(Bondy-Denomy et al., 2013)

AcrlF6	Yes	Yes	(Zhang et al., 2020)
AcrlF7	Yes	unknown	(Hirschi et al., 2020)
AcrlF8	Yes	Yes	(Zhang et al., 2020)
AcrlF9	Yes	Yes	(Hirschi et al., 2020; Zhang et al., 2020)
AcrlF10	Yes	unknown	(Guo et al., 2017)
AcrlF11	unknown	unknown	(Marino et al., 2018)
AcrlF12	unknown	unknown	(Marino et al., 2018)
AcrlF13	unknown	unknown	(Marino et al., 2018)
AcrlF14	unknown	unknown	(Marino et al., 2018)
AcrlF15	probable	unknown	(Pinilla-Redondo et al., 2020)
AcrlF16	unknown	unknown	(Pinilla-Redondo et al., 2020)
AcrlF17	unknown	unknown	(Pinilla-Redondo et al., 2020)
AcrlF18	probable	unknown	(Pinilla-Redondo et al., 2020)
AcrlF19	unknown	unknown	(Pinilla-Redondo et al., 2020)
AcrlF20	unknown	unknown	(Pinilla-Redondo et al., 2020)
AcrlF21	unknown	unknown	(Pinilla-Redondo et al., 2020)
AcrlF22	unknown	unknown	(Pinilla-Redondo et al., 2020)
AcrlF23	unknown	unknown	(Pinilla-Redondo et al., 2020)
AcrlF24	unknown	unknown	(Pinilla-Redondo et al., 2020)
AcrlII-1	No (degrades CA4 second messenger)	No	(Athukoralage et al., 2020)
AcrlIIB1	Yes	unknown	(Bhoobalan-Chitty et al., 2019)

**Supplemental Table 2.** PC4-like proteins with structural homology to AcrIIA22

Structural Homolog		Function	Similarity to AcrIIA22			
PDBID	Name	DNA/RNA Binding*	Zscore	r.m.s.d.	n-align	% A.A. ID
4bg7	PC4 putative transcriptional coactivator p15	DNA	6.2	2.5	54	15
3k44	<i>D. melanogaster</i> Pur- $\alpha$	DNA/RNA	5.9	2.6	47	9
5fgp	Pur- $\alpha$ repeat I and II from <i>D. melanogaster</i>	DNA/RNA	5.6	2.1	48	8
3n8b	Pur- $\alpha$ from <i>B. burgdorferi</i>	DNA/RNA	5	2.8	48	6
2gje	Mitochondrial RNA Binding Protein ( <i>T. brucei</i> )	RNA	4.9	2.5	52	8
5zkl	Protein of unknown function SP_0782, <i>S. pneumoniae</i>	DNA	4.7	3.6	52	12
5fg0	<i>D. melanogaster</i> Pur- $\alpha$ repeat III	No info	4.5	2.7	44	14
1pcf	Replication & transcription cofactor PC4 CTD	DNA	4.5	2.5	45	7
2ltt	Putative Uncharacterized Protein YDBC	DNA	4.5	2.8	50	12
4bhm	MoSub1-DNA PC4 transcription cofactor	DNA	3.9	2.8	45	4
3cm1	SSGA-like sporulation specific cell division protein	No info	2.8	3.7	47	13
1l3a	Transcription factor PBF-2 (P24, WHY1)	DNA	2.8	5	48	8
4ntq	Anti-toxin Cdil, <i>E. cloacae</i>	No info	2.7	3	49	12
3n1k	WHY2 transcription factor, <i>S. tuberosum</i>	DNA	2.6	2.8	52	4

\*RNA/DNA binding data from (Janowski and Niessing, 2020).

**Supplemental Table 3.** All sequences used in this study. Sequence names and databases are indicated. All sequences and annotations are also available as supplemental data. Sequences retrieved from Pasolli *et al.* refer to the following study: (Pasolli *et al.*, 2019).

Contig No.	Sequence Name	How Used?	NCBI Nuc. ID	Pasolli et al SGB?	Pasolli et al Raw Assembly?	Pasolli Reconstructed Genome Name	SGB id	GTDB Taxonomy	External Data Available at:
1	4303_LiJ_2014__V1.UC63-0_bin.67_NODE_112_length_95405_cov_4.60675	Figure 2, find gene functions from 54 unique genomic loci; Figure 3 Acr Seq	n/a	Yes	No	LiJ_2014__V1.UC63-0_bin.67	4303	d_Bacteria; p_Firmicutes_A; c_Clostridia; o_Oscillospirales; f_Acutalibacteraceae; g_CAG-217	<a href="http://segatalab.cibio.unitn.it/data/Pasolli_et_al.html">http://segatalab.cibio.unitn.it/data/Pasolli_et_al.html</a>
2	Bengtsson-PalmeJ_2015_TRAVELRE_S9_NODE_4_length_538580_cov_9.43148	find gene functions from 54 unique genomic loci	n/a	No	Yes	n/a	n/a	d_Bacteria; p_Firmicutes_A; c_Clostridia; o_Oscillospirales; f_Acutalibacteraceae; g_CAG-217 (inferred)	<a href="http://segatalab.cibio.unitn.it/data/Pasolli_et_al.html">http://segatalab.cibio.unitn.it/data/Pasolli_et_al.html</a>
3	ChengpingW_2017_AS9raw_NODE_922_length_27664_cov_3.49089	find gene functions from 54 unique genomic loci	n/a	No	Yes	n/a	n/a	d_Bacteria; p_Firmicutes_A; c_Clostridia; o_Oscillospirales; f_Acutalibacteraceae; g_CAG-217 (inferred)	<a href="http://segatalab.cibio.unitn.it/data/Pasolli_et_al.html">http://segatalab.cibio.unitn.it/data/Pasolli_et_al.html</a>
4	CosteaPI_2017_SID713B0_25-11-0-0_NODE_4_length_351620_cov_7.46108	find gene functions from 54 unique genomic loci	n/a	No	Yes	n/a	n/a	d_Bacteria; p_Firmicutes_A; c_Clostridia; o_Oscillospirales; f_Acutalibacteraceae; g_CAG-217 (inferred)	<a href="http://segatalab.cibio.unitn.it/data/Pasolli_et_al.html">http://segatalab.cibio.unitn.it/data/Pasolli_et_al.html</a>
5	BritoLL_2016_M1.64.ST_NODE_47_length_140472_cov_9.49805	find gene functions from 54 unique genomic loci; Figure 3 Acr Seq	n/a	No	Yes	n/a	n/a	d_Bacteria; p_Firmicutes_A; c_Clostridia; o_Oscillospirales; f_Acutalibacteraceae; g_CAG-217 (inferred)	<a href="http://segatalab.cibio.unitn.it/data/Pasolli_et_al.html">http://segatalab.cibio.unitn.it/data/Pasolli_et_al.html</a>
6	BritoLL_2016_M2.57.ST_NODE_3_length_405636_cov_14.0428	find gene functions from 54 unique genomic loci	n/a	No	Yes	n/a	n/a	d_Bacteria; p_Firmicutes_A; c_Clostridia; o_Oscillospirales; f_Acutalibacteraceae; g_CAG-217 (inferred)	<a href="http://segatalab.cibio.unitn.it/data/Pasolli_et_al.html">http://segatalab.cibio.unitn.it/data/Pasolli_et_al.html</a>
7	BritoLL_2016_WL.14.ST_NODE_13_length_259523_cov_10.8408	find gene functions from 54 unique genomic loci	n/a	No	Yes	n/a	n/a	d_Bacteria; p_Firmicutes_A; c_Clostridia; o_Oscillospirales; f_Acutalibacteraceae; g_CAG-217 (inferred)	<a href="http://segatalab.cibio.unitn.it/data/Pasolli_et_al.html">http://segatalab.cibio.unitn.it/data/Pasolli_et_al.html</a>
8	ChengpingW_2017_AS67raw_NODE_2_length_439177_cov_9.00174	Figure 2, find gene functions from 54 unique genomic loci; Figure 3 Acr Seq	n/a	No	Yes	n/a	n/a	d_Bacteria; p_Firmicutes_A; c_Clostridia; o_Oscillospirales; f_Acutalibacteraceae; g_CAG-217 (inferred)	<a href="http://segatalab.cibio.unitn.it/data/Pasolli_et_al.html">http://segatalab.cibio.unitn.it/data/Pasolli_et_al.html</a>
9	CM_madagascar_A90_04_1FE_NODE_125_length_81453_cov_9.00904	find gene functions from 54 unique genomic loci	n/a	No	Yes	n/a	n/a	d_Bacteria; p_Firmicutes_A; c_Clostridia; o_Oscillospirales; f_Acutalibacteraceae; g_CAG-217 (inferred)	<a href="http://segatalab.cibio.unitn.it/data/Pasolli_et_al.html">http://segatalab.cibio.unitn.it/data/Pasolli_et_al.html</a>
10	CM_madagascar_V12_01_2FE_NODE_5_length_202628_cov_9.50435	find gene functions from 54 unique genomic loci	n/a	No	Yes	n/a	n/a	d_Bacteria; p_Firmicutes_A; c_Clostridia; o_Oscillospirales; f_Acutalibacteraceae; g_CAG-217 (inferred)	<a href="http://segatalab.cibio.unitn.it/data/Pasolli_et_al.html">http://segatalab.cibio.unitn.it/data/Pasolli_et_al.html</a>
11	CosteaPI_2017_SID713A0_46-11-0-0_NODE_322_length_69000_cov_4.32987	find gene functions from 54 unique genomic loci; Figure 3 Acr Seq	n/a	No	Yes	n/a	n/a	d_Bacteria; p_Firmicutes_A; c_Clostridia; o_Oscillospirales; f_Acutalibacteraceae; g_CAG-217 (inferred)	<a href="http://segatalab.cibio.unitn.it/data/Pasolli_et_al.html">http://segatalab.cibio.unitn.it/data/Pasolli_et_al.html</a>
12	CosteaPI_2017_SID713A0_45-11-0-0_NODE_78_length_64886_cov_3.97493	find gene functions from 54 unique genomic loci	n/a	No	Yes	n/a	n/a	d_Bacteria; p_Firmicutes_A; c_Clostridia; o_Oscillospirales; f_Acutalibacteraceae; g_CAG-217 (inferred)	<a href="http://segatalab.cibio.unitn.it/data/Pasolli_et_al.html">http://segatalab.cibio.unitn.it/data/Pasolli_et_al.html</a>
13	CosteaPI_2017_SID713A0_04-11-0-0_NODE_1_length_647860_cov_14.1013	find gene functions from 54 unique genomic loci; Figure 3 Acr Seq	n/a	No	Yes	n/a	n/a	d_Bacteria; p_Firmicutes_A; c_Clostridia; o_Oscillospirales; f_Acutalibacteraceae; g_CAG-217 (inferred)	<a href="http://segatalab.cibio.unitn.it/data/Pasolli_et_al.html">http://segatalab.cibio.unitn.it/data/Pasolli_et_al.html</a>
14	CosteaPI_2017_peacemaker-11-60-	find gene functions from 54 unique genomic loci	n/a	No	Yes	n/a	n/a	d_Bacteria; p_Firmicutes_A; c_Clostridia; o_Oscillospirales; f_Acutalibacteraceae; g_CAG-217 (inferred)	<a href="http://segatalab.cibio.unitn.it/data/Pasolli_et_al.html">http://segatalab.cibio.unitn.it/data/Pasolli_et_al.html</a>

	0_NODE_48_length_49378_cov_15.5445							
15	CosteaPI_2017_SID713A0_63-11-90-0_NODE_2082_length_169_60_cov_2.98527	find gene functions from 54 unique genomic loci	n/a	No	Yes	n/a	n/a	d_Bacteria; p_Firmicutes_A; c_Clostridia; o_Oscillospirales; f_Acutalibacteraceae; g_CAG-217 (inferred)
16	CosteaPI_2017_SID713A0_88-11-0-0_NODE_89_length_11329_7_cov_5.77445	find gene functions from 54 unique genomic loci; Figure 3 Acr Seq	n/a	No	Yes	n/a	n/a	d_Bacteria; p_Firmicutes_A; c_Clostridia; o_Oscillospirales; f_Acutalibacteraceae; g_CAG-217 (inferred)
17	CosteaPI_2017_SID713A0_62-11-0-0_NODE_38_length_19219_6_cov_4.03099	Find gene functions from 54 unique genomic loci	n/a	No	Yes	n/a	n/a	d_Bacteria; p_Firmicutes_A; c_Clostridia; o_Oscillospirales; f_Acutalibacteraceae; g_CAG-217 (inferred)
18	CosteaPI_2017_SID713B0_51-11-0-0_NODE_14_length_29861_9_cov_7.20988	find gene functions from 54 unique genomic loci	n/a	No	Yes	n/a	n/a	d_Bacteria; p_Firmicutes_A; c_Clostridia; o_Oscillospirales; f_Acutalibacteraceae; g_CAG-217 (inferred)
19	FengQ_2015_SID31872_NODE_2_length_392843_cov_5.93617	find gene functions from 54 unique genomic loci	n/a	No	Yes	n/a	n/a	d_Bacteria; p_Firmicutes_A; c_Clostridia; o_Oscillospirales; f_Acutalibacteraceae; g_CAG-217 (inferred)
20	FengQ_2015_SID530258_NODE_5_length_350476_cov_17.595	find gene functions from 54 unique genomic loci; Figure 3 Acr Seq	n/a	No	Yes	n/a	n/a	d_Bacteria; p_Firmicutes_A; c_Clostridia; o_Oscillospirales; f_Acutalibacteraceae; g_CAG-217 (inferred)
21	FengQ_2015_SID530373_NODE_21_length_272157_cov_9.73468	find gene functions from 54 unique genomic loci	n/a	No	Yes	n/a	n/a	d_Bacteria; p_Firmicutes_A; c_Clostridia; o_Oscillospirales; f_Acutalibacteraceae; g_CAG-217 (inferred)
22	HeQ_2017_SZAXPI02956_1-52_NODE_1_length_50275_2_cov_8.09488	find gene functions from 54 unique genomic loci; Figure 3 Acr Seq	n/a	No	Yes	n/a	n/a	d_Bacteria; p_Firmicutes_A; c_Clostridia; o_Oscillospirales; f_Acutalibacteraceae; g_CAG-217 (inferred)
23	HeQ_2017_SZAXPI02957_5-90_NODE_229_length_949_18_cov_3.79903	find gene functions from 54 unique genomic loci	n/a	No	Yes	n/a	n/a	d_Bacteria; p_Firmicutes_A; c_Clostridia; o_Oscillospirales; f_Acutalibacteraceae; g_CAG-217 (inferred)
24	KarlssonFH_2013_S463_NODE_1_length_570037_cov_16.3973	Figure 2, find gene functions from 54 unique genomic loci	n/a	No	Yes	n/a	n/a	d_Bacteria; p_Firmicutes_A; c_Clostridia; o_Oscillospirales; f_Acutalibacteraceae; g_CAG-217 (inferred)
25	LiJ_2014_O2.UC12-1_NODE_323_length_4999_5_cov_5.04395	find gene functions from 54 unique genomic loci	n/a	No	Yes	n/a	n/a	d_Bacteria; p_Firmicutes_A; c_Clostridia; o_Oscillospirales; f_Acutalibacteraceae; g_CAG-217 (inferred)
26	LiJ_2014_V1.FI02_NODE_274_length_84286_cov_3.4_9253	find gene functions from 54 unique genomic loci	n/a	No	Yes	n/a	n/a	d_Bacteria; p_Firmicutes_A; c_Clostridia; o_Oscillospirales; f_Acutalibacteraceae; g_CAG-217 (inferred)
27	LiJ_2017_H1M413815_NO DE_71_length_81514_cov_18.301	find gene functions from 54 unique genomic loci	n/a	No	Yes	n/a	n/a	d_Bacteria; p_Firmicutes_A; c_Clostridia; o_Oscillospirales; f_Acutalibacteraceae; g_CAG-217 (inferred)
28	LiJ_2017_H2M514909_NO DE_68_length_69076_cov_10.283	find gene functions from 54 unique genomic loci	n/a	No	Yes	n/a	n/a	d_Bacteria; p_Firmicutes_A; c_Clostridia; o_Oscillospirales; f_Acutalibacteraceae; g_CAG-217 (inferred)
29	LiuW_2016_SRR3992969_NODE_1149_length_1899_9_cov_8.45033	find gene functions from 54 unique genomic loci; Figure 3 Acr Seq	n/a	No	Yes	n/a	n/a	d_Bacteria; p_Firmicutes_A; c_Clostridia; o_Oscillospirales; f_Acutalibacteraceae; g_CAG-217 (inferred)

30	LiuW_2016_SRR3992984_NODE_127_length_61384_cov_18.0593	find gene functions from 54 unique genomic loci	n/a	No	Yes	n/a	n/a	d_Bacteria; p_Firmicutes_A; c_Clostridia; o_Oscillospirales; f_Acutalibacteraceae; g_CAG-217 (inferred)	<a href="http://segatalab.cibio.unitn.it/data/Pasolli_et_al.html">http://segatalab.cibio.unitn.it/data/Pasolli_et_al.html</a>
31	LiuW_2016_SRR3993014_NODE_8_length_143441_cov_89.3981	find gene functions from 54 unique genomic loci	n/a	No	Yes	n/a	n/a	d_Bacteria; p_Firmicutes_A; c_Clostridia; o_Oscillospirales; f_Acutalibacteraceae; g_CAG-217 (inferred)	<a href="http://segatalab.cibio.unitn.it/data/Pasolli_et_al.html">http://segatalab.cibio.unitn.it/data/Pasolli_et_al.html</a>
32	QinJ_2012_NOM001_NO_DE_179_length_28679_cov_2.87521	find gene functions from 54 unique genomic loci	n/a	No	Yes	n/a	n/a	d_Bacteria; p_Firmicutes_A; c_Clostridia; o_Oscillospirales; f_Acutalibacteraceae; g_CAG-217 (inferred)	<a href="http://segatalab.cibio.unitn.it/data/Pasolli_et_al.html">http://segatalab.cibio.unitn.it/data/Pasolli_et_al.html</a>
33	QinJ_2012_T2D-050_NODE_25_length_192_521_cov_10.1129	find gene functions from 54 unique genomic loci	n/a	No	Yes	n/a	n/a	d_Bacteria; p_Firmicutes_A; c_Clostridia; o_Oscillospirales; f_Acutalibacteraceae; g_CAG-217 (inferred)	<a href="http://segatalab.cibio.unitn.it/data/Pasolli_et_al.html">http://segatalab.cibio.unitn.it/data/Pasolli_et_al.html</a>
34	VatanenT_2016_G78791_NODE_43_length_22491_cov_6.98654	find gene functions from 54 unique genomic loci	n/a	No	Yes	n/a	n/a	d_Bacteria; p_Firmicutes_A; c_Clostridia; o_Oscillospirales; f_Acutalibacteraceae; g_CAG-217 (inferred)	<a href="http://segatalab.cibio.unitn.it/data/Pasolli_et_al.html">http://segatalab.cibio.unitn.it/data/Pasolli_et_al.html</a>
35	XieH_2016_YSZC12003_3_5392_NODE_87_length_19_6476_cov_13.3023	find gene functions from 54 unique genomic loci	n/a	No	Yes	n/a	n/a	d_Bacteria; p_Firmicutes_A; c_Clostridia; o_Oscillospirales; f_Acutalibacteraceae; g_CAG-217 (inferred)	<a href="http://segatalab.cibio.unitn.it/data/Pasolli_et_al.html">http://segatalab.cibio.unitn.it/data/Pasolli_et_al.html</a>
36	XieH_2016_YSZC12003_3_5563_NODE_11_length_35_3850_cov_18.1068	Figure 2, find gene functions from 54 unique genomic loci	n/a	No	Yes	n/a	n/a	d_Bacteria; p_Firmicutes_A; c_Clostridia; o_Oscillospirales; f_Acutalibacteraceae; g_CAG-217 (inferred)	<a href="http://segatalab.cibio.unitn.it/data/Pasolli_et_al.html">http://segatalab.cibio.unitn.it/data/Pasolli_et_al.html</a>
37	XieH_2016_YSZC12003_3_6005_NODE_238_length_9_9923_cov_5.91259	Figure 2, find gene functions from 54 unique genomic loci, source of orf1-encoding phage genome; Figure 3 Acr Seq	n/a	No	Yes	n/a	n/a	d_Bacteria; p_Firmicutes_A; c_Clostridia; o_Oscillospirales; f_Acutalibacteraceae; g_CAG-217 (inferred)	<a href="http://segatalab.cibio.unitn.it/data/Pasolli_et_al.html">http://segatalab.cibio.unitn.it/data/Pasolli_et_al.html</a>
38	XieH_2016_YSZC12003_3_6794_NODE_1_length_781_521_cov_10.2961	find gene functions from 54 unique genomic loci, source of orf1-encoding phage genome; Figure 3 Acr Seq	n/a	No	Yes	n/a	n/a	d_Bacteria; p_Firmicutes_A; c_Clostridia; o_Oscillospirales; f_Acutalibacteraceae; g_CAG-217 (inferred)	<a href="http://segatalab.cibio.unitn.it/data/Pasolli_et_al.html">http://segatalab.cibio.unitn.it/data/Pasolli_et_al.html</a>
39	XieH_2016_YSZC12003_3_7133_NODE_3_length_676_817_cov_24.9073	find gene functions from 54 unique genomic loci	n/a	No	Yes	n/a	n/a	d_Bacteria; p_Firmicutes_A; c_Clostridia; o_Oscillospirales; f_Acutalibacteraceae; g_CAG-217 (inferred)	<a href="http://segatalab.cibio.unitn.it/data/Pasolli_et_al.html">http://segatalab.cibio.unitn.it/data/Pasolli_et_al.html</a>
40	XieH_2016_YSZC12003_3_7322_NODE_5_length_601_737_cov_115.712	find gene functions from 54 unique genomic loci	n/a	No	Yes	n/a	n/a	d_Bacteria; p_Firmicutes_A; c_Clostridia; o_Oscillospirales; f_Acutalibacteraceae; g_CAG-217 (inferred)	<a href="http://segatalab.cibio.unitn.it/data/Pasolli_et_al.html">http://segatalab.cibio.unitn.it/data/Pasolli_et_al.html</a>
41	XieH_2016_YSZC12003_3_7399_NODE_3_length_598_430_cov_49.9887	find gene functions from 54 unique genomic loci	n/a	No	Yes	n/a	n/a	d_Bacteria; p_Firmicutes_A; c_Clostridia; o_Oscillospirales; f_Acutalibacteraceae; g_CAG-217 (inferred)	<a href="http://segatalab.cibio.unitn.it/data/Pasolli_et_al.html">http://segatalab.cibio.unitn.it/data/Pasolli_et_al.html</a>
42	XieH_2016_YSZC12003_3_7878_NODE_8_length_402_183_cov_76.149	find gene functions from 54 unique genomic loci	n/a	No	Yes	n/a	n/a	d_Bacteria; p_Firmicutes_A; c_Clostridia; o_Oscillospirales; f_Acutalibacteraceae; g_CAG-217 (inferred)	<a href="http://segatalab.cibio.unitn.it/data/Pasolli_et_al.html">http://segatalab.cibio.unitn.it/data/Pasolli_et_al.html</a>
43	YuJ_2015_SZAXPI003435_11_NODE_1_length_77221_8_cov_11.5924	find gene functions from 54 unique genomic loci	n/a	No	Yes	n/a	n/a	d_Bacteria; p_Firmicutes_A; c_Clostridia; o_Oscillospirales; f_Acutalibacteraceae; g_CAG-217 (inferred)	<a href="http://segatalab.cibio.unitn.it/data/Pasolli_et_al.html">http://segatalab.cibio.unitn.it/data/Pasolli_et_al.html</a>
44	YuJ_2015_SZAXPI015230_16_NODE_32_length_1743_49_cov_17.3543	find gene functions from 54 unique genomic loci	n/a	No	Yes	n/a	n/a	d_Bacteria; p_Firmicutes_A; c_Clostridia; o_Oscillospirales; f_Acutalibacteraceae; g_CAG-217 (inferred)	<a href="http://segatalab.cibio.unitn.it/data/Pasolli_et_al.html">http://segatalab.cibio.unitn.it/data/Pasolli_et_al.html</a>
45	ZeeviD_2015_PNP_DietIntervention_11_NODE_16_le	find gene functions from 54 unique genomic loci	n/a	No	Yes	n/a	n/a	d_Bacteria; p_Firmicutes_A; c_Clostridia; o_Oscillospirales; f_Acutalibacteraceae; g_CAG-217 (inferred)	<a href="http://segatalab.cibio.unitn.it/data/Pasolli_et_al.html">http://segatalab.cibio.unitn.it/data/Pasolli_et_al.html</a>

	ngth_97163_cov_10.0000_I_D_22997								
46	ZeeviD_2015_PNP_Main_234_NODE_10_length_202229_cov_13.9987_ID_180729	find gene functions from 54 unique genomic loci	n/a	No	Yes	n/a	n/a	d_Bacteria; p_Firmicutes_A; c_Clostridia; o_Oscillospirales; f_Acutalibacteraceae; g_CAG-217 (inferred)	<a href="http://segatalab.cibio.unitn.it/data/Pasolli_et_al.html">http://segatalab.cibio.unitn.it/data/Pasolli_et_al.html</a>
47	ZeeviD_2015_PNP_Main_294_NODE_20_length_208110_cov_20.9981_ID_106095	find gene functions from 54 unique genomic loci	n/a	No	Yes	n/a	n/a	d_Bacteria; p_Firmicutes_A; c_Clostridia; o_Oscillospirales; f_Acutalibacteraceae; g_CAG-217 (inferred)	<a href="http://segatalab.cibio.unitn.it/data/Pasolli_et_al.html">http://segatalab.cibio.unitn.it/data/Pasolli_et_al.html</a>
48	ZeeviD_2015_PNP_Main_390_NODE_33_length_137723_cov_10.9985_ID_46475	find gene functions from 54 unique genomic loci	n/a	No	Yes	n/a	n/a	d_Bacteria; p_Firmicutes_A; c_Clostridia; o_Oscillospirales; f_Acutalibacteraceae; g_CAG-217 (inferred)	<a href="http://segatalab.cibio.unitn.it/data/Pasolli_et_al.html">http://segatalab.cibio.unitn.it/data/Pasolli_et_al.html</a>
49	ZeeviD_2015_PNP_Main_578_NODE_20_length_138741_cov_8.9988_ID_132563	find gene functions from 54 unique genomic loci	n/a	No	Yes	n/a	n/a	d_Bacteria; p_Firmicutes_A; c_Clostridia; o_Oscillospirales; f_Acutalibacteraceae; g_CAG-217 (inferred)	<a href="http://segatalab.cibio.unitn.it/data/Pasolli_et_al.html">http://segatalab.cibio.unitn.it/data/Pasolli_et_al.html</a>
50	ZeeviD_2015_PNP_Main_741_NODE_13_length_214417_cov_12.0572_ID_91679	find gene functions from 54 unique genomic loci	n/a	No	Yes	n/a	n/a	d_Bacteria; p_Firmicutes_A; c_Clostridia; o_Oscillospirales; f_Acutalibacteraceae; g_CAG-217 (inferred)	<a href="http://segatalab.cibio.unitn.it/data/Pasolli_et_al.html">http://segatalab.cibio.unitn.it/data/Pasolli_et_al.html</a>
51	ZellerG_2014_CCIS03857607ST-4-0_NODE_542_length_35291_cov_2.7674	find gene functions from 54 unique genomic loci	n/a	No	Yes	n/a	n/a	d_Bacteria; p_Firmicutes_A; c_Clostridia; o_Oscillospirales; f_Acutalibacteraceae; g_CAG-217 (inferred)	<a href="http://segatalab.cibio.unitn.it/data/Pasolli_et_al.html">http://segatalab.cibio.unitn.it/data/Pasolli_et_al.html</a>
52	ZellerG_2014_CCIS22958137ST-20-0_NODE_40_length_181493_cov_7.91373	find gene functions from 54 unique genomic loci, source of orf1-encoding phage genome; Figure 3 Acr Seq	n/a	No	Yes	n/a	n/a	d_Bacteria; p_Firmicutes_A; c_Clostridia; o_Oscillospirales; f_Acutalibacteraceae; g_CAG-217 (inferred)	<a href="http://segatalab.cibio.unitn.it/data/Pasolli_et_al.html">http://segatalab.cibio.unitn.it/data/Pasolli_et_al.html</a>
53	XieH_2016_YSCZC12003_35635_NODE_109_length_156568_cov_5.12141	find gene functions from 54 unique genomic loci	n/a	No	Yes	n/a	n/a	d_Bacteria; p_Firmicutes_A; c_Clostridia; o_Oscillospirales; f_Acutalibacteraceae; g_CAG-217 (inferred)	<a href="http://segatalab.cibio.unitn.it/data/Pasolli_et_al.html">http://segatalab.cibio.unitn.it/data/Pasolli_et_al.html</a>
54	ZeeviD_2015_PNP_Main_85_NODE_182_length_52997_cov_7.0000_ID_133080	find gene functions from 54 unique genomic loci	n/a	No	Yes	n/a	n/a	d_Bacteria; p_Firmicutes_A; c_Clostridia; o_Oscillospirales; f_Acutalibacteraceae; g_CAG-217 (inferred)	<a href="http://segatalab.cibio.unitn.it/data/Pasolli_et_al.html">http://segatalab.cibio.unitn.it/data/Pasolli_et_al.html</a>
55	4303_HeQ_2017_SZAXPI029570-85_bin.1_NODE_2_length_608092_cov_26.3259	Figure 2	n/a	Yes	No	HeQ_2017_S_ZAXPI029570-85_bin.1	4303	d_Bacteria; p_Firmicutes_A; c_Clostridia; o_Oscillospirales; f_Acutalibacteraceae; g_CAG-217	<a href="http://segatalab.cibio.unitn.it/data/Pasolli_et_al.html">http://segatalab.cibio.unitn.it/data/Pasolli_et_al.html</a>
56	4303_CosteaPI_2017_SID713B074-11-90-0_bin.57_NODE_18_length_238289_cov_5.37382	Source of orf1-encoding phage genome; Figure 3 Acr Seq	n/a	Yes	No	CosteaPI_2017_SID713B074-11-90-0_bin.57	4303	d_Bacteria; p_Firmicutes_A; c_Clostridia; o_Oscillospirales; f_Acutalibacteraceae; g_CAG-217	<a href="http://segatalab.cibio.unitn.it/data/Pasolli_et_al.html">http://segatalab.cibio.unitn.it/data/Pasolli_et_al.html</a>
57	Clostridiales_bacterium_isolate_CIM:MAG_317_1_contig_8085	Figure 2, source of orf1-encoding phage genome	QALM0100000.2.1	No	No	n/a	n/a	d_Bacteria; p_Firmicutes_A; c_Clostridia; o_Oscillospirales; f_Acutalibacteraceae; g_CAG-217 (inferred)	NCBI Genbank
58	TPA_asm:_Ruminococcaceae_bacterium_isolate_UBA8277_contig_226	Figure 3 Acr Seq	DPDR01000010.1	No	No	n/a	n/a	d_Bacteria; p_Firmicutes_A; c_Clostridia; o_Oscillospirales; f_Acutalibacteraceae; g_CAG-217 (inferred)	NCBI Genbank
59	KarlssonFH_2013_S424_NODE_2_length_526279_cov_9.22761	Source of orf1-encoding phage genome	n/a	No	Yes	n/a	n/a	d_Bacteria; p_Firmicutes_A; c_Clostridia; o_Oscillospirales; f_Acutalibacteraceae; g_CAG-217 (inferred)	<a href="http://segatalab.cibio.unitn.it/data/Pasolli_et_al.html">http://segatalab.cibio.unitn.it/data/Pasolli_et_al.html</a>

60	XieH_2016_YSCZ12003_3 6696_NODE_1_length_776 477_cov_39.8546	Source of orf1-encoding phage genome, AcrlIA17 encoding phage (figure S5)	n/a	No	Yes	n/a	n/a	d_Bacteria; p_Firmicutes_A; c_Clostridia; o_Oscillospirales; f_Acutalibacteraceae; g_CAG-217 (inferred)	<a href="http://segatalab.cibio.unitn.it/data/Pasolli_et_al.html">http://segatalab.cibio.unitn.it/data/Pasolli_et_al.html</a>
61	XieH_2016_YSCZ12003_3 7308R1_NODE_3_length_7 17276_cov_26.9646	source of orf1-encoding phage genome	n/a	No	Yes	n/a	n/a	d_Bacteria; p_Firmicutes_A; c_Clostridia; o_Oscillospirales; f_Acutalibacteraceae; g_CAG-217 (inferred)	<a href="http://segatalab.cibio.unitn.it/data/Pasolli_et_al.html">http://segatalab.cibio.unitn.it/data/Pasolli_et_al.html</a>
62	ZellerG_2014_CCIS88007 743ST-4-0_NODE_31_length_21091 0_cov_8.07406	source of orf1-encoding phage genome	n/a	No	Yes	n/a	n/a	d_Bacteria; p_Firmicutes_A; c_Clostridia; o_Oscillospirales; f_Acutalibacteraceae; g_CAG-217 (inferred)	<a href="http://segatalab.cibio.unitn.it/data/Pasolli_et_al.html">http://segatalab.cibio.unitn.it/data/Pasolli_et_al.html</a>
63	4303_QinN_2014_LD- 22_bin.75_NODE_22_length_329763_cov_10.7401	Figure 3 Acr Seq	n/a	Yes	No	QinN_2014_LD-22_bin.75	4303	d_Bacteria; p_Firmicutes_A; c_Clostridia; o_Oscillospirales; f_Acutalibacteraceae; g_CAG-217	<a href="http://segatalab.cibio.unitn.it/data/Pasolli_et_al.html">http://segatalab.cibio.unitn.it/data/Pasolli_et_al.html</a>
64	ZellerG_2014_CCMD2596 3797ST-21-0_NODE_9_length_356111 cov_10.1715	Figure 3 Acr Seq	n/a	No	Yes	n/a	n/a	d_Bacteria; p_Firmicutes_A; c_Clostridia; o_Oscillospirales; f_Acutalibacteraceae; g_CAG-217 (inferred)	<a href="http://segatalab.cibio.unitn.it/data/Pasolli_et_al.html">http://segatalab.cibio.unitn.it/data/Pasolli_et_al.html</a>
65	ZellerG_2014_CCIS41222 843ST-4-0_NODE_17_length_26713 3_cov_14.7383	Figure 3 Acr Seq	n/a	No	Yes	n/a	n/a	d_Bacteria; p_Firmicutes_A; c_Clostridia; o_Oscillospirales; f_Acutalibacteraceae; g_CAG-217 (inferred)	<a href="http://segatalab.cibio.unitn.it/data/Pasolli_et_al.html">http://segatalab.cibio.unitn.it/data/Pasolli_et_al.html</a>
66	FengQ_2015_SID530168_NODE_20_length_224404_cov_6.02914	Figure 3 Acr Seq	n/a	No	Yes	n/a	n/a	d_Bacteria; p_Firmicutes_A; c_Clostridia; o_Oscillospirales; f_Acutalibacteraceae; g_CAG-217 (inferred)	<a href="http://segatalab.cibio.unitn.it/data/Pasolli_et_al.html">http://segatalab.cibio.unitn.it/data/Pasolli_et_al.html</a>
67	FengQ_2015_SID530041_NODE_7_length_421742_cov_9.32571	Figure 3 Acr Seq	n/a	No	Yes	n/a	n/a	d_Bacteria; p_Firmicutes_A; c_Clostridia; o_Oscillospirales; f_Acutalibacteraceae; g_CAG-217 (inferred)	<a href="http://segatalab.cibio.unitn.it/data/Pasolli_et_al.html">http://segatalab.cibio.unitn.it/data/Pasolli_et_al.html</a>
68	FengQ_2015_SID31223_NODE_13_length_228767_cov_7.50553	Figure 3 Acr Seq	n/a	No	Yes	n/a	n/a	d_Bacteria; p_Firmicutes_A; c_Clostridia; o_Oscillospirales; f_Acutalibacteraceae; g_CAG-217 (inferred)	<a href="http://segatalab.cibio.unitn.it/data/Pasolli_et_al.html">http://segatalab.cibio.unitn.it/data/Pasolli_et_al.html</a>

**Supplemental Table 4.** Plasmids used in this study. Supplemental Table S5 indicates genes expressed from pZE21\_tetR.

Plasmid	crRNA promoter, sequence (5'-3')	Notes	Refs	Purpose
pZE21_tetR	n/a	Contains tetR behind pLac promoter for inducible expression of candidate Acrs. Targeted by crRNA_A; PAM = AGG.	(Forsberg et al., 2019)	Expressing genes to test <i>in vivo</i> anti-CRISPR activity
pSpyCas9_crA	pJ23100, GTTCATTCAAGGCAC CGGAC	Arabinose-inducible SpyCas9 with pZE21 targeting pZE21_tetR	(Forsberg et al., 2019)	Target pZE21_tetR for elimination with SpyCas9
pSpyCas9_crMu	pJ23100, GTAATACTTGTCGGC AAAG	Mu-targeting spacer for phage Mu immunity testing. Otherwise identical to pSpyCas9_crA	(Forsberg et al., 2019)	Phage Mu immunity testing
pSpyCa9_crNT	pJ23100, GAACGAAAAGCTGCG CCGGG	non-targeting spacer used as control. Otherwise identical to pSpyCas9_crA	(Forsberg et al., 2019)	Phage Mu immunity testing, Western blots
pCloDF13_GFP	pJ23100, GAACGAAAAGCTGCG CCGGG	eGFP gene replaces spyCas9 in pSpyCas9_crA		Measure generic protein expression from pSpyCas9 expression vector
pIDTsmart	n/a	Plasmid used for <i>in-vitro</i> SpyCas9 digestion. Sequence available at: <a href="https://www.idtdna.com/pages/products/genes-and-gene-fragments/custom-gene-synthesis">https://www.idtdna.com/pages/products/genes-and-gene-fragments/custom-gene-synthesis</a>		Plasmid template for <i>in-vitro</i> nuclease reactions
pET15b/HE	n/a	Novagen Cat. No. 69661-3; pET15 variants 'b' and 'HE' differ only by a few bases upstream of the N-terminal thrombin cut site		Protein purification
pSpyCas9_Fig3C	n/a	J23100 promoter expressing a theophylline inducible SpyCas9, used in Figure 3C	(Uribe et al., 2019)	Testing AcrlIA22 activity against a panel of Cas9 and Cas12 effector nucleases
pNmCas9_Fig3C	n/a	J23100 promoter expressing a theophylline inducible NmCas9, used in Figure 3C	(Uribe et al., 2019)	Testing AcrlIA22 activity against a panel of Cas9 and Cas12 effector nucleases
pLbCas12_Fig3C	n/a	J23100 promoter expressing a theophylline inducible LbCas12, used in Figure 3C	(Uribe et al., 2019)	Testing AcrlIA22 activity against a panel of Cas9 and Cas12 effector nucleases
pFnCas12_Fig3C	n/a	J23100 promoter expressing a theophylline inducible FnCas12, used in Figure 3C	(Uribe et al., 2019)	Testing AcrlIA22 activity against a panel of Cas9 and Cas12 effector nucleases
pDual4_Spy	P <sub>BAD</sub> , GTTCATTCAAGGCAC CGGAC	Arabinose inducible gRNA for SpyCas9 targeting pZE21	(Uribe et al., 2019)	Testing AcrlIA22 activity against a panel of Cas9 and Cas12 effector nucleases
pDual4_Nm	P <sub>BAD</sub> , GAACACGGCGGCATC AGAGC	Arabinose inducible gRNA for NmCas9 targeting pZE21	(Uribe et al., 2019)	Testing AcrlIA22 activity against a panel of Cas9 and Cas12 effector nucleases
pDual4_Lb	P <sub>BAD</sub> , TCAAGACCGACCTGT CCGGTGCCCTGAATG	Arabinose inducible gRNA for LbCas12 targeting pZE21	(Uribe et al., 2019)	Testing AcrlIA22 activity against a panel of Cas9 and Cas12 effector nucleases
pDual4_Fn	P <sub>BAD</sub> , TCAAGACCGACCTGT CCGGTGCCCTGAATG	Arabinose inducible gRNA for FnCas12 targeting pZE21	(Uribe et al., 2019)	Testing AcrlIA22 activity against a panel of Cas9 and Cas12 effector nucleases

**Supplemental Table 5.** Gene sequences used in this study.







## References for Supplemental Tables.

An, S.Y., Ka, D., Kim, I., Kim, E.-H., Kim, N.-K., Bae, E., and Suh, J.-Y. (2020). Intrinsic disorder is essential for Cas9 inhibition of anti-CRISPR AcrIIA5. *Nucleic Acids Research* 48, 7584-7594.

Athukoralage, J.S., McMahon, S.A., Zhang, C., Gruschow, S., Graham, S., Krupovic, M., Whitaker, R.J., Gloster, T.M., and White, M.F. (2020). An anti-CRISPR viral ring subverts type III CRISPR immunity. *Nature* 577, 572-575.

Bhoobalan-Chitty, Y., Johansen, T.B., Di Cianni, N., and Peng, X. (2019). Inhibition of Type III CRISPR-Cas Immunity by an Archaeal Virus-Encoded Anti-CRISPR Protein. *Cell* 179, 448-458 e411.

Bondy-Denomy, J., Garcia, B., Strum, S., Du, M., Rollins, M.F., Hidalgo-Reyes, Y., Wiedenheft, B., Maxwell, K.L., and Davidson, A.R. (2015). Multiple mechanisms for CRISPR-Cas inhibition by anti-CRISPR proteins. *Nature* 526, 136-139.

Bondy-Denomy, J., Pawluk, A., Maxwell, K.L., and Davidson, A.R. (2013). Bacteriophage genes that inactivate the CRISPR/Cas bacterial immune system. *Nature* 493, 429-432.

Chowdhury, S., Carter, J., Rollins, M.F., Golden, S.M., Jackson, R.N., Hoffmann, C., Nosaka, L., Bondy-Denomy, J., Maxwell, K.L., Davidson, A.R., et al. (2017). Structure Reveals Mechanisms of Viral Suppressors that Intercept a CRISPR RNA-Guided Surveillance Complex. *Cell* 169, 47-57 e11.

Dong, Guo, M., Wang, S., Zhu, Y., Wang, S., Xiong, Z., Yang, J., Xu, Z., and Huang, Z. (2017). Structural basis of CRISPR-SpyCas9 inhibition by an anti-CRISPR protein. *Nature* 546, 436-439.

Eitzinger, S., Asif, A., Watters, K.E., Iavarone, A.T., Knott, G.J., Doudna, J.A., and Minhas, F. (2020). Machine learning predicts new anti-CRISPR proteins. *Nucleic Acids Res* 48, 4698-4708.

Esvelt, K.M., Mali, P., Braff, J.L., Moosburner, M., Yaung, S.J., and Church, G.M. (2013). Orthogonal Cas9 proteins for RNA-guided gene regulation and editing. *Nat. Methods* 10, 1116-1123.

Forsberg, K.J., Bhatt, I.V., Schmidtke, D.T., Javanmardi, K., Dillard, K.E., Stoddard, B.L., Finkelstein, I.J., Kaiser, B.K., and Malik, H.S. (2019). Functional metagenomics-guided discovery of potent Cas9 inhibitors in the human microbiome. *Elife* 8.

Fuchsauer, O., Swuec, P., Zimberger, C., Amigues, B., Levesque, S., Agudelo, D., Duringer, A., Chaves-Sanjuan, A., Spinelli, S., Rousseau, G.M., et al. (2019). Cas9 Allosteric Inhibition by the Anti-CRISPR Protein AcrIIA6. *Mol Cell* 76, 922-937 e927.

Garcia, B., Lee, J., Edraki, A., Hidalgo-Reyes, Y., Erwood, S., Mir, A., Trost, C.N., Seroussi, U., Stanley, S.Y., Cohn, R.D., et al. (2019). Anti-CRISPR AcrIIA5 Potently Inhibits All Cas9 Homologs Used for Genome Editing. *Cell Rep* 29, 1739-1746 e1735.

Guo, T.W., Bartesaghi, A., Yang, H., Falconieri, V., Rao, P., Merk, A., Eng, E.T., Raczkowski, A.M., Fox, T., Earl, L.A., et al. (2017). Cryo-EM Structures Reveal Mechanism and Inhibition of DNA Targeting by a CRISPR-Cas Surveillance Complex. *Cell* 171, 414-426 e412.

He, F., Bhoobalan-Chitty, Y., Van, L.B., Kjeldsen, A.L., Dedola, M., Makarova, K.S., Koonin, E.V., Brodersen, D.E., and Peng, X. (2018). Anti-CRISPR proteins encoded by archaeal lytic viruses inhibit subtype I-D immunity. *Nat Microbiol* 3, 461-469.

Hirschi, M., Lu, W.T., Santiago-Frangos, A., Wilkinson, R., Golden, S.M., Davidson, A.R., Lander, G.C., and Wiedenheft, B. (2020). AcrIF9 tethers non-sequence specific dsDNA to the CRISPR RNA-guided surveillance complex. *Nat Commun* 11, 2730.

Janowski, R., and Niessing, D. (2020). The large family of PC4-like domains - similar folds and functions throughout all kingdoms of life. *RNA Biol* 17, 1228-1238.

Jiang, F., Liu, J.J., Osuna, B.A., Xu, M., Berry, J.D., Rauch, B.J., Nogales, E., Bondy-Denomy, J., and Doudna, J.A. (2019). Temperature-Responsive Competitive Inhibition of CRISPR-Cas9. *Mol Cell* 73, 601-610 e605.

Knott, G.J., Cress, B.F., Liu, J.J., Thornton, B.W., Lew, R.J., Al-Shayeb, B., Rosenberg, D.J., Hammel, M., Adler, B.A., Lobba, M.J., *et al.* (2019a). Structural basis for AcrVA4 inhibition of specific CRISPR-Cas12a. *Elife* 8.

Knott, G.J., Thornton, B.W., Lobba, M.J., Liu, J.J., Al-Shayeb, B., Watters, K.E., and Doudna, J.A. (2019b). Broad-spectrum enzymatic inhibition of CRISPR-Cas12a. *Nat Struct Mol Biol* 26, 315-321.

Lee, J., Mir, A., Edraki, A., Garcia, B., Amrani, N., Lou, H.E., Gainetdinov, I., Pawluk, A., Ibraheim, R., Gao, X.D., *et al.* (2018). Potent Cas9 Inhibition in Bacterial and Human Cells by AcrIIC4 and AcrIIC5 Anti-CRISPR Proteins. *mBio* 9.

Leon, L.M., Park, A.E., Borges, A.L., Zhang, J.Y., and Bondy-Denomy, J. (2020). Mobile element warfare via CRISPR and anti-CRISPR in *Pseudomonas aeruginosa*. *bioRxiv*, 2020.2006.2015.151498.

Lin, P., Qin, S., Pu, Q., Wang, Z., Wu, Q., Gao, P., Schettler, J., Guo, K., Li, R., Li, G., *et al.* (2020). CRISPR-Cas13 Inhibitors Block RNA Editing in Bacteria and Mammalian Cells. *Mol Cell* 78, 850-861 e855.

Liu, L., Yin, M., Wang, M., and Wang, Y. (2019). Phage AcrIIA2 DNA Mimicry: Structural Basis of the CRISPR and Anti-CRISPR Arms Race. *Mol Cell* 73, 611-620 e613.

Mahendra, C., Christie, K.A., Osuna, B.A., Pinilla-Redondo, R., Kleinstiver, B.P., and Bondy-Denomy, J. (2020). Broad-spectrum anti-CRISPR proteins facilitate horizontal gene transfer. *Nat Microbiol* 5, 620-629.

Marino, N.D., Zhang, J.Y., Borges, A.L., Sousa, A.A., Leon, L.M., Rauch, B.J., Walton, R.T., Berry, J.D., Joung, J.K., Kleinstiver, B.P., *et al.* (2018). Discovery of widespread Type I and Type V CRISPR-Cas inhibitors. *Science*.

Meeske, A.J., Jia, N., Cassel, A.K., Kozlova, A., Liao, J., Wiedmann, M., Patel, D.J., and Marraffini, L.A. (2020). A phage-encoded anti-CRISPR enables complete evasion of type VI-A CRISPR-Cas immunity. *Science* 369, 54-59.

Osuna, B.A., Karambelkar, S., Mahendra, C., Christie, K.A., Garcia, B., Davidson, A.R., Kleinstiver, B.P., Kilcher, S., and Bondy-Denomy, J. (2020). Listeria Phages Induce Cas9 Degradation to Protect Lysogenic Genomes. *Cell Host Microbe* 28, 31-40 e39.

Pasolli, E., Asnicar, F., Manara, S., Zolfo, M., Karcher, N., Armanini, F., Beghini, F., Manghi, P., Tett, A., Ghensi, P., *et al.* (2019). Extensive Unexplored Human Microbiome Diversity Revealed by Over 150,000 Genomes from Metagenomes Spanning Age, Geography, and Lifestyle. *Cell* 176, 649-662 e620.

Pawluk, A., Amrani, N., Zhang, Y., Garcia, B., Hidalgo-Reyes, Y., Lee, J., Edraki, A., Shah, M., Sontheimer, E.J., Maxwell, K.L., *et al.* (2016). Naturally Occurring Off-Switches for CRISPR-Cas9. *Cell* 167, 1829-1838 e1829.

Pawluk, A., Bondy-Denomy, J., Cheung, V.H., Maxwell, K.L., and Davidson, A.R. (2014). A new group of phage anti-CRISPR genes inhibits the type I-E CRISPR-Cas system of *Pseudomonas aeruginosa*. *MBio* 5, e00896.

Pawluk, A., Shah, M., Mejdani, M., Calmettes, C., Moraes, T.F., Davidson, A.R., and Maxwell, K.L. (2017). Disabling a Type I-E CRISPR-Cas Nuclease with a Bacteriophage-Encoded Anti-CRISPR Protein. *MBio* 8.

Pinilla-Redondo, R., Shehreen, S., Marino, N.D., Fagerlund, R.D., Brown, C.M., Sørensen, S.J., Fineran, P.C., and Bondy-Denomy, J. (2020). Discovery of multiple anti-CRISPRs uncovers anti-defense gene clustering in mobile genetic elements. *bioRxiv*, 2020.2005.2022.110304.

Rauch, B.J., Silvis, M.R., Hultquist, J.F., Waters, C.S., McGregor, M.J., Krogan, N.J., and Bondy-Denomy, J. (2017). Inhibition of CRISPR-Cas9 with Bacteriophage Proteins. *Cell* 168, 150-158 e110.

Shin, J., Jiang, F., Liu, J.-J., Bray, N.L., Rauch, B.J., Baik, S.H., Nogales, E., Bondy-Denomy, J., Corn, J.E., and Doudna, J.A. (2017). Disabling Cas9 by an anti-CRISPR DNA mimic. *Science Advances* 3.

Song, G., Zhang, F., Zhang, X., Gao, X., Zhu, X., Fan, D., and Tian, Y. (2019). AcrIIA5 Inhibits a Broad Range of Cas9 Orthologs by Preventing DNA Target Cleavage. *Cell Rep* 29, 2579-2589 e2574.

Stanley, S.Y. (2018). An Investigation of Bacteriophage Anti-CRISPR and Anti-CRISPR Associated Proteins. In Department of Molecular Genetics (<http://hdl.handle.net/1807/97883>: University of Toronto), pp. 120.

Uribe, R.V., van der Helm, E., Misiakou, M.A., Lee, S.W., Kol, S., and Sommer, M.O.A. (2019). Discovery and Characterization of Cas9 Inhibitors Disseminated across Seven Bacterial Phyla. *Cell Host Microbe* 25, 233-241 e235.

Varble, A., Campisi, E., Euler, C.W., Fyodorova, J., Rostøl, J.T., Fischetti, V.A., and Marraffini, L.A. (2020). Integration of prophages into CRISPR loci remodels viral immunity in &lt;em&gt;Streptococcus pyogenes&lt;/em&gt;. *bioRxiv*, 2020.2010.2009.333658.

Wang, J., Ma, J., Cheng, Z., Meng, X., You, L., Wang, M., Zhang, X., and Wang, Y. (2016a). A CRISPR evolutionary arms race: structural insights into viral anti-CRISPR/Cas responses. *Cell Res* 26, 1165-1168.

Wang, X., Yao, D., Xu, J.G., Li, A.R., Xu, J., Fu, P., Zhou, Y., and Zhu, Y. (2016b). Structural basis of Cas3 inhibition by the bacteriophage protein AcrF3. *Nat Struct Mol Biol* 23, 868-870.

Watters, K.E., Fellmann, C., Bai, H.B., Ren, S.M., and Doudna, J.A. (2018). Systematic discovery of natural CRISPR-Cas12a inhibitors. *Science*.

Watters, K.E., Shivram, H., Fellmann, C., Lew, R.J., McMahon, B., and Doudna, J.A. (2020). Potent CRISPR-Cas9 inhibitors from *Staphylococcus* genomes. *Proc Natl Acad Sci U S A* 117, 6531-6539.

Yang, H., and Patel, D.J. (2017). Inhibition Mechanism of an Anti-CRISPR Suppressor AcrIIA4 Targeting SpyCas9. *Mol Cell* 67, 117-127 e115.

Zetsche, B., Gootenberg, J.S., Abudayyeh, O.O., Slaymaker, I.M., Makarova, K.S., Essletzbichler, P., Volz, S.E., Joung, J., van der Oost, J., Regev, A., et al. (2015). Cpf1 Is a Single RNA-Guided Endonuclease of a Class 2 CRISPR-Cas System. *Cell*.

Zhang, H., Li, Z., Daczkowski, C.M., Gabel, C., Mesecar, A.D., and Chang, L. (2019). Structural Basis for the Inhibition of CRISPR-Cas12a by Anti-CRISPR Proteins. *Cell Host Microbe* 25, 815-826 e814.

Zhang, K., Wang, S., Li, S., Zhu, Y., Pintilie, G.D., Mou, T.C., Schmid, M.F., Huang, Z., and Chiu, W. (2020). Inhibition mechanisms of AcrF9, AcrF8, and AcrF6 against type I-F CRISPR-Cas complex revealed by cryo-EM. *Proc Natl Acad Sci U S A* 117, 7176-7182.